OBSERVATIONS OF ANTICYCLONES IN HAWAIʻI USING SURFACE DRIFTERS

A DISSERTATION SUBMITTED TO THE GRADUATE DIVISION OF THE UNIVERSITY OF HAWAIʻI IN PARTIAL FULFILLMENT OF THE REQUIREMENTS FOR THE DEGREE OF

DOCTOR OF PHILOSOPHY

IN

OCEANOGRAPHY

DECEMBER 2019

By
Victoria C. Futch

Dissertation Committee:

Pierre Flament, Chairperson
François Ascani
Glenn Carter
Brian Powell
Oceana Francis

To Eva

Acknowledgements

I'd like to thank my advisor, Dr. Pierre Flament and my committee members for their support during my time as a student. I appreciated your willingness to work with my unique time and military constraints. I couldn't have done this without that support. Additionally I'd like to thank Dr. Laurence Armi, an un-official member of my committee for his concern, assistance, and mentorship during my research.

I received drifter data from Dr. Rick Lumpkin, as well as comments and feedback on my work. I also received physical drifters from Art Allen. Thanks for helping smooth the way for me to deploy and collect the data from these drifters. Thanks goes to the entire Radlab team for helping with buoy refurbishment and deployment. Special thanks to Ryan for the hours he spent making battery packs and cleaning buoy electronics. I could not have done all of that without your help!

I would also like to thank my husband, Matt. He willingly (most of the time) travelled all over the Hawaiian islands helping me deploy and retrieve drifting buoys. I only had to endure a few Ekman and Van Halen jokes in return. To my family in California, thanks for keeping me sane and coming to visit me in Hawai'i. And to my mom, thanks for suffering a bit and volunteering to proofread the first draft of this dissertation.

Abstract

Mesoscale eddies are common in the lee of the Hawaiian Islands. Persistent cyclones (anticyclones) have been observed downstream of the northern (southern) corner of the leeward side of the island of Hawai'i. In addition, smaller submesoscale eddies have been observed in the lee of other islands, such as Oahu and Lanai. The region has been subject to numerous model studies of the lee eddies, but the last comprehensive observational study was completed over twenty years ago. Now, with the increase in available surface drifting buoys, the coverage of some lee areas by High Frequency Radar (HFR), as well as twenty years of satellite data an observational study is well timed. Surface drifting buoys were used to determine the frequency, timing, and characteristics of anticyclones in the lee of both Hawai'i and Oahu. The anticyclones in the lee of Hawai'i are formed most commonly in summer months, when both the wind and ocean forcing is the steadiest. The outline of the wake created by the anticyclonic drifting buoys extends westward from the island over 1500 km and is directed to the southwest. An analysis of wind and ocean forcing using Empirical Orthogonal Function (EOF) methodology revealed an overlap in spatial signature with the wind-forced annual sea level anomaly patterns, as well as partial overlap with a non wind-induced 100-day signature. Due to the overlap, exact forcing cannot be determined without better quality observations of ocean currents to the south of the island. The eddies in the lee of Oahu were smaller, had a much shortened leeward extent, and were observed more often due to the presence of HFR currents. The anticyclones and most of the cyclones in the lee of Oahu all occurred during steady Northeast Trade winds and can be explained by wind stress curl induced forcing. Three cyclones formed during trade wind

reversals where wind stress curl forcing was zero, leaving a vorticity residual that can only be explained by ocean stress induced vorticity.

Table of Contents

List of Tables

List of Figures

Chapter 1

Introduction

1.1 Motivation

The Hawaiian Island chain sits in the Pacific subtropical gyre. Centered around 20 °N, the islands lie directly in the path of the North Equatorial Current (NEC) and the North East (NE) trade winds. As the westward NEC reaches the islands, it bifurcates, with part flowing along the windward side of the islands as the Northern Hawaiian Ridge Current (NHRC), and part travelling past the Southern-most point of the island of Hawai‘i, and separating from the island (Figure 1.1) (Lumpkin and Flament 2013; Flament et al. 1998). In the lee of the islands, centered at 19.5 °N is the eastward Hawaii Lee Counter-current (HLCC) (Lumpkin and Flament 2013) and along with the westward NEC it creates a gyre-like circulation in the direct lee of the islands.

Persistent vortices are observed in the lee of the islands (Wyrtki 1982). In general, cyclonic vortices are observed north of, and anticyclonic vortices observed south of 19.5 °N (Lumpkin 1998; Patzert 1969). The cyclonic vortices are more biologically productive due to the upwelling of colder, more nutrient dense waters in their core (Vaillancourt et al. 2003) and have been well studied in the Hawaiian region (Calil et al. 2008). The cyclonic vortices in the lee of the Hawaiian Islands have been found to be wind-driven eddies (Jia et al. 2011). Anticyclones, which are characterized by downwelling in the core,

depress the thermocline and cut-off nutrient-rich waters from the surface, making them less biologically productive (Fong et al. 2008) and have been examined in less detail. The dominant formation mechanism for the anticyclones has also not been successfully resolved (Lumpkin 1998; Flament et al. 2001).

In the Hawaiian Islands there are two main mechanisms that could create anticyclonic vortices: 1) Ekman pumping from wind stress curl, and 2) shear instability in the NEC as it separates from the island of Hawai‘i.

Wind Stress Curl: The large vertical extent of the Hawaiian Islands, created by volcanic topography, causes the islands to impede the flow of the NE trade winds. This blockage of the NE trades creates wind stress curl dipoles in the lee, with the largest dipoles in the lee of Hawai‘i, Maui, and Oahu (Chavanne et al. 2002). In regions of negative wind stress curl there are convergent Ekman transports, which creates downwelling, spinning up anticyclonic vortices.

Shear instability in the NEC: The Hawaiian Islands lie in the path of the NEC. As the NEC hits Hawai‘i, it passes along the southeast side of the Island of Hawai‘i where there is a relatively narrow and steep shelf (Figure 1.2). As the NEC passes South Point, Hawai‘i, it separates from the island. There is a shallow underwater promontory that extends off the tip of South Point, which could impact the location of the separation point. This separation, or blocking of the current by the island, creates an unstable shear layer (Flament et al. 2001). This addition of clockwise (negative) vorticity caused by the instability, can spin up anticyclonic vortices.

This leads to the question, which mechanism is the dominant mechanism that spins-up anticyclonic vortices in the lee of Hawai‘i? In this study, I aim to help answer this question by examining two related problems:

- Anticyclones are observed frequently in the lee of Hawai'i, but there has not been a comprehensive observational study completed in recent years. What are the size, duration, characteristics and seasonality of the anticyclones? I intend to use historical observational data from the last 20 years to build upon previous knowledge of anticyclones in Hawai'i. And in addition to just examining the anticyclones that are persistent near Hawai'i, I also examine similar lee eddies off Oahu.

- What are the large scale atmospheric and oceanic conditions present as anticyclones evolve off the southern tip of Hawai'i? How do these conditions explain the presence of anticyclones in Hawai'i?

1.2 Outline

Chapter 2 uses historical drifter data as well as satellite winds and sea surface anomalies to examine the timing, frequency, and characteristics of the anticyclones formed in the lee of the island of Hawai'i. A database of historical anticyclones was built by analyzing surface drifter data from the Global Drifter Program - Surface Velocity Program (SVP) database. From this data, 25 anticyclones were identified from surface drifter trajectories. The characteristics of the anticyclones, including period, radius, date of formation, etc. were estimated from the drifter trajectories. The anticyclones were shown to be most common in late summer and early fall. After formation off the southern tip of the island of Hawai'i, the anticyclones followed a track very similar to the theoretical anticyclonic sector shown in Figure 1.1 based off of Lumpkin (1998). The anticyclones persisted for up to several months, and out to 170 °W. Chapter 2 also examines the atmospheric and oceanic forcing that creates Hawai'i's ocean wake. Using Empirical Orthogonal Function (EOF) analysis, satellite-derived winds from Quikscat and satellite-derived sea surface height anomalies from AVISO are analyzed to determine large scale patterns related to island wakes. The primary EOF modes of the wind data show that the NE trade winds are fairly stable, even after removing the mean flow. The first three modes demonstrate the annual fluctuations in the

trade winds, such as the shift between NE trades and Kona (south-westerly) winds, shifts in the main zonal jet of the NE trades due to seasonal shifts in the Pacific subtropical gyre, and the seasonal NE trade wind bursts. These modes comprise most of (80%) of the combined variance in the data. Higher scale fluctuations account for less than 20% of the variance and are hard to distinguish from noise. The primary modes of the sea surface anomaly data show a seasonal shift in the Pacific subtropical gyre due to shifts in winds. However, unlike the wind data, higher frequency patterns are visible in lower modes with sea surface height anomalies constrained to the lee of the islands occurring every 100 days. These are most likely related to the eddy shedding by the Hawaiian islands but do not correlate with wind forcing.

Chapter 3 uses drifter statistics and High Frequency Radar (HFR) to examine flow properties in the lee of the island of Oahu, in particular it focuses on the development of lee eddies. Mean currents derived from the drifters show counter-rotating vortices in the lee of the island. The presence of these vortices was confirmed using HFR, where 5 anticyclones and 8 cyclones were observed by HFR in the lee of Oahu. These vortices are smaller than the lee eddies that form off of Hawai‘i and did not travel great distances away from the island, but occurred at a higher frequency. The majority of the drifters appear to be wind-generated, and this was confirmed by examining the vorticity budget of the drifters. However, there were three cyclones that formed during a trade-wind reversal and this eliminated the wind-stress curl forcing, and the vorticity budget was not able to be closed without allowing for additional forcing from ocean stress.

Chapter 4 provides an estimate of surface drifter leeway. Two drifter varieties, a Davis type drifter and a Microstar type drifter were used in Chapter 3. The response of the drifters to different forces needs to be understood in order to accurately use the data. The drifters were launched in a gridded cluster with a zonal spacing of 2-km. At each grid point, one drifter of each variety was launched, approximately 200m apart. The separation rate of the clusters and the separation rate of the drifter pairs were examined. The drifter pairs at

each grid point did not respond similarly to the forcing, and for the pairs, they separated up to 8km in 24 hours. The leeway of each drifter type was estimated. Both drifters exhibited large crosswind leeway that can be explained by a push from Stokes drift from waves and surface Ekman currents. However, the Davis drifters crosswind leeway was larger than the Microstar's leeway, indicating that wind forcing and vertical shear in the current structure are greater than the Microstars.

Chapter 5 draws together the main conclusions found in this dissertation and discusses questions that remain, whether they arose during this research, or were not able to be answered given this data-set.

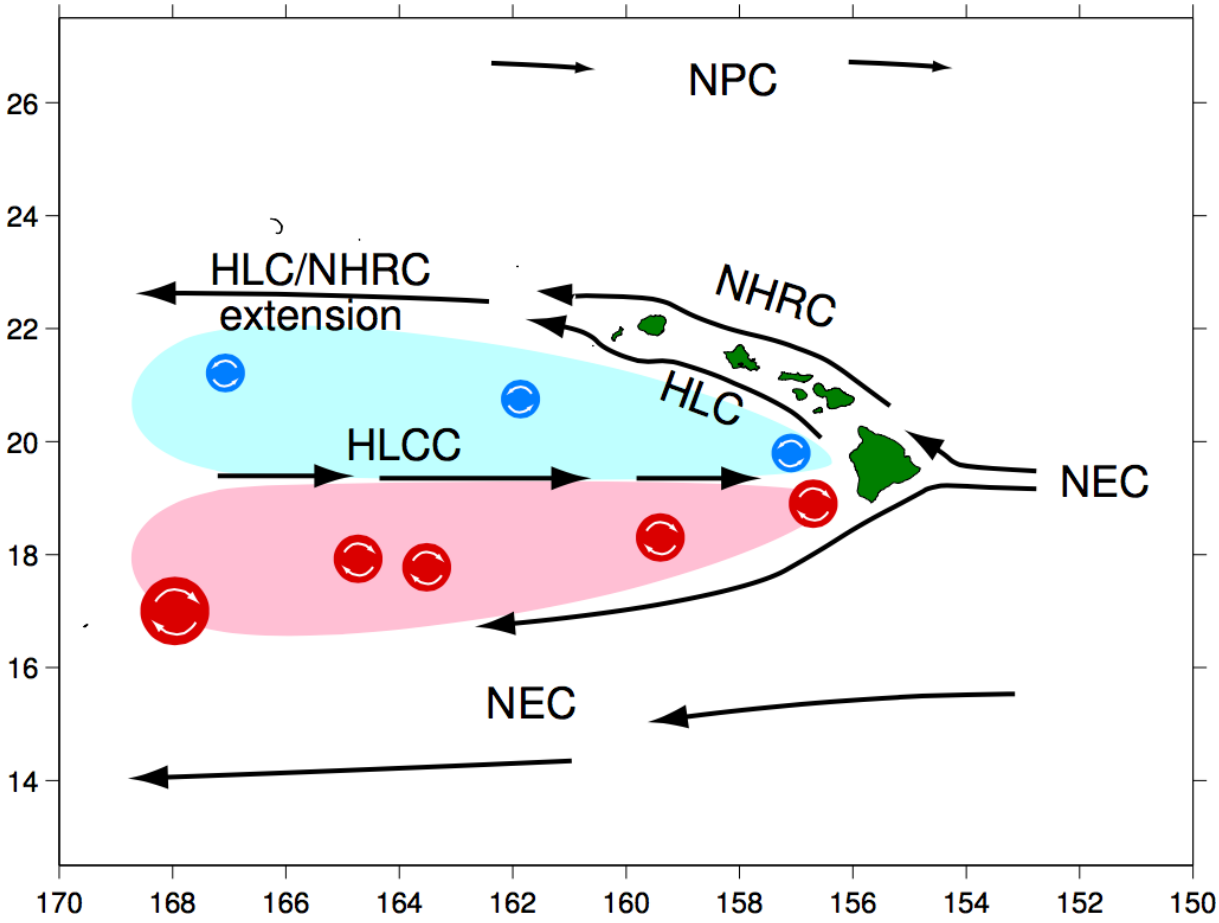

Figure 1.1: The main currents of the Hawaiian islands. After (Lumpkin 1998)

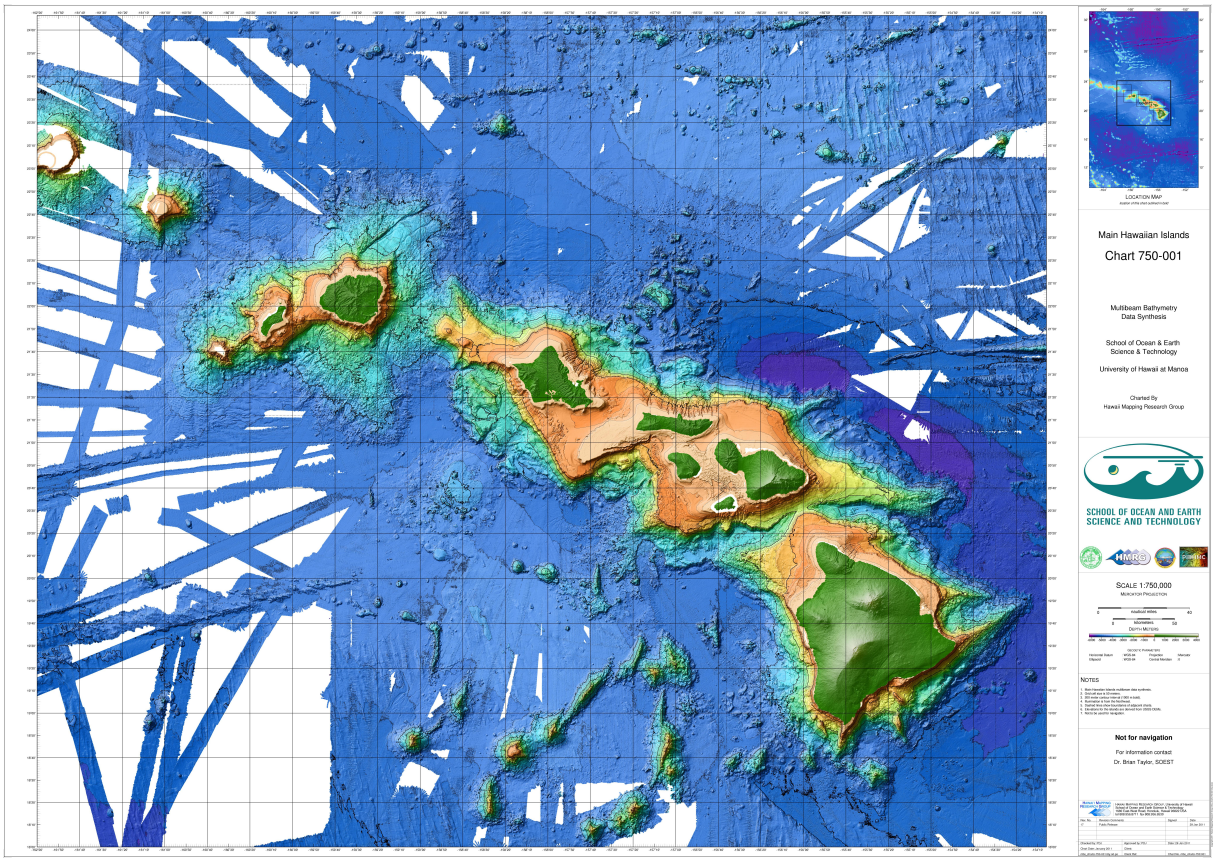

Figure 1.2: The bathymetry of the Hawaiian Islands. The shallow underwater promontory off the Southern tip of the island of Hawai'i is clearly visible. Image from Main Hawaiian Islands Multibeam Bathymetry and Backscatter Synthesis.

Chapter 2

Observations of Anticyclones in the Lee of Hawai'i Island

Abstract

The lee of the Hawaiian Islands is known for eddy generation. Counter-rotating vortices have been observed with a cyclonic zone to the north and an anticyclonic zone to the south of the main island of Hawai'i. The cyclones have been proven to be wind-driven. Less is known about the anticyclones in the region. This study updates the observational knowledge of anticyclones in the lee of Hawai'i using 25 years of surface drifting buoys. 20 years of satellite data was used to look for spatial and temporal patterns in wind stress and sea level anomaly (SLA) that would help explain the vortices. The anticyclones were most common in summer when the wind forcing was the strongest and a 1500km long anticyclonic sector is visible downstream of Hawai'i. EOF results for both the wind and SLA show the most overlap with the anticyclonic sector in the annual cycle, implying wind-forcing can explain the vortex formation. There is also some overlap with the 100 day signal seen in the SLA and there is no similar frequency in the wind data, but without quality data for the NEC strength and variability south of Hawai'i, ocean forcing cannot be confirmed.

2.1 Introduction

The Hawaiian Island chain sits in the Pacific subtropical gyre. Centered around 20 °N, the islands lie directly in the path of the North Equatorial Current (NEC) and the North East (NE) trade winds. The islands block the flow of both the NE trade winds and NEC, creating unique ocean wake patterns in the lee of the islands. The NE trade winds are part of the dominant global scale wind pattern formed by meridional heat differentials. In theory the NE trades extend from the equator to 30 °N, however, in reality the latitude band of the NE trades varies with season due to differential heating caused by the earth's tilt. The migration of the Intertropical Convergence Zone (ITCZ; where the NE trade winds meet the SE trade winds) towards the summer hemisphere dictates the meridional extent of the NE trades. As the NE trades come in contact with the steep volcanic topography of the Hawaiian islands, the winds are blocked, creating regions of opposing wind stress curl in the near vicinity of the lee and a visible atmospheric wake which can be seen up to 3000 km downstream of the islands (Xie et al. 2001; Chavanne et al. 2002).

The NEC is the southern boundary of the Pacific subtropical gyre and flows from east to west from around 8 °N to 20 °N (Talley et al. 2011). When the westward NEC reaches the islands it bifurcates, flowing along the windward side of the islands as the Northern Hawaiian Ridge Curent (NHRC) (Qiu et al. 1997), and travelling past the southern-most point of the island of Hawai'i as the NEC and separating from the island (Lumpkin and Flament 2013; Flament et al. 1998). In the lee of the islands, centered at 19.5 °N is the eastward Hawaii Lee Countercurrent (HLCC) and along with the westward NEC it creates a gyre-like circulation in the direct lee of the islands (Flament et al. 1998).

Persistent vortices are observed in the lee of the islands (Patzert 1969; Wyrtki 1982). These vortices are a significant part of Hawai'i's oceanic wake, originating from either the wind stress curl dipoles caused by the NE trade winds or the shear instability of the NEC as it separates from island of Hawai'i. Seasonal shifts or higher frequency patterns in the

predominant wind and currents could be responsible for the mechanism and timing of the vortices' formation in the lee of Hawai‘i, which then impacts the strength and location of Hawaii‘s wake currents. Mitchum (1995) identified a 90-day signal in tidal gauges near Johnston Atoll that was back-traced to its origin in the lee of Hawai‘i. Mitchum suggested this signal was related to eddy shedding by the island of Hawai‘i. Lumpkin (1998) identified two distinct eddy zones in the lee of Hawai‘i, separated by the HLCC: an elongated cyclonic zone north of and an elongated anticyclonic zone south of the HLCC. Yoshida et al. (2010) used satellite sea surface height data to investigate wind-driven eddies in the lee of Hawai‘i, which they connected to a 60-day signal in sea surface height (SSH) closer to the island of Hawai‘i. Further to the west, they found a 100-day signal in ssh, but did not correlate the westernmost signal with patterns in wind stress.

From a mean flow perspective, the Hawaii Lee Counter Current (HLCC) appears to be associated with the Reynold's shear stresses induced by these vortices. The conversion from eddy to mean energy suggests that the anticyclonic vortices induce a meridional transport of zonal momentum, the convergence of which accelerates the HLCC and maintains the HLCC/NEC zonal shear (Lumpkin and Flament 2013).

The biologically productive cyclonic eddies have been the subject of many interdisciplinary studies (Aristegui et al. 1997; Calil et al. 2008). On the contrary, negative Ekman divergence due to anticyclonic wind-stress curl does not have significant biological signature other than horizontal advection, and as a result, anticyclones have not been studied as much as cyclones. While there are substantial modeling studies of eddies in Hawai‘i (Calil et al. 2008; Jia et al. 2011; Souza et al. 2014), most observational studies of anticyclones in Hawai‘i are outdated. Patzert (1969) published the first comprehensive report of eddies in Hawaiian waters in 1969, using shipboard observations. Wyrtki (1982) followed a decade later describing eddy patterns and signals seen throughout the islands. The last comprehensive observational account of anticyclones in Hawai‘i was by Lumpkin (1998) who described the mean path of anticyclones formed in the lee of Hawai‘i using

drifter statistics. However, since 1998 the number of drifters that have passed through the Hawaiian islands has doubled. This robust dataset, along with the now 20 years of satellite altimetry and wind data, is a promising source to update our current knowledge of anticyclones in Hawai‘i.

Here we utilized the 16 additional years of drifter data to clarify characteristics of the anticyclones formed in Hawai‘i. What are the size, frequency, seasonal timing, propagation and duration of the anticyclones in Hawai‘i? Then using EOF analysis of satellite winds and sea level anomalies we investigate patterns in the large scale circulation in both the atmosphere and ocean to determine the stability of atmospheric forcing and resulting sea level anomalies around the Hawaiian Islands. Additionally we investigated annual and higher frequency patterns in wind and sea level anomaly data and their relationship to the mesoscale vortices around Hawai‘i.

2.2 Methods

2.2.1 Drifter Data

Drifter trajectories from the Global Drifter Program-Surface Velocity Program (SVP) were used to identify anticyclones in the lee of Hawai‘i. These drifting buoys consisted of both the original and mini-SVP drifters. Both types of SVP drifters were designed to have the same drag ratio, allowing accurate comparison between drifters (Lumpkin and Pazos 2007). SVP drifters are drogued to 15m in depth and on average transmit for 400 days before expiring. The data is collected via ARGOS, then undergoes a strict quality control process, and is interpolated to 6-hour intervals (Lumpkin and Pazos 2007). All SVP drifters passing through the Hawaiian Islands were extracted for analysis. The limits were set by a box, with boundaries defined by 14 °N-25 °N in the meridional direction, and 180 °W-140 °W in the zonal direction. Over the length of the dataset there were 832 SVP drifters that entered this region. The number of surface drifting buoys originating or passing

through the Hawaiian Islands has increased dramatically since 1998. Lumpkin (1998) had only 356 passing through the Hawaiian Islands, compared to 832 today. Additionally the number of observations available in each 0.25 ° box surrounding the islands has grown from up to 400 to up to 2000 (Figure 2.1). Figure 2.2 shows the trajectories of all the drifters, broken down into 20 day segments and color-coded by direction. The main currents of the islands of Hawai‘i are visible in the drifter data. The dominant red color south of the islands demonstrates the westward flow of the NEC. The mixture of colors in the direct lee corresponds to the highly varied flow in Hawai‘i's wake. Additionally there is a band of green, eastward flow centered around 19.5N, in line with the center of the HLCC. The highest number of observations is in the lee of the island of Hawai‘i, which corresponds to the largest variance, $u'^2 + v'^2$ ($\frac{m^2}{s^2}$) in the SVP-based drifter currents.

Mean currents were calculated from the drifting buoys by three different datasets: 1) All 832 drifters, 2) All drifters except the anticyclonic loopers (779 drifters), and 3) only the anticyclonic loopers (53 drifters). To calculate the mean currents, the area was binned in 0.25 ° boxes and the mean current was calculated in each box from all available observations. Mean currents were kept if they were significantly different than zero.

A visual inspection of each drifter's path was completed to identify anticyclonic looping trajectories (loopers).[1] These loopers were then conditionally sampled to remove any trajectory which entered the region with pre-existing anticyclonic vorticity. This left 53 drifting buoys with anticyclonic looping trajectories in the lee of the islands. After quality control procedures, and based on the date time group (DTG) and positions of the drifters, there were 25 distinct anticyclonic vortices identified from the 37 loopers.

The period and radius of the anticyclonic loopers were calculated using the method presented in Lumpkin (2016). However, unlike Lumpkin, this method was not used to identify loopers, but to verify looper status and to quantify known looper statistics. The

[1] In this study, only anticyclones were of interest, so cyclonically looping drifters were grouped in with non-loopers. From this point forward, the term loopers refers only to anticyclonic loopers.

spin of each of the 37 drifting buoys identified as loopers was calculated using:

$$\Omega = \frac{< u'dv' - v'du' >}{(2\Delta t EKE)} \tag{2.1}$$

$$EKE = \frac{1}{2}(< u' >^2 + < v' >^2) \tag{2.2}$$

where u', v' are the eddy velocities, du', dv' are the changes in those velocities over the time step Δt and EKE is the eddy kinetic energy. From the spin, both the period and radius of the drifter's rotation can be calculated:

$$P = \frac{2\pi}{|\Omega|} \tag{2.3}$$

$$R = \frac{\sqrt{2EKE}}{|\Omega|} \tag{2.4}$$

Time periods of prolonged negative (positive) spin indicated that the drifter may be caught in an anticyclonic (cyclonic) vortex. Lumpkin (2016) defined the length of these time periods as persistence. If the persistence was at least twice the theoretical period (the period calculated using the median value of Ω during the corresponding time period), then the drifter was confirmed as being in an vortex. This meant that the drifter made at least two complete rotations within the vortex. Drifters which only completed one full rotation were not identified as individual anticyclones. However, these drifters were kept in the anticyclonic looping database if the one rotation was within one standard deviation from the mean period and radius of the 25 quantified anticyclones. The anticyclonic looping database consisted of the 37 drifters that made up the 25 known anticyclones and 16 others that only made one loop, but were within the guidelines previously described.

An example of the results from the anticyclone identification and the subsequent calculation of looper statistics is shown in Figures 2.3 and 2.4. The anticyclone described is number twenty in Table 2.3. Anticyclone # 20 was identified from buoy number 22936. The zonal and meridional velocities, as well as sea surface temperature and trajectory are shown

in Figure 2.3. The strong oscillatory motion induced by the anticyclone is evident in the zonal and meridional velocities. Drifter 22936 entered the box in January, 2003 and exited the region in June, 2004. Drifter 22936 approached the islands from the east, and passed just south of the island of Hawai'i, entering the lee region in June, 2003. Immediately after entering the lee region, it became trapped in a long-lasting anticyclone. The anticyclone formed in the immediate lee of the island of Hawai'i with an initial orbital period of 3 days (taken from Figure 2.4), corresponding to a Rossby number of $Ro = -1$. The drifter remained trapped in the anticyclone for over 200 days, until February, 2004, as seen in Figure 2.4. Downstream, the mean period of the anticyclone, calculated using Lumpkin (2016), increased to 5 days, which it maintained for the rest of its life-span. The mean radius of the anticyclone when the period of was 3 days was 27 km, and the mean radius of the anticyclone when the period of 5 days was 26 km (Figure 2.4). The mean path of the anticyclone was consistent over its long life-span, with the anticyclone moving in the direction 267 °T, or nearly due westward at latitude 18 °N. It travelled a distance of 1456 km downstream, well past 170 °W. This is the second farthest distance travelled by an anticyclone that was observed in the SVP drifter database.

The method described above worked well for most drifters, however there was evidence of vortex merging in some of the loopers' trajectories, including anticyclone #20. This change in period and radius was not always obvious when plotted using the Eq. 2.4 and Eq. 2.3, and could lead to errors. As seen in Figure 2.4, there is variation in the calculations for radius and period as the vortex orbits. Taking the mean is intended to reduce this noise. It is also difficult to specify exactly when a drifter transitioned from one period to the next. The oscillatory motion in the velocities meant that a simple fourier transform of the zonal or meridional velocity would pull out dominant frequencies, but it did not yield any information on when the transitions occurred. In order to see time-frequency data, a one-dimensional wavelet analysis was used. Wavelet analysis is a means to pull out of a timeseries data the time intervals where specific spectral components occur. Here we used

a continuous wavelet transform (CWT) given by:

$$C(a, b, f(t), \psi(t)) = \int_{-\infty}^{\infty} f(t) \frac{1}{a} \psi^*(\frac{t-b}{a}) dt \tag{2.5}$$

where $C(a, b)$ represents the energy of the signal at any scale a (the scale parameter) and time b (the position parameter). ψ is the wavelet used in the transform, while ψ^* is the complex conjugate of the wavelet. A Morse wavelet was used here. A full discussion of Morse wavelets and their applicability to these timescales can be found in Olhede and Walden (2002); Lilly and Olhede (2012). The signal is multiplied by the wavelet and a transform is completed separately for different segments of the time domain. The result is a spectrogram where the various periods of the signal are plotted against the time-domain. This process allowed the transitions between vortex merges to be easily pulled from the velocity data of a looping drifter. Returning to the example of Anticyclone # 20, we can visualize the progression of the anticyclone over time. Figure 2.5 is the magnitude scalogram of the zonal velocity continuous wavelet transformation. The x-axis shows the time in days. The 509 days the drifter was active are represented in the length of the x-axis. The y-axis is a logarithmic scale of period, in days. The dashed line represents the boundary outside of which edge effects are large and the results are no longer valid. The drifter entered the anticyclone around day 200 and the initial orbital period of 3 days is visible in the CWT. The drifter remained in the anticyclone for 200 days, which is verified by the presence of high magnitude regions on the scalogram. The period also increased from 3 to 6 to 7 to 9 days as shown in Figure 2.5. These periods differ slightly from the previous results, but agree more with the observed behavior of the drifter. The change from the 6 to 7 day period was not observed in the calculations from the EKE, nor was the presence of the 9 day period near the end of the anticyclone's life. Also unlike the fourier transform and the method used in Lumpkin (2016), the timing of the changes are distinct in the CWT scalogram. For all loopers who exhibited vortex merging, a CWT analysis was conducted to verify or correct periods and establish the timing of each merger.

2.2.2 Satellite Data

The mean flow fields in the vicinity of the Hawaiian islands, in both the atmosphere and ocean, are well known. Here we are interested in the fluctuations about those means. One way to isolate variations in a flow is to use Empirical Orthogonal Function (EOF) analysis. EOF analysis provides a mechanism to identify patterns in a data set that explain the largest percentage of the data's variance. These patterns can then be compared to regional geophysics to determine if a link exists between the EOF modes and the theoretical dynamics. Another useful property of an EOF is that it can be used to reduce noise in a dataset. After the EOF has been calculated, the data can be re-constructed using only the dominant modes of variability, eliminating excess noise from the data. In this study, EOF analysis was conducted using eigenmethods with the following equation:

$$Ce - \lambda e = 0 \tag{2.6}$$

where C is the covariance matrix of the detrended data, e is the eigenvectors (EOF modes) and λ is the eigenvalues (EOF principle components). This method was used for standing wave patterns, which was acceptable for the windstress EOF. However, sea level patterns are usually propagating features and required the use of a complex EOF. A complex EOF (CEOF) utilizes a Hilbert transformation to switch into the frequency domain before the EOF is completed.[2] Here Empirical Orthogonal Function (EOF) analysis was used to determine the dominant patterns in the atmosphere and ocean in the vicinity of Hawai‘i. The dominant EOF modes were extracted from large scale wind and sea surface height data to explain seasonal, as well as higher frequency fluctuations. QuikScat wind vectors (1999-2009) and AVISO sea level anomalies (1992-2012) were used. The gridded data from each

[2] A more detailed explanation of EOF mechanics and use is provided in Appendix A

source was extracted and trimmed to equal spatial dimensions (14 °-25 °N,180 °-140 °W).[3] The mean was removed (Figure 2.6) from each data set before the EOF was computed using either conventional eigenmethods or complex Hilbert transform eigenmethods.

Ten years of satellite wind data from QuikScat with 8-day rolling wind vector composites were used in the calculation of the EOF modes and principle components. Wind speed data for each direction was converted into the corresponding wind stress based on methods demonstrated in Large and Pond (1981). The zonal and meridional components of wind stress were combined into a complex variable, w, before a vector EOF was used to calculate the eigenvalues and eigenvectors. The resulting eigenvectors and eigenvalues of a vector EOF are complex and the EOF vectors are aligned within the EOF frame of reference, not the geophysical frame of reference. In order to interpret the results of the vector EOF, the resulting spatial mode vectors needed to be rotated back to the original geophysical frame of reference. Hodographs of the phase and magnitude of the dominant modes' principle components are shown in Figure 2.7 (right column). The hodographs were used to identify modes that needed to be rotated in order to analyse the results. The hodographs that showed the vector EOF results were tightly aligned along the EOF mode frame of reference, regardless of season or year, indicated modes needing to be rotated. To rotate back to the original geophysical frame of reference, the mode's complex principle components were converted to Cartesian coordinates and the angle of the variance ellipse for each mode was used to rotate the vectors back to zero. These rotated vectors were then used to interpret the results. The rotated vectors are shown in Figure 2.7 (left column).

Twenty years of weekly composite satellite derived sea surface height from AVISO were used in the EOF analysis. The AVISO sea surface dataset consisted of the sea level anomalies plus the long term mean dynamic topography (Ducet et al. 2000), shown in Figure 2.6. Mean

[3]Because EOF results can depend on the dimensions of the grid, three separate boxes were tested 1) a small box just in the lee of the islands, 2) the medium box described here and 3) a large box incorporating most of the Pacific subtropical gyre. The small and large boxes were eliminated because they did not show lee dynamics. The small box was not big enough to catch seasonal changes or the origin of disturbances, and the large box only caught gyre-scale variations, not island induced variability.

Dynamic Topography (MDT) is required to differentiate the sea level anomalies from the long term dynamic height in the ocean. MDT is calculated first as a large-scale guess using 4.5 years of GRACE geoid data and spatial filtering, and refined to smaller scales using in-situ oceanographic measurements, as described in Rio et al. (2013). This MDT was on the order of 1 meter and was removed when the data was detrended before the EOF was calculated, leaving only sea level anomaly (on the order of 0.1 meter). A mean of twenty years of sea level anomaly averages to approximately zero and shows no significant features (Figure 2.6), as expected.

2.3 Drifter Results

Table 2.1 summarizes the characteristics of the 25 anticyclones, including the month and year the drifter first started exhibiting anticyclonic vorticity, the period and radius of the rotation, and the direction and distance the anticyclone travelled. Although the statistics listed here represent the behavior of the drifter in the anticyclone and not necessarily the exact characteristics of the anticyclone, they provide an estimate of the variety of anticyclones seen in Hawaii and are a useful tool to build statistics on these features.

2.3.1 Characteristics of Hawaiian Lee Anticyclones

The 25 anticyclones are spaced out throughout the years that drifter data was available. The first anticyclone appeared in August of 1989 and the most recent (at the time this analysis was completed) was May of 2014. The years with anticyclones were 1989, 1990, 1991, 1994 (x4), 1995 (x4), 2000 (x3), 2001 (x2), 2002 (x3), 2003, 2006, 2009, 2011, 2013, 2014. In 1994 and 1995 an intensive oceanographic survey was conducted and many drifting buoys were released in the lee of Hawai‘i, some directly into anticyclones. This may explain the higher observed numbers in those years. Figure 2.8 is a map of all 37 looping drifter trajectories which make up the 25 anticyclones. To reduce clutter, once the drifter exited the anticyclone, the remaining portion of the drifter tracks were removed. Once in the lee,

the drifters quickly acquired anticyclonic spin and the trajectories are closely packed in the direct lee of the island of Hawai‘i.

For a drifter coming from the east of the Hawaiian islands, there are 5 main pathways into the lee of the islands (shown in Figure 2.9). From south to north, the pathways are 1) entering south of the southernmost tip of the island of Hawai‘i (South Point), 2)‘Alenuihāhā channel, which separates the islands of Maui and Hawai‘i, 3) Kaiwi channel separating Oahu from Moloka‘i, 4) Ka‘ie‘ie channel separating Kaua‘i and Oahu, and 5) north of the island of Kaua‘i. The drifters that became trapped in anticyclones followed similar pathways into the lee of the islands. Most of the drifters which became anticyclonic loopers (23) originated east of the Hawaiian island chain in the latitudinal band 18 °N-20 °N and entered the lee of the islands south of the island of Hawai‘i. 10 anticyclonic drifters originated in the lee of the islands, many of which were deployed during the 1994-1995 survey. Four looping drifters entered the lee of the islands through the ‘Alenuihāhā channel. No drifters that became anticyclones entered the lee of the islands through the more northern Kaiwi channel or the Ka‘ie‘ie channel. For comparison, Figure 2.10 shows the path of loopers versus non-loopers through the two pathways that led to anticyclone creation. The top two maps of Figure 2.10 are maps of drifter pathways through South Point, with *a*) showing the 23 drifters that passed South Point and became anticyclonic loopers and *b*) showing all the drifters which entered the lee of the islands by passing directly south of the island of Hawai‘i that did not become anticyclonic loopers. There were 85 drifters that passed through this region without becoming trapped, as opposed to 23 (27%) that entered anticyclonic vortices. These 85 drifters mostly followed the dominant current patterns after entering the lee, flowing with the NEC towards the west and some heading along the leeward side of the islands as the Hawaiian Lee Current (HLC). There were 9 drifters that passed through the narrow, but deep ‘Alenuihāhā channel without becoming trapped (Fig. 2.10, d), as opposed to 4 (44%) that did (Fig. 2.10, c).

Once in an anticyclone, drifters provide a way to measure the characteristics of the anticyclone and their Lagrangian properties. Although the drifters do not show the exact size or rotation rate of the eddy, they do provide the best observational estimate of different anticyclones. Statistics for the 25 anticyclones are shown in Figure 2.11. The top row in Figure 2.11 shows the month that the anticyclone was first observed in the drifter data (a) and the estimated month the anticyclone was formed (b). The blue errorbars show the mean and standard error bars for 10,000 samples of 25 random data points ranging from 1-12 (corresponding to month). Due to the nature of drifter data, it was necessary to examine both month first observed and estimated formation month for each anticyclone. Some drifters followed the anticyclone from birth, while others entered a pre-existing anticyclone. Month observed is the month the drifter data first started showing anticyclonic looping. Because some drifters joined anticyclones later in the eddy's life cycle, this does not correlate to the month the eddy formed. Based on previous work on anticyclones in Hawai‘i, lee anticyclones form between $156 - 157\,^{\circ}$W, at a latitude just south of the southern tip of Hawai‘i Island (Lumpkin 1998; Flament et al. 2001). The speed and track of each anticyclone was calculated using the mean path of the eddy. The mean path of the eddy connected the center of rotation for each loop. The distance between each center and the time required to advance from one to the next was used to calculate speed of advance of the eddy, for as long as the vortex period and radius remained similar. Mean eddy propagation speeds ranged from $3 - 12$ cm/s, which agree with previous estimates (Wyrtki 1982; Lumpkin 1998; Calil et al. 2008). To estimate when individual anticyclones were formed, based on the speed of advance and track of the mean path of an anticyclone, the vortices could be back-drifted to the known formation region. The month when the vortices reached their closet point of approach to the formation region was used as a best-guess estimate of formation date. The results show a marked difference between the seasonality of month observed versus estimated formation month. The month that the anticyclones were first observed in drifter data was not significantly different than the random data for winter, spring, and summer months. However, the occurrence of anticyclones in fall months (October through December) was

significantly higher than the random data. However, when the observations were corrected to estimated formation month, there was a shift in peak anticyclone appearance. Winter and spring months remained not significantly different than random distributions, but the formation of anticyclones in summer months (July-September) was high, and the formation of anticyclones in fall was below the expected results for a random distribution. Summer months in Hawai'i correspond to stronger and more consistent trade winds, as well as the peak strength of the NEC, both of which are mechanisms capable of spinning up anticyclonic vortices in the lee of Hawai'i (Lumpkin 1998; Wyrtki 1975).

The distribution of observed periods for each of the 25 anticyclones is shown in Figure 2.11 (c). The results are summarized in Table 2.1. The majority of the anticyclone's periods were between 6-13 days (the $25-75\%$ range), however the distribution between 6-13 days is not even. The highest grouping of periods occurs at 3, 6 and 12 days (Fig. 2.11). This agrees with the case studies on vortex merging by Flament et al. (2001); Lumpkin et al. (2000) where anticyclones were found to form near the angular frequency instability limit of $\omega = -f/2$ ($\sim$3 days) and merge downstream into 6 ($\omega = -f/4$), 12 ($\omega = -f/8$), and 24 ($\omega = -f/16$) day period vortices, although no observations of 24 hour periods were made using the drifter data. The distribution of anticyclone periods was fairly narrow. The mean (10.7 days) and median (11 days) were close, indicating little skew in the distribution. The shortest period observed by drifting buoys was 3 days, which is where the Rossby number becomes nearly exactly -1 for the latitude of the southern tip of the island of Hawai'i. Flament et al. (2001) found that the vortices formed in the anticyclonic shear layer in the NEC are nearly immediately limited by centrifugal instability, and do not exhibit a gradual spin up to the instability limit. If we assume that vortices formed off the southern tip of the island of Hawai'i with initial periods at or around 3 days are those formed from the anticyclonic shear layer in the NEC, and that vortices formed in the same area whose initial periods are greater than 3 days or exhibit gradual spin-up have been formed by Ekman pumping from wind stress curl, we can look at an estimate of the ratio of wind

stress to NEC current shear in anticyclone formation. There were 13 anticyclones that formed directly off the southern tip of the island of Hawai'i with drifters that followed the anticyclone from birth. Out of those 13 anticyclones, 9 (69%) had varying periods from 6-13 days upon formation. Of those nine, all but one formed between the months of August to November. This time-frame corresponds to strong and consistent trade winds. Assuming that purely wind-driven anticyclones will behave similarly to purely wind-driven cyclones, we can narrow these nine anticyclones down again. Wind-driven cyclones display gradual spin-up, generally stay close to the lee of the islands, and are of shorter duration than anticyclones (Lumpkin 1998; Calil et al. 2008; Jia et al. 2011). Of the nine anticyclones which displayed gradual spin-up, only two remained near the lee of the islands, and both were of short duration. The other seven anticyclones, except for a gradual spin-up displayed properties similar to those anticyclones previously shown to be driven by the shear instability in the NEC. These anticyclones may have been formed by a combination of wind stress curl and anticyclonic NEC shear instability, however further research is necessary before concrete conclusions can be drawn about the role of each forcing mechanism. In contrast, four anticyclones (31%) had periods of almost exactly 3 days upon formation. These four anticyclones formed in February, March, April, and June (one in each month), when trade wind gusts can be greatest, but due to Kona winds bursts, is more sporadic. This would indicate that the centrifugally-limited half-inertial flow eddies were more common in late winter and spring, except previous research indicates that the North Equatorial Current is weakest during this period (Meyers 1975; Wyrtki 1975; Wyrtki and Kilonsky 1984). This contradiction underlies the need for an updated examination of the current strength and variability off of South Point, Hawai'i, an area which has to date, very limited oceanographic observations.

The mean radius of the observed anticyclones was 63.8km, with the majority of the anticyclones having radii in the range of 43-83km, consistent with previous observations of drifters entrained in anticyclonic vortices (Lumpkin 1998; Flament et al. 2001). Flament

	Median	Mean	Standard Deviation
Period (d)	11	10.7	±5.2
Radius (km)	52.5	46.9	±22.1
Month	8	7.4	±3
Track (°T)	264	260	±19.2
Distance (km)	350	556	±434.3
Persistence (d)	63.3	75.5	±49.9

Table 2.1: Statistics for the 25 anticyclones

et al. (2001) found that radii estimated from drifting buoys was smaller than radii estimated from satellite altimetry, indicating the drifters were entrained in the center of the vortex. In general, both period and radius increased away from the islands, as the anticyclone moved downstream (Figure 2.13). There were a few exceptions where anticyclones started with long periods and large radii during initial spin-up, and eventually increased in strength until they were fully developed with periods around 6 days, consistent with wind-forcing.

The anticyclones followed a defined path away from the lee of Hawai‘i. The mean track was 260.7 °T with the $9-91\%$ ranging from just 235-281 °T, which defines a very narrow anticyclonic sector originating in the lee of Hawai‘i and extending out in the south-west direction to 170 °W, a distance of $\sim 1500km$. The size and shape of the pack of loopers is in remarkable agreement with the theoretical anticyclonic sector of Hawai‘i's wake described in Lumpkin (1998), however the orientation of the anticyclonic zone is not even with the island of Hawai‘i, as referenced in Lumpkin (1998) and Yoshida et al. (2010). As seen in Figure 2.8, the anticyclonic zone orients more to the south west, below the 19.5°N HLCC belt, with the far western tip almost dipping down to 16°N.

2.4 EOF Results

2.4.1 Wind Stress Results

The NE trade winds dominant the surface wind patterns around the Hawaiian Islands, as seen in Figure 2.6 (top), which shows the 10-year mean surface wind stress magnitude

and direction. Wind direction is primarily from the ENE at around 0.05 to 0.08 N/m^2 in the vicinity of the islands, consistent with findings in Sasaki et al. (2010). Figure 2.14 is the monthly mean wind stress magnitude and direction. The color bar scale for all months is identical. Monthly means show a slight seasonal fluctuation in the magnitude of the NE trades around Hawai‘i, although magnitudes remain fairly steady, ranging from 0.044 N/m^2 to 0.056 N/m^2 (Table 2.2 outlines the mean, maximum, and standard deviation for each month). Figure 2.15 is the spatial mean for each month and shows that peak mean winds occur in April, dropping quickly to minimum winds in May, strengthening again for a relative maximum in July, and dropping again for a relative minimum in September. Some of the variability in the mean monthly winds can be explained by seasonal changes in wind direction. Although the dominant wind direction is from the northeast, there can be large variability in wind direction during winter months, when the NE trade winds can occur as low as 50% of the time (Sanderson 1993; Garza et al. 2012). In winter months, Hawai‘i can be influenced by Kona winds. Kona winds are winds from the south-west or south-south-west, opposite the direction of the NE trade winds. Kona winds were first explained by Daingerfield (1921). Kona winds occur when low pressure systems are within 500 miles northwest of the islands. Due to the counterclockwise and inward flow around atmospheric low pressure systems, this creates winds from the south-west in the vicinity of Hawai‘i. The presence of Kona winds in wind data from the Honolulu airport is shown in Figure 2.16. These are daily mean winds at the Honolulu airport. Most of the time the wind is coming from the northeast, however, there are episodes when the wind reverses and becomes southwest. These Kona wind systems occur mostly in December-February and can persist for weeks at a time. However, shorter events may not be visible in the Quikscat data, due to the 8 day rolling vector composites.

Opposing wind stress curl dipoles are observed in the lee of the major islands, as previously shown in Chavanne et al. (2002), but are confined relatively near to the islands. These wind stress curl dipoles create regions of Ekman pumping (downward velocities) and suction

Table 2.2: Monthly statistics (maximum, mean, and standard deviation) from 10 years of Quikscat wind stress (N/m^2)

$Month$	Max	$Mean$	$stddev.$
Jan	0.072	0.045	±0.012
Feb	0.075	0.047	±0.013
Mar	0.079	0.049	±0.011
Apr	0.099	0.057	±0.011
May	0.077	0.044	±0.011
Jun	0.098	0.049	±0.009
Jul	0.113	0.052	±0.008
Aug	0.105	0.051	±0.009
Sep	0.093	0.044	±0.008
Oct	0.084	0.048	±0.009
Nov	0.080	0.048	±0.011
Dec	0.084	0.052	±0.014

(upward velocities) from:

$$w_e = curl\frac{\tau}{\rho f} \tag{2.7}$$

Mean Ekman pumping rates (in m/day) are shown in Figure 2.17, with a strong area of Ekman pumping on the south side of the island of Hawai‘i and a strong region of Ekman suction on the north side of the island of Hawai‘i, regions know to create anticyclonic and cyclonic eddies, respectively (Jia et al. 2011; Calil et al. 2008; Lumpkin 1998). Ekman pumping is consistent throughout the year, however summer months exhibit the longest westward extent of Ekman pumping off the southern tip of the island of Hawai‘i.

In order to look at spatial fluctuations in the flow field, the mean was removed from the wind stress data. The application of EOF methods to the detrended data yielded spatial EOF modes and their accompanying principle components. Based on the cumulative variance represented by each mode (Figure 2.18), the first three modes were kept for analysis. After the third mode, the percent variance became small, the separation between modes decreased, and the slope of the line was near constant. These modes were eliminated to reduce noise in the dataset in order to focus on the dominant modes. The first three

modes represented 81% variance in the wind stress. Modes 1 and 3, whose spatial patterns can be seen in Figure 2.7 (left column) both have a distinct seasonal cycle. The spatial pattern of Mode 1 mimics the dominant NE trade winds. This mode in itself represents 53.7% of the variance in the winds around Hawai'i. These fluctuations are mostly like the time modulation of the strength of the trade winds throughout the year. The mean monthly principle components for Mode 1 (shown in Figure 2.19,top) show the strongest fluctuations in the strength of the trade winds occurs in winter, consistent with the standard deviations listed in Table 2.2. The NE trade winds are steadier in the summer, which is reflected in the principle components. The spatial pattern in Mode 2 (which has a dominant period of 50 days), represents 19.7% of the variance, is an west-east oscillation between NE trade winds and SW winds. This mode is strongest in the winter (February), and weakest in the summer (Figure 2.19, middle). This pattern resembles the development of Kona winds from low pressure systems during winter in Hawai'i. Additionally, the phase of Mode 2 is most variable in winter and relatively similar for all other seasons (Figure 2.7, right column, middle). The spatial pattern of Mode 3, which represents 7.6% of the variance, is a north-south oscillation of the trade wind magnitude, with strongest magnitudes in winter, and weaker magnitudes in summer (Figure 2.19,bottom). The rotary spectra of each mode's principle components is Figure 2.7 (center column). The dashed line marks a period of 365 days for modes 1 and 3. The dashed line on mode 2 is 50 days. Modes 1 and 3 show strong annual cycles, while mode 2 is missing a yearly component. The right column in Figure 2.7 are hodographs of the complex principle components' angles and magnitudes for each mode, color coded by season. Regardless of season, modes 1 and 3 were tightly aligned in the hodograph. These angles were used to rotate the vectors back to geophysical space, as described in the methods. The dominant wind modes range from 10% to 20% of the magnitude of the mean wind stress and the spatial patterns of that relationship are shown in Figure 2.20. The top plot shows the magnitude of the mean wind stress, and the bottom three show the magnitudes of the modes normalized by the mean wind stress (units are dimensionless).

2.4.2 Sea Surface Height Results

Once the long term mean dynamic height was removed, the sea level anomalies in the region of Hawai‘i were evaluated. Although the mean sea level anomalies over the 20 year period did not reveal any patterns (Figure 2.6), monthly means reveal seasonal patterns in sea level anomalies in the lee of Hawai‘i (Figure 2.21). Patterns in the monthly mean sea level anomalies show minimal disturbances in the lee of the islands from February through June. Eddy activity peaks August until December, with positive anomalies in excess of 10 cm in the lee of the island, and slows down as the end of the year approaches. The positive anomalies in the lee of the island of Hawai‘i generally follow the anticyclonic sector south of the HLCC. Eddy kinetic energy (EKE) was calculated using the associated AVISO geostrophic currents using the same definition provided earlier in Eq. 2.2. Figure 2.22 shows the spatial EKE patterns derived from the AVISO geostrophic currents. The satellite-derived geostrophic currents are highly variable in the vicinity of Hawai‘i. In order to examine the lee region of Hawai‘i, data was extracted for an area encompassing the direct lee of Hawai‘i, from (18 °-21 °N,180 °-155 °W). The mean spatial average for each month is shown in Figure 2.23. The highest EKE occurs in August and September, while the lowest value of EKE occurs in January and April.

EOF analysis was applied to the SLA data first using conventional EOF methods, and second using a complex EOF. The conventional EOF results, unlike the wind stress EOF results, spanned more than three modes. In order to represent the major patterns in sea level anomaly in the lee of Hawai‘i, 7 modes were needed. Because the modes in SLA appear to be propagating features, a complex EOF was performed on the data as well, bringing the number of modes needed to explain the variance down to 4. This brought together the different phases (modes) of a propagating feature seen in a conventional EOF into one mode. The first mode and its accompanying principle components from the CEOF of sea level anomaly is shown in Figure 2.24. As mentioned earlier, the spatial patterns of EOFs can be summed using:

$$\left(\sum_{i}^{N} EOF_i^2 / var_i \right)^{\frac{1}{2}} \tag{2.8}$$

where the squares of EOF modes i through N are summed, and normalized by their percent variance, var_i. The resulting spatial pattern and magnitude of the sum of conventional SLA EOF modes 1-3 is nearly identical to the first complex SLA EOF mode shown in Figure 2.24 (top). This complex EOF represents the seasonal fluctuations in SLA in the Hawaiian region, the timeseries of the principle components for CEOF mode 1 is shown in Figure 2.24 (bottom), which has a distinct annual peak in its spectra (Figure 2.25). SLA CEOF modes 2 and 3 had interannual timescales and were not included here for analysis. However, CEOF mode 4 (shown in Figure 2.26) depicts a persistent zonal sea level anomaly feature in the lee of the island of Hawai'i, centered at 19.5 °N, very similar to the sum of conventional EOF modes 6 and 7. Additionally, the principle component timeseries has a distinct peak at 100 days (Figure 2.27). These two complex modes, 1 and 4, represent the annual and 100 day fluctuations in sea level in the vicinity of Hawai'i, respectively.

At first glance, the low percentage of explained variance, even in the leading modes, could be considered suspicious. However, unlike the wind stress EOF, the sea surface height data does not have a true mean removed before conducting the EOF. The mean wind stress removed from the Quikscat data clearly showed the NE trade winds, as expected. The remainder of the data is variations from this expected mean flow. The mean sea surface height removed from the data here is the MDT described in the methods, which is unrelated to SLA. Removing the mean sea level anomaly before calculating the EOF does not impact the results due to the negligible values of the mean anomalies. This could be one reason why the percentage of variance explained is low, it resembles an EOF calculated without removing the mean first. Additionally, in order to see spatial patterns, the EOF was calculated using the gridded sea surface height data, meaning that the gridded data is interpolated from the spatially and temporally sparser along-track data, adding to noise in the EOF results. One method to verify EOF results was to analyze time-series of sea

level anomalies at specific locations directly from along-track data. The time-series of sea level anomaly from specific locations in the Hawaiian region confirmed the results of the gridded sea level anomaly EOF results. Transformation of 8 different locations (two to the east of the islands, and 6 to the west of the islands) into the frequency domain revealed matching periods with the gridded EOF results. All locations showed a strong seasonal cycle. The two locations upstream to the east of the islands did not have a 100 day period in their spectra. However, the six locations to the west showed a 100 day signal in their spectra, with stronger 100 day peaks in the HLCC zone and the anticyclonic zone south of the HLCC (Figure 2.28).

2.5 Discussion

There was mostly good agreement between the anticyclone results gathered from the surface drifting buoys and the eddy activity results inferred from the satellite sea level anomaly and seasonal wind forcing data. The drifter results showed that anticyclone formation was most common in summer months (July-September) when both the NEC and wind forcing are thought to be the strongest. However, the seasonal strength of the NEC is still unclear. Results from the monthly mean sea level anomalies concur with the drifter results. The strongest anticyclonic eddy activity (highest positive sea level anomalies) occurred in August through December. The associated EKE in the lee of Hawai‘i also peaks in August and September, matching the peak anticyclone activity noted in the drifter data. So how does this correlate with wind signals? Peak NE trade winds occur in April (but quickly diminish to a minimum in May) and peak again July through September. The strongest and most consistent NE trade winds occur in the summer months. In winter, the winds may be gustier, leading to high averages, but the proportion of Kona days increases, making the forcing less reliable. Winter months also have the shortest westward extent of Ekman pumping, meaning the ocean is less conditioned for anticyclone development. Where the results disagree some is the formation rate of anticyclones in the fall. According

to the drifter observations, formation in the fall (October-December) was statistically low. This does not match the observed monthly mean sea level anomalies or EKE. The sea level anomalies and EKE are a minimum February-May. During these months, anticyclone formation observed in the drifter data was average. Whether the discrepancy is a sampling bias in the drifter observations, or related to NEC forcing, which is still undetermined, is unknown at this time.

The results from the EOF analysis show distinct annual cycles in wind forcing and the sea level anomalies. There is also a 50 day signal in the second mode of the wind stress EOF and a 100 day signal in the 4th mode of the CEOF for sea surface anomalies. From here, two questions arise. Is the 50 day signal seen the in the wind stress related to or in phase with the 100 day signal seen in the sea level anomalies? And secondly, are either of these signals related to the presence of the large anticyclonic zone in the lee of Hawai'i?

If the 50 and 100 day signals are related, then potentially the 50-day cycle observed in the wind stress EOF mode 2 could be forcing the 100-day signal seen in the sea level anomaly CEOF mode 4. Figure 2.29 is a comparison of the respective wind mode 2 and SLA mode 4 EOF temporal amplitudes. In order to determine a cross correlation, the higher temporal frequency wind data was interpreted onto the same sampling frequency as the lower resolution SLA data. A lag correlation, shown in the bottom of Figure 2.29, shows low correlation values ($< 15\%$) at all potential time lags. This indicates that there is little correlation between the strengths of the two signals and that these modes are not related.

If the 100 day signal seen in sea level anomalies was caused by the presence of anticyclones, it is expected that the spatial phases of the CEOF mode would line up with the anticyclonic zone detected in the drifter data. The shape of the anticyclonic sector seen in Figure 2.8 was outlined by taking the outermost limits of the cluster of rotating vortices. Two outlines are shown. The smaller one is the outline of the tightly packed anticyclones. The larger one is the outline including a few outlying anticyclones at the western edge. These shapes were

then overlaid on to the SLA CEOF modes 1 and 4 (Figure 2.30). At first glance it appears that neither mode lines up well perfectly with the anticyclonic sector. The anticyclonic sector in the drifters extends all the way to the island of Hawai'i at 155°W. Neither mode extends that far west. However, the near lee sea level anomalies (using satellite data) have been shown by Yoshida et al. (2010) to have periods of 60 days. This frequency does not match the frequency of either mode, meaning its signal would not be visible in these representations. Yoshida et al. (2010) found that the near lee had a period of 60 days and that anticyclones formed in this region were wind-driven, as the signal matched a 60 day wind signal. However, the 100 day period they noted further downstream could not be explained by wind. The area they noted as Region-W had a 100 day period and was located along a zonal line centered at 19.5°N and extended from $162-166$°W. This location and the 100-day period matches what is seen in SLA CEOF mode 4. The analysis here extended beyond 170°W to 180°W, and a second region, an extension of Region-W exists out to that longitude. However, this region, does not align well with the observed anticyclonic sector from the drifters. The anticyclonic sector tilts to the southwest, heading of ~ 260°T. Region-W extends almost purely zonally at heading 270°T, this most closely matches the core of the HLCC, not the anticyclonic sector. However, there is a weaker signal in CEOF mode 4 that aligns well with the anticyclonic sector, indicating that the anticyclones could be related to a portion of the 100 day signal. Additionally, if we allow for the fact that drifter lifespans may have reduced the number of drifters to make it west through the life of the anticyclone, the spatial pattern in mode 1 is the closest to the anticyclonic sector. Knowing that the 60-day signal near the immediate lee of Hawai'i is not visible in mode one due to the annual pattern, and looking at the extent of the drifters in Figure 2.8, the anticyclonic zone could extend out, weakly, to 180°W. If the sea level anomaly mode 1 does match with the anticyclonic sector, given those assumptions, then the annual seasonal cycle in the ocean, caused by the annual seasonal variations in wind forcing, could be forcing the anticyclonic zone. If so, the time series of the EOF modes would align. Figure 2.31 shows the mode 1 SLA (blue) compared to the combined annual signal seen in wind modes 1 and

3. There is a 6 month periodic lag between the signals. Considering the distance from the formation zone to the edge of the anticyclonic sector, 1500km, and the mean speed of the anticyclones ($\sim 10\, cm/s$), this makes sense.

Although anticyclones were observed during every season, there was only one season where anticyclones formed at significantly different than random values, the summer months. This also corresponds with decreased disturbances in the wind stress annual EOF modes, and the peak monthly averages of wind speed calculated earlier. In order to determine if the anticyclones are caused by shear instability in the NEC, high resolution spatial and temporal current measurements are necessary. In an attempt to gauge the potential of ocean stresses as a cause of vorticity for the anticyclones, we looked at both the satellite derived geostrophic currents and OSCAR currents.

Since SLA is known, geostrophic currents can be inferred from the changes in sea surface height due to the geostrophic balance, where the pressure gradient force is balanced by the Coriolis force:

$$fv = \frac{1}{\rho}\frac{\partial P}{\partial x} \qquad -fu = \frac{1}{\rho}\frac{\partial P}{\partial y} \tag{2.9}$$

where u and v are the zonal and meridional geostrophic velocities, ρ is the density, and P is the pressure. Since pressure is difficult to measure, the geostrophic balance equations can be re-written in terms of sea surface height η using the hydrostatic balance, $P = \rho_o g(\eta - z)$

$$fv = g\frac{\partial \eta}{\partial x} \qquad -fu = g\frac{\partial \eta}{\partial y} \tag{2.10}$$

Geostrophic currents were available from AVISO using the same merged-satellite database from 1992 until 2014. AVISO uses a 9-pt stencil width to calculate the geostrophic currents, where stencil width is the number of grid points used to estimate the derivative on a grid using finite differencing (Arbic et al. 2012). The mean geostrophic currents (Figure 2.32, top) do not reflect the mean large-scale wind-driven geostrophic currents, but instead show the mesoscale fluctuations in the Hawaiian region. This can also been seen the variance of

the geostrophic currents, which is strongest directly in the lee where eddy activity is high (Figure 2.32, bottom). In addition to the geostrophic velocities measured from sea level anomalies, another satellite-derived surface current measurement is available: NOAA's OSCAR (Ocean Surface Current Analyses-Real time) measurements. OSCAR currents differ from the base-level geostrophic currents because it also includes the local wind-driven Ekman currents into the analysis. The Ekman momentum balance represents a balance between the Coriolis force and the windstress:

$$fv_e = -\frac{1}{\rho}(\frac{\partial}{\partial z}\tau_{zy}) \qquad fu_e = \frac{1}{\rho}(\frac{\partial}{\partial z}\tau_{zy}) \tag{2.11}$$

where u_e and v_e are the Ekman currents in the zonal and meridional direction, f is the Coriolis parameter, ρ is the density, and τ_{zx} and τ_{zy} are the zonal and meridional wind stress. NOAA uses a linear combination of geostrophic and Ekman currents to calculate OSCAR currents, however the MDT (discussed in above) is removed in favor of the mean annual 0-1000 dbar dynamic height from Levitus (ESR 2009; Bonjean and Lagerloef 2002). The OSCAR currents are available at 1° and $1/3^\circ$ degree resolution. The mean currents are shown in Figure 2.33. The $1/3^\circ$ degree resolution surface currents were used for this research. The EKE in the mean OSCAR currents is highest in the NEC region in the southern section on the area of interest (Figure 2.34, top). The variance, however is highest in the direct lee of the island of Hawai‘i.

While both ocean current sources confirmed the presence of persistent vortices, neither the AVISO based geostrophic currents or the OSCAR currents had a high enough resolution to detect fluctuations in current velocity near South Point, Hawai‘i. Also, as both estimates of currents are derived from the very satellite data used to conduct the EOF analysis, their results would not explain anything outside of what is already known with these data sets. Without the necessary data on current structure as the NEC separates from Hawai‘i, shear instability cannot be ruled out as a forcing mechanism for the anticyclones. This means that until further high resolution data is available for the velocity off of South Hawai‘i, the

null hypothesis cannot be ignored: wind stress curl is forcing the anticyclones in the island's lee. This is shown by the overlap between the annual mode EOF in wind stress and the structure of the anticyclonic sector.

Regardless of their forcing mechanism, the anticyclones play a large part in the island lee dynamics. The anticyclonic sector extends over 1500km downstream from Hawai'i. It is worth noting that of the 832 drifters, there were only three cyclones discovered, one of which passed south of the anticyclonic sector, leaving only two observed cyclones in the theoretical cyclonic sector. This is compared to the 25 anticyclones in the dataset. The anticyclonic sector shown in Figure 1.1 is reasonable in size, but the cyclonic sector shown was not visible in this dataset. This could be due to interactions with the wakes of other islands (Chapter 3). The anticyclones, on the other hand impact the flow patterns not only in the wake of the island, but downstream. Figure 2.36 shows the mean currents calculated from all non-looping drifters. The westward NEC is clearly visible upstream of the Hawaiian Island chain. Reaching the islands it bifurcates, with part heading along the windward side as the Northern Hawaiian Ridge Current, part passing south of Hawaii and turning north to flow along the leeward side of the island chain as the Hawaii Lee Current, and then finally, a portion passing south of Hawai'i undisturbed. This is the expected circulation described earlier. Mean drifter-derived speeds south of the island of Hawai'i average $10\,cm/s$. When mean currents are calculated using only the anticyclonic loopers, the flow in the vicinity of Hawai'i changes (Figure 2.35). The northward flowing Hawaii Lee Current is reversed on the leeward side of Hawai'i with the flow moving from North to South along the Kona coastline. Also, the presence of the anticyclones intensifies the separation off of South Point, Hawai'i. Mean speeds along the southwest oriented convergence zone average $20\,cm/s$, double what is present without the anticyclones. The flow is also more southerly, as seen in Figure 2.37. The zonally averaged meridional velocity calculated from near the island out to 160°W adds negative, southward flow to the normally zonal NEC. This could mean that anticyclones are forming when the NEC is stronger, or the anticyclones are actually helping to create

the strength in the NEC. So preexisting vortices are priming the region for further shear instability and preconditioning the ocean for vortex development.

2.6 Conclusion

The anticyclonic zone in the lee of Hawai‘i is well defined by drifter observations. These anticyclones are most likely to form during summer months when the wind stress forcing is at its strongest. However, anticyclones have been observed in every month of the year. An examination of the wind stress forcing and the sea level anomalies showed an annual cycle in both forcing mechanisms. The windstress induced annual cycle represents seasonal variability in the trade winds. The sea level anomaly annual cycle shares similar spatial properties to the anticyclonic sector shown by the drifters when higher frequency cycles are removed. The 100 day signal seen in higher order SLA modes has a weaker segment that resembles the drifter's anticyclonic sector, but the main signal is too zonal and does not align with the vortices. Instead, this signal sits at the latitude band of the HLCC. If the weaker portion of the signal is indeed the anticyclones, it could indicate there is a strong connection between the HLCC and the anticyclones at this frequency. Due to a lack of reliable and high resolution data on current structure and variability to the south of the island chain, the null hypothesis that these anticyclones are wind-driven cannot be disproved.

AC#	Start Date	Period (d)	Radius (km)	Track (°T)	Distance (km)
1	08/89	6,16	17,51	254	343
2	08/90	3	26	277	105
3	11/91	12.5	58.5	259	748
4	02/94	3	11.5	300	266
5	03/94	3,6,12	11,48,76	246,277	1363
6	10/94	6,11	58	290,259	1182
7	11/94	11,14	44,49	262	402
8	08/95	6	56	226	260
9	10/95	12	66	237	808
10	10/95	12	53	270	414
11	11/95	7,12	28,56	215,281	234
12	07/00	13	38	260	350
13	09/00	13	48	268	284
14	10/00	27,21	78,53	270	254
15	04/01	3	11	249,279	427
16	08/01	10,13	64	261	1614
17	06/02	6,11	63,53	S,S	157
18	10/02	13,12	66,105	244	291
19	11/02	14	53	268	284
20	06/03	3,6,7,9	27,26	267	1456
21	06/06	6	18	270	887
22	10/09	18	41	238	210
23	01/11	7	22	267	781
24	03/13	10	27	270	501
25	05/14	12,6	58,27	235	282

Table 2.3: Characteristics of the 25 Anticyclones identified via drifting buoys. Anticyclones that displayed multiple distinct radii, periods, or tracks are noted as multiple entries for the same Anticyclone. S means stationary.

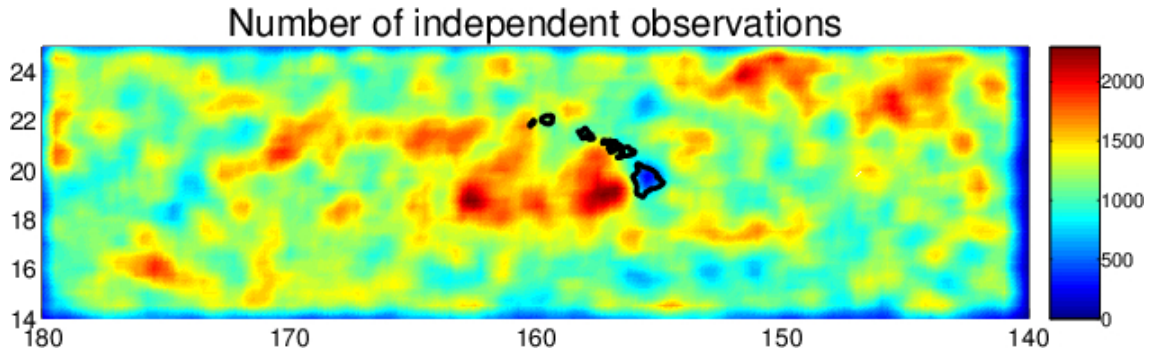

Figure 2.1: Number of SVP drifter observations in each 0.25° box.

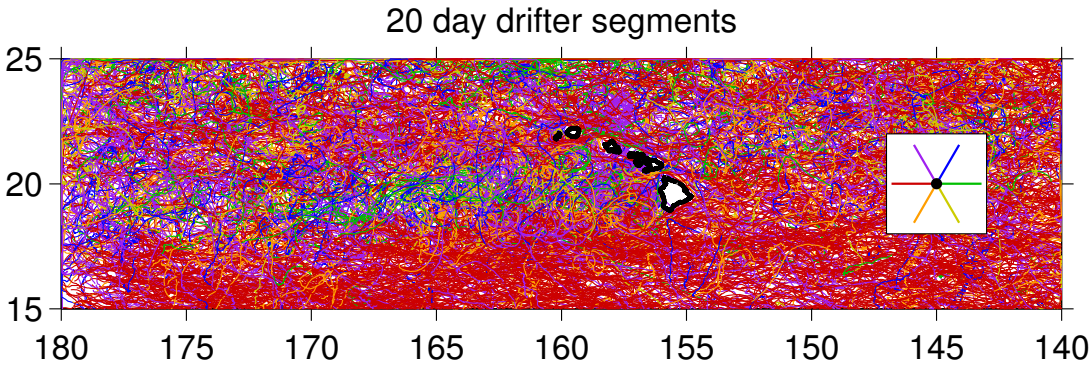

Figure 2.2: Surface Velocity Program drifter data from 1979-2016, broken down into 20-day drift segments.

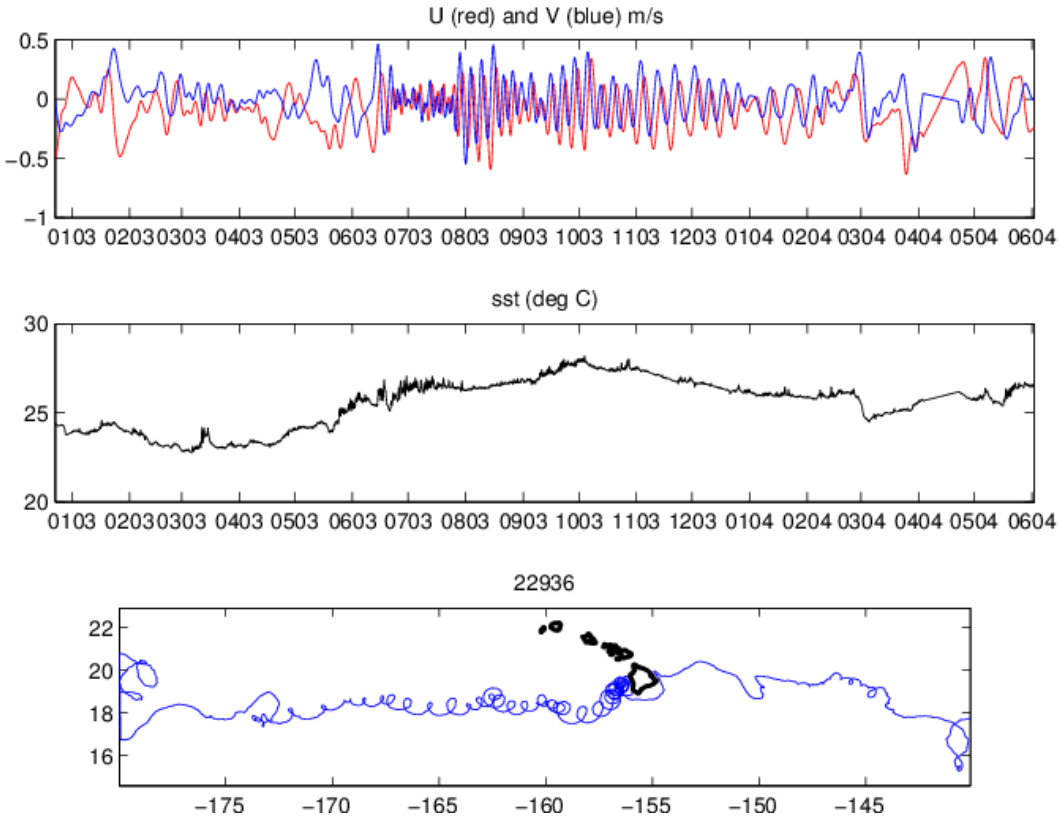

Figure 2.3: Anticyclone 20. Top: zonal (red) and meridional (blue) velocities of the drifter with time (mmyy). Middle: Sea surface temperature of drifter with time (mmyy). Bottom: Drifter track.

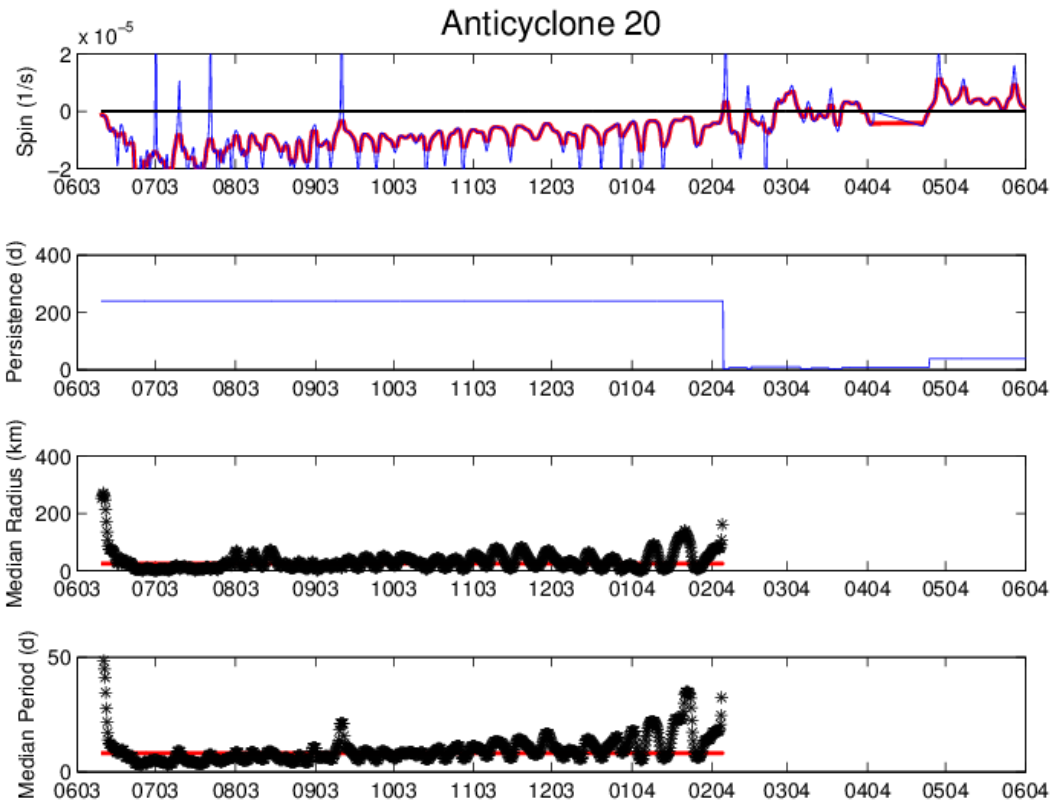

Figure 2.4: Anticyclone 20. The x-axis for all is time in mmyy. Top: Spin (s^{-1}) of the drifter over time. Middle (top): Persistence (days) of drifter. Middle (bottom): Radius (km) of anticyclone only when persistence meets cut-off criteria. Bottom: Period (days) of anticyclone only when persistence meets cut-off criteria.

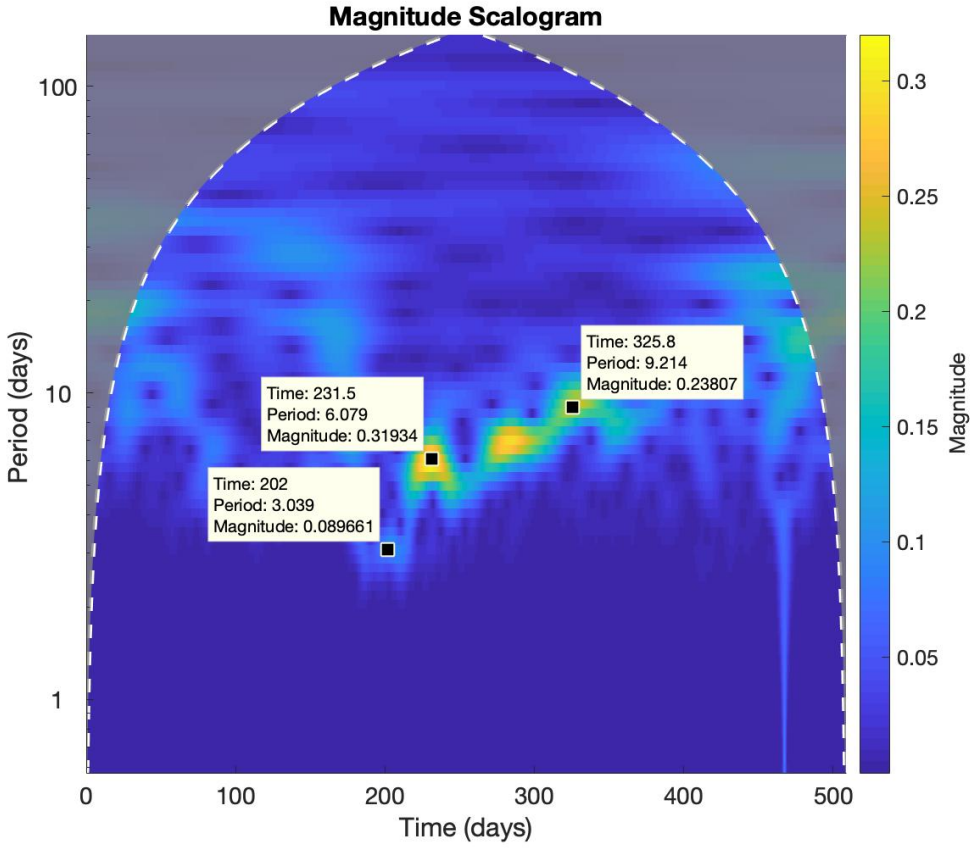

Figure 2.5: Continuous Wavelet Transform analysis of Anticyclone # 20 showing the time-frequency analysis of the drifter's zonal velocity

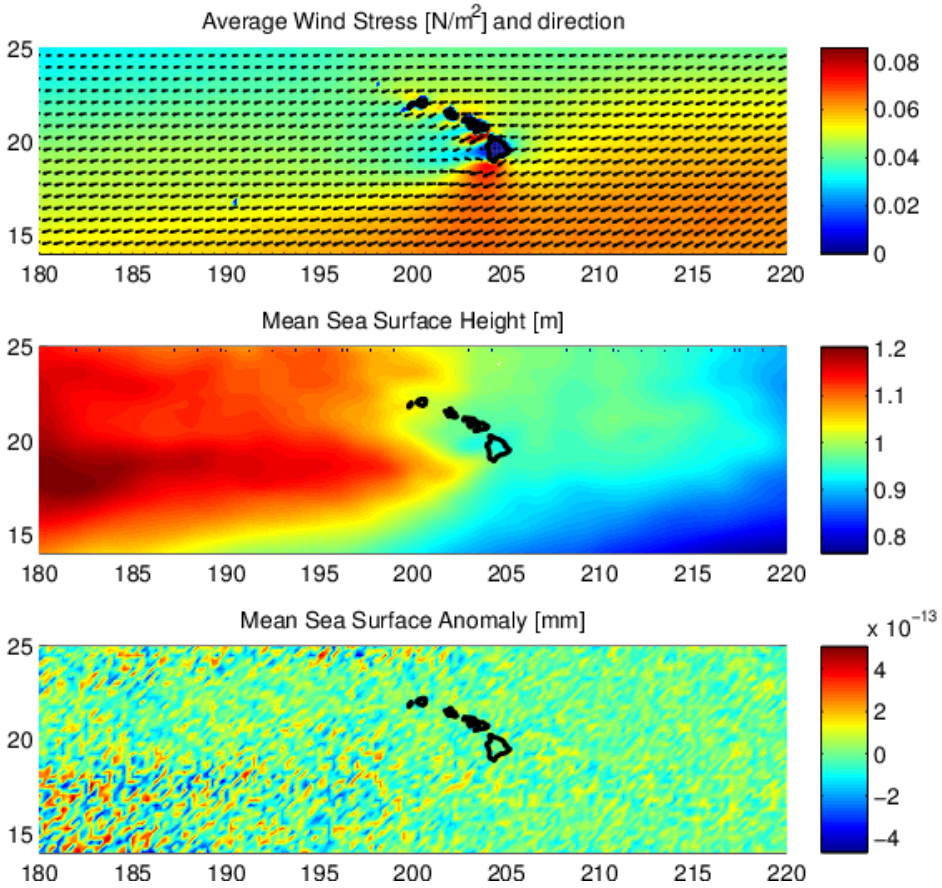

Figure 2.6: Mean wind and sea surface fields calculated from satellite-derived data. (a) Mean wind stress (N/m^2) and wind direction from 10 year QuikScat record. (b) Mean sea surface height (m) in AVISO sea surface height data. This is the long term mean dynamic height which needed to be removed in order to examine sea surface height anomalies. (c) After the mean dynamic height was removed, only sea surface anomalies remained. A 20 year mean of sea surface anomalies averages to zero.

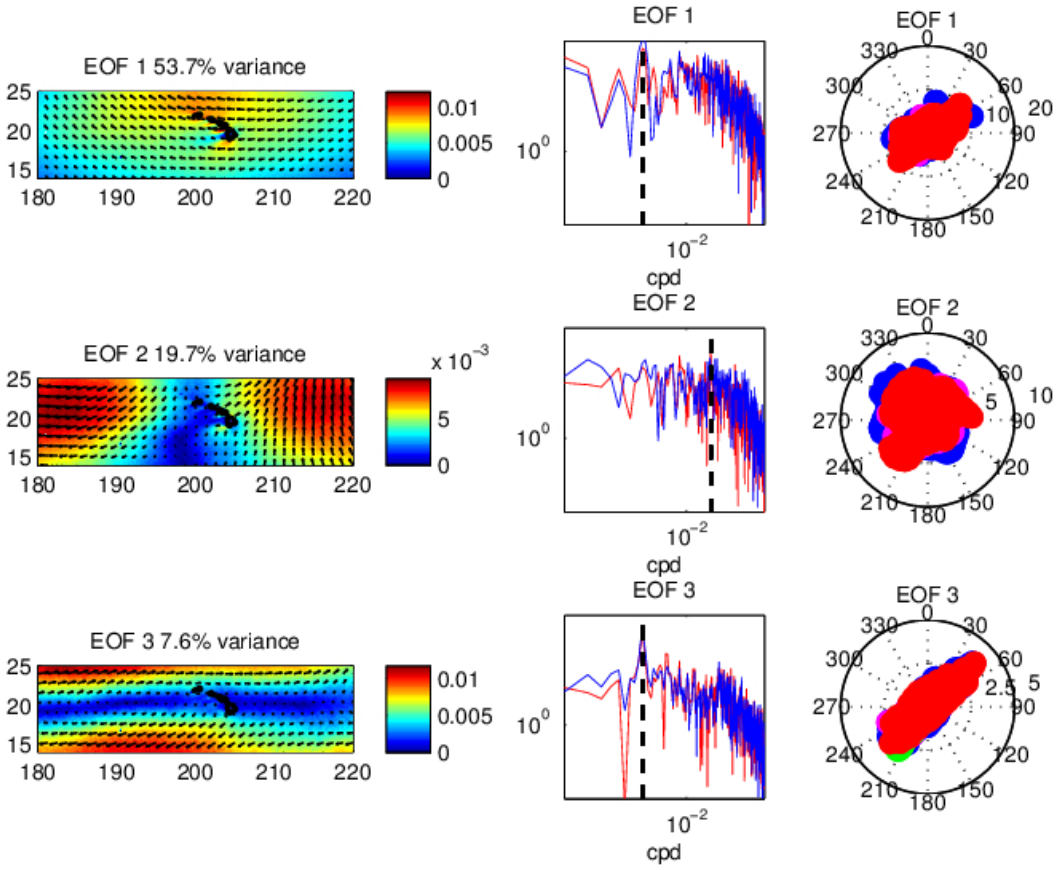

Figure 2.7: The first three wind stress EOF modes, accounting for 81% of the variance in the wind. (Left Column) The spatial EOF patterns for modes 1-3, in N/m^2. (Center Column) Spectra of EOF modes 1-3 principle components. Blue is clockwise, Red is anticlockwise. Dashed lines in mode 1 and 3 show the annual frequency. The dashed line in mode 2 shows a 50 day period. (Right Column) Hodographs of EOF modes 1-3 amplitude timeseries, color coded by season (Blue=winter, Magenta=Spring, Green=Summer, Red=Fall. The superposition of all the colors by season indicates good alignment in the EOF space)

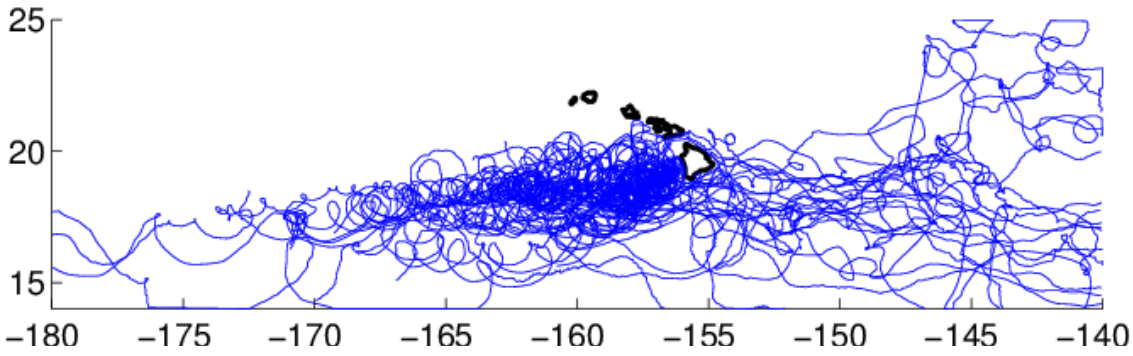

Figure 2.8: All 37 anticyclonic looping drifting buoy tracks. For clarity, the path of drifters after exiting anticyclones was removed.

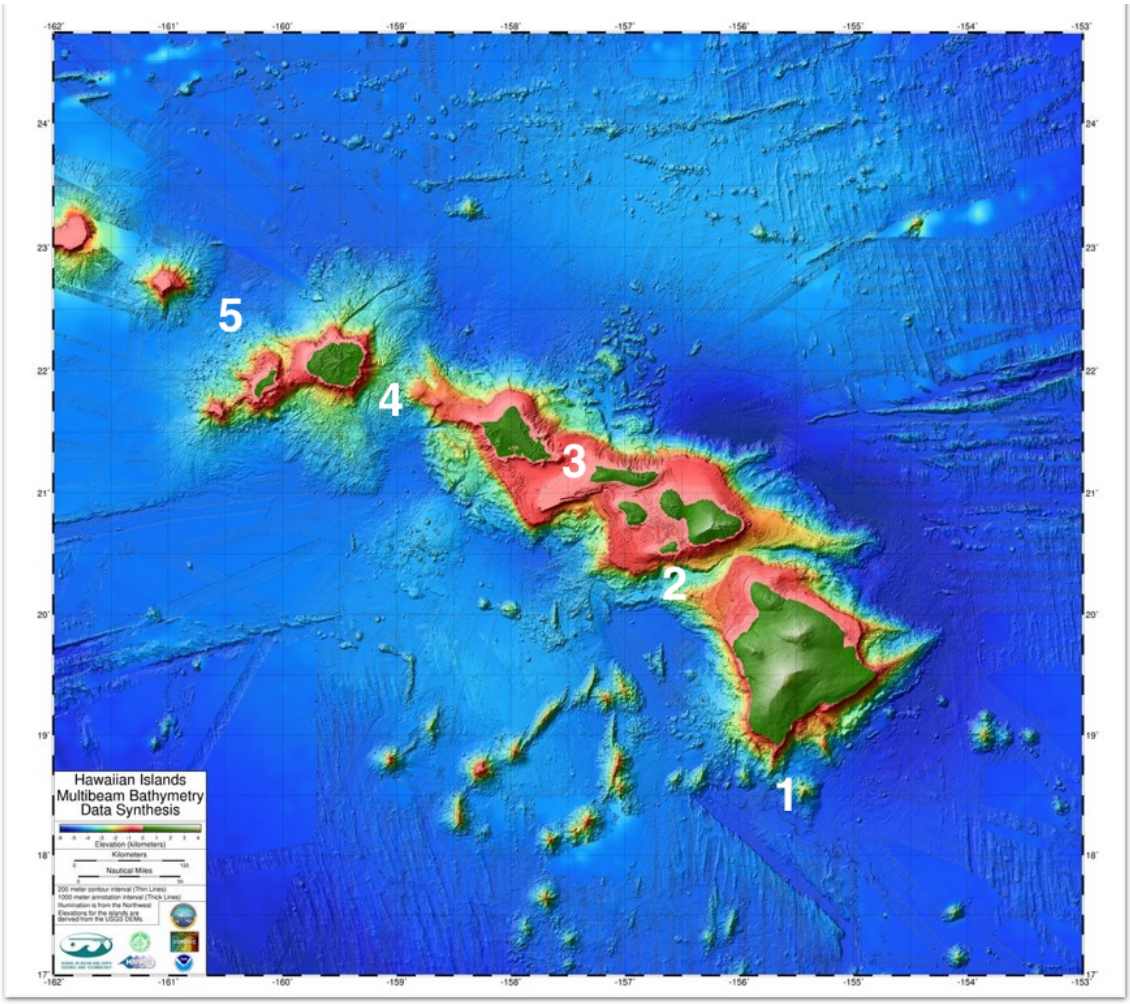

Figure 2.9: The 5 main channels or pathways into Hawaiian waters for a drifting buoy coming from the east. 1) South of the southernmost tip of the island of Hawai'i (South Point), 2) 'Alenuihāhā channel, 3) Kaiwi channel, 4) Ka'ie'ie channel, and 5) North of the island of Kaua'i. Background image from Main Hawaiian Islands Multibeam Bathymetry and Backscatter Synthesis.

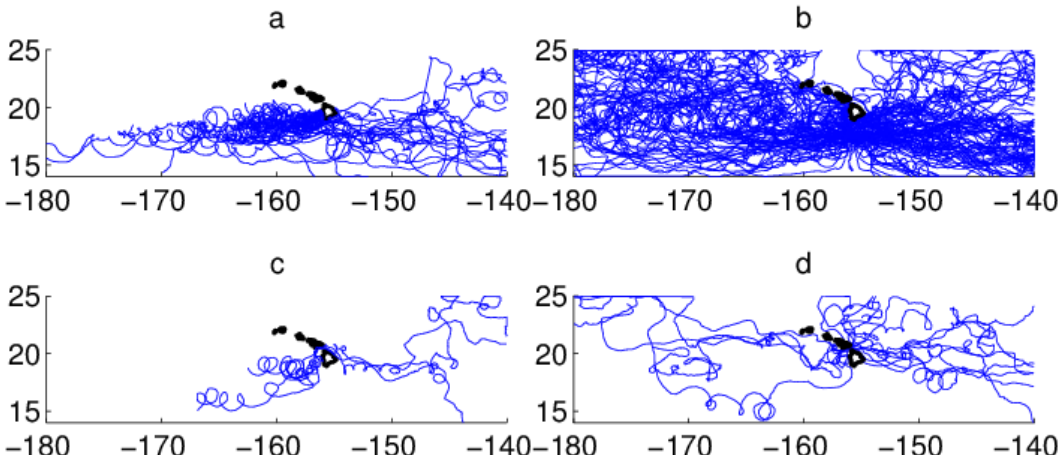

Figure 2.10: a) Anticyclonic loopers that entered the lee of the islands by passing south of the island of Hawai'i. b) All non-loopers that entered the lee of the islands by passing south of the island of Hawai'i. c) Anticyclonic loopers that entered the lee of the islands by passing through 'Alenuihāhā channel. d) All non-loopers that entered the lee of the islands by passing through 'Alenuihāhā channel.

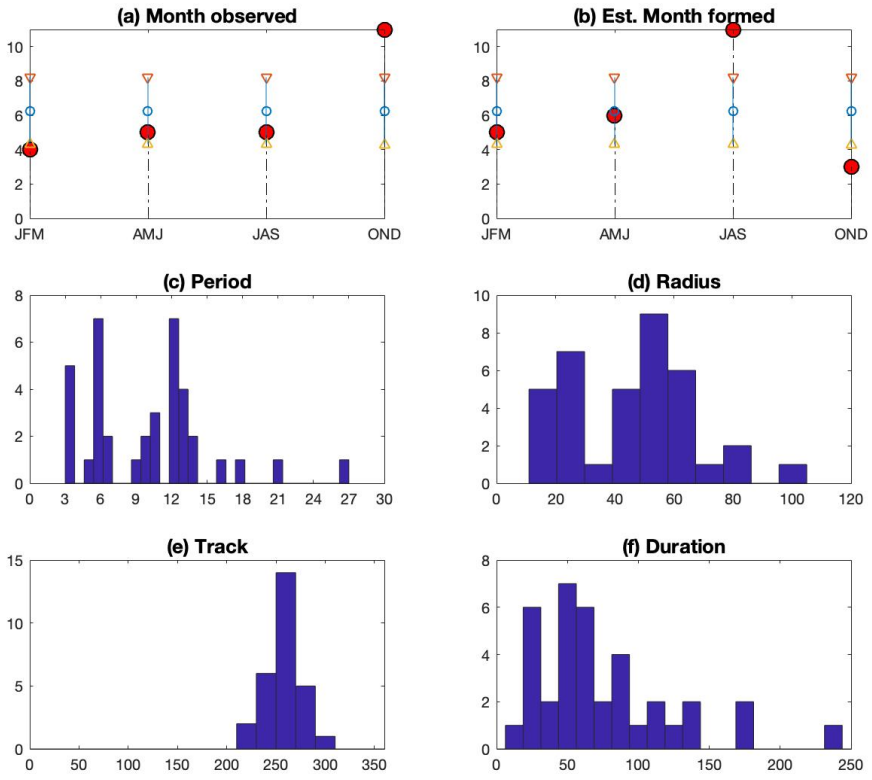

Figure 2.11: Histograms of Anticyclone characteristics. a) Month anticyclone was first observed in the data. Red circles are the observed values from the anticyclonic drifters. Blue circle and triangles represent mean and 95% confidence intervals for 10,000 random samples of 25 months. b) same as a), except this is estimated month the anticyclone was formed. c) Period (in days) of the 25 anticyclones d) Radius (in km), e) Track (in degrees True), and f) Duration (in days)

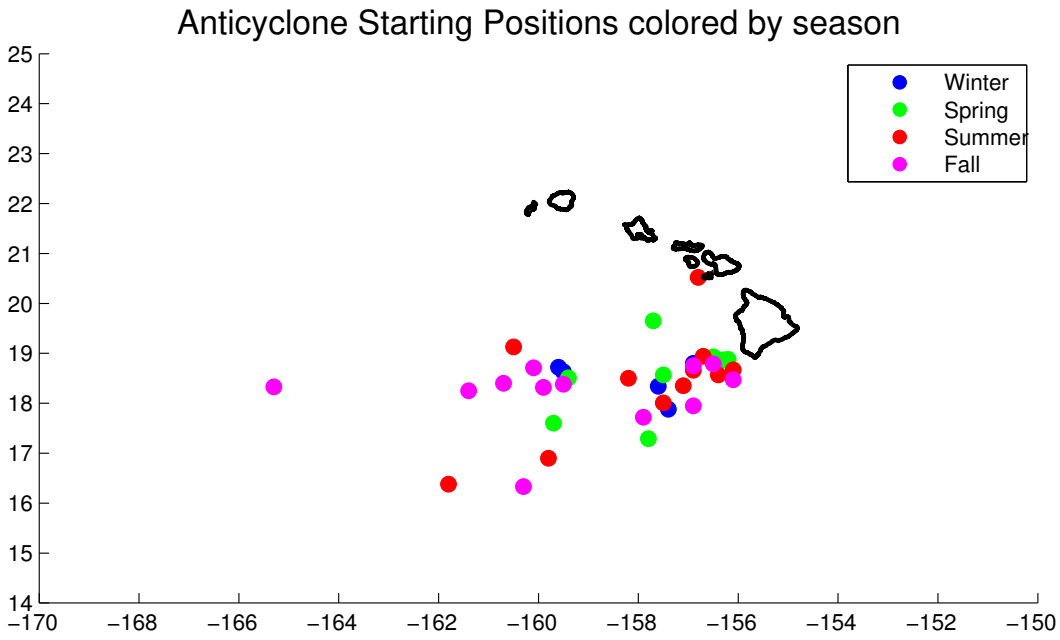

Figure 2.12: Anticyclone locations color coded by season.

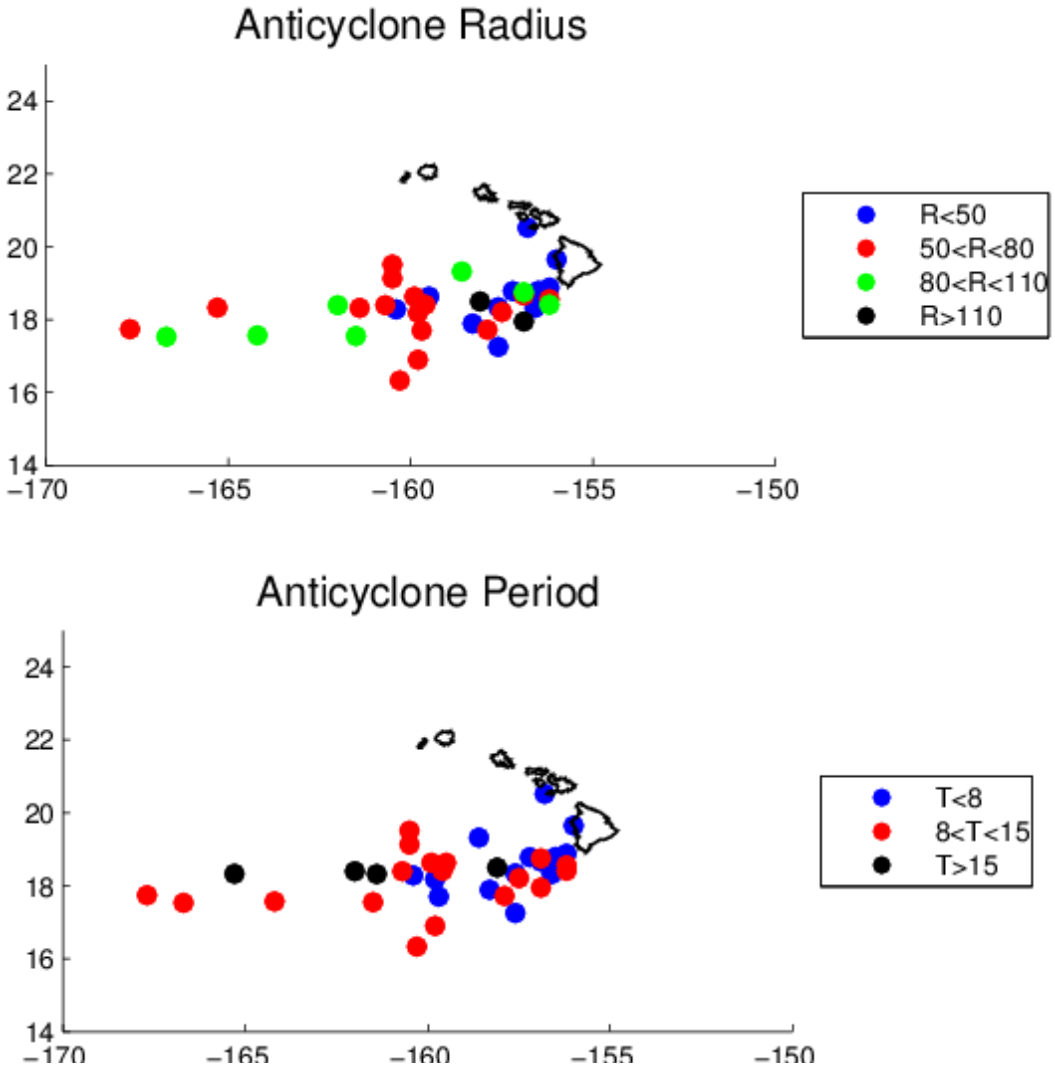

Figure 2.13: Top: Anticyclone locations color coded by radius. Bottom: Anticyclone locations color coded by period. Blue: Periods <10 days, Red: Periods>10 but <20 days, Black: Periods >20 days.

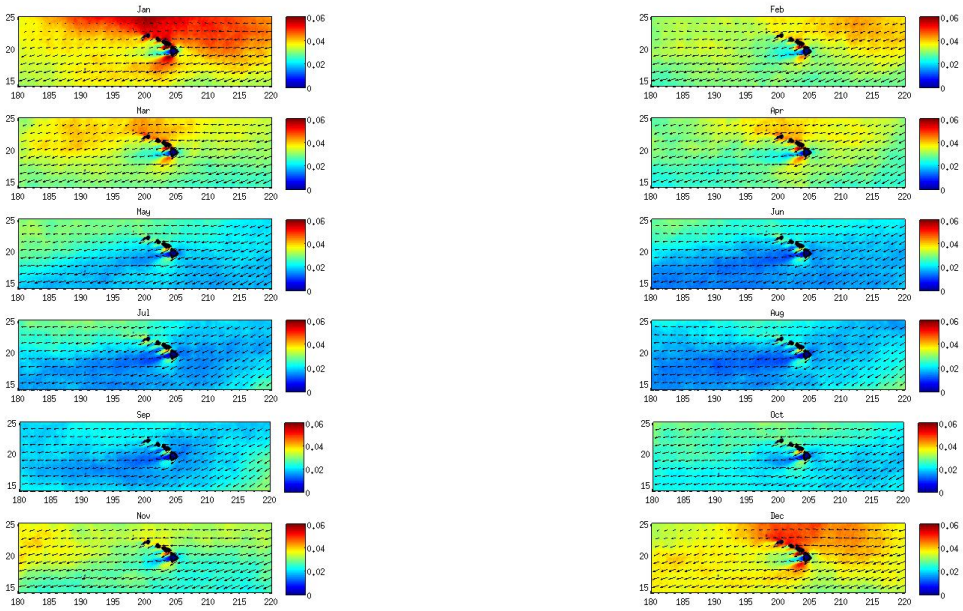

Figure 2.14: Mean wind stress (N/m^2) and direction over 10 year QuikScat record broken down by month.

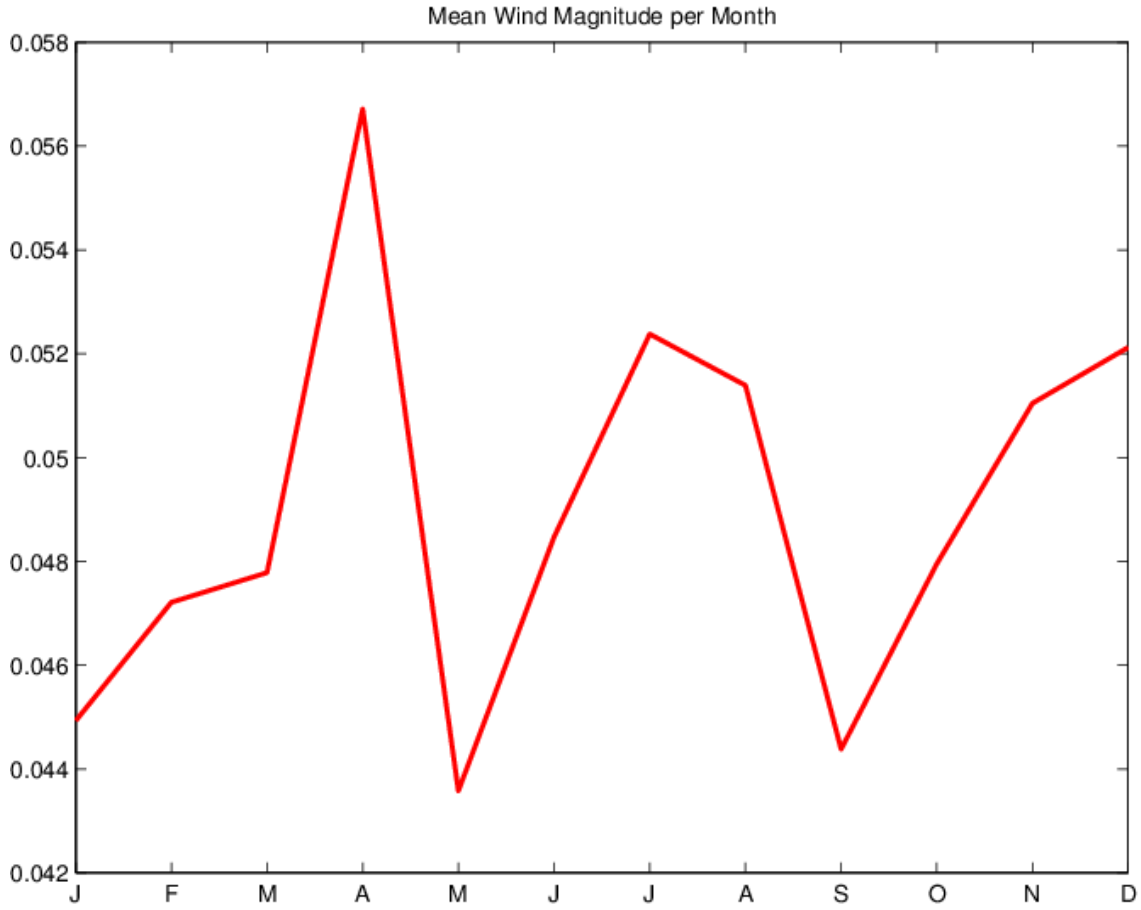

Figure 2.15: Spatially averaged mean wind stress (N/m^2) over 10 year QuikScat record for each month.

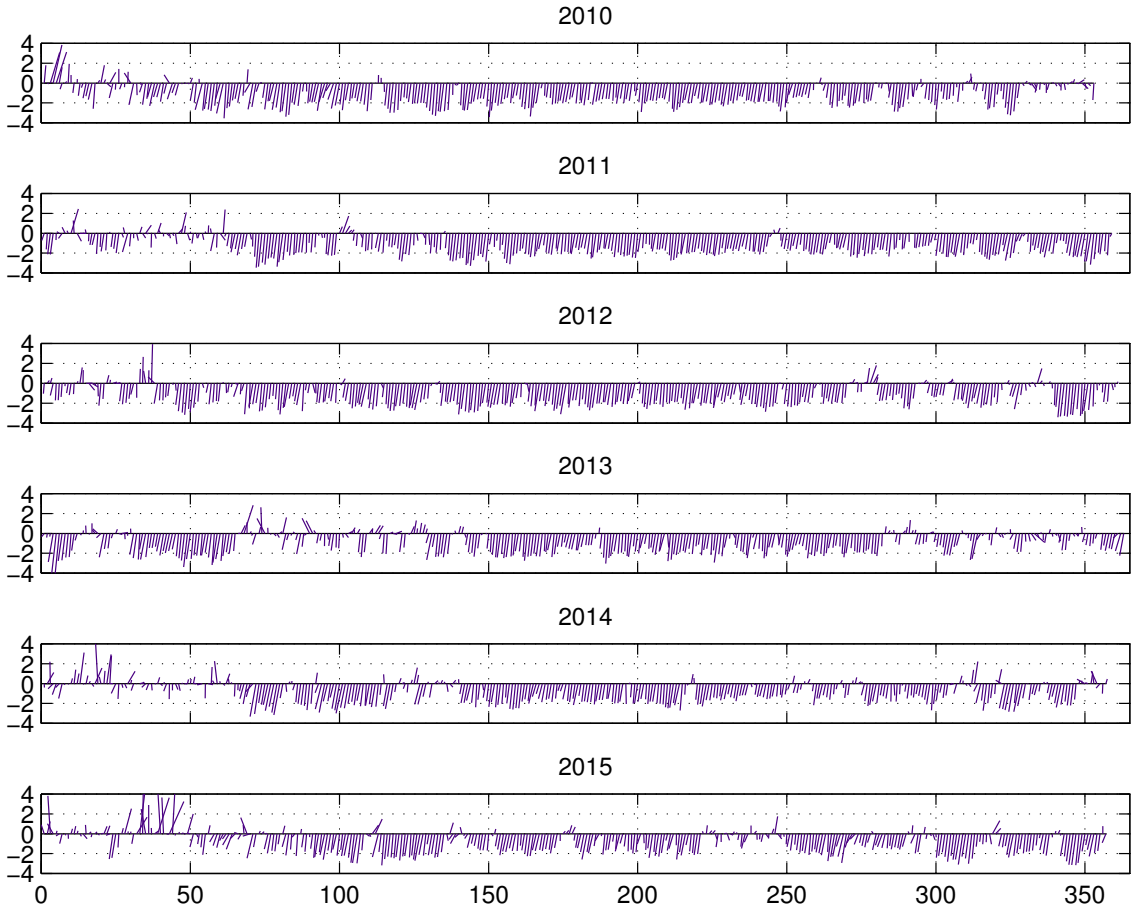

Figure 2.16: Daily Mean Wind Speed and Direction from Honolulu airport 2010-2015. The x-axis is the numbered day of the year.

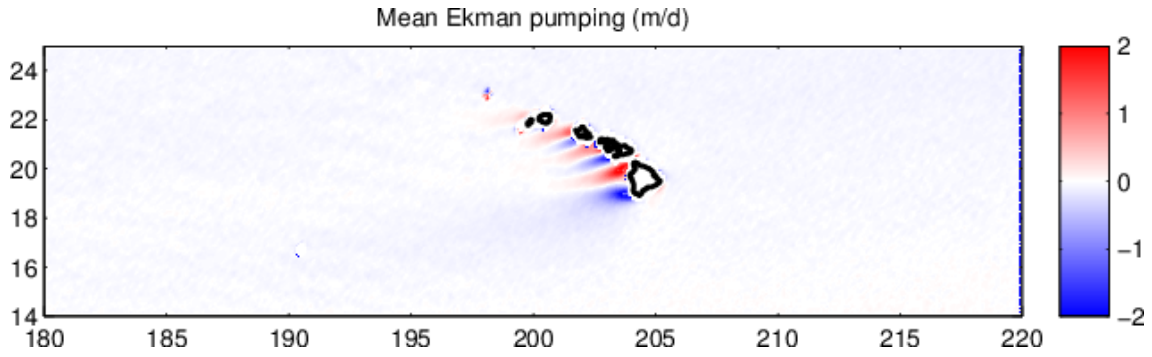

Figure 2.17: 10 year mean Ekman Pumping velocity in meters per day.

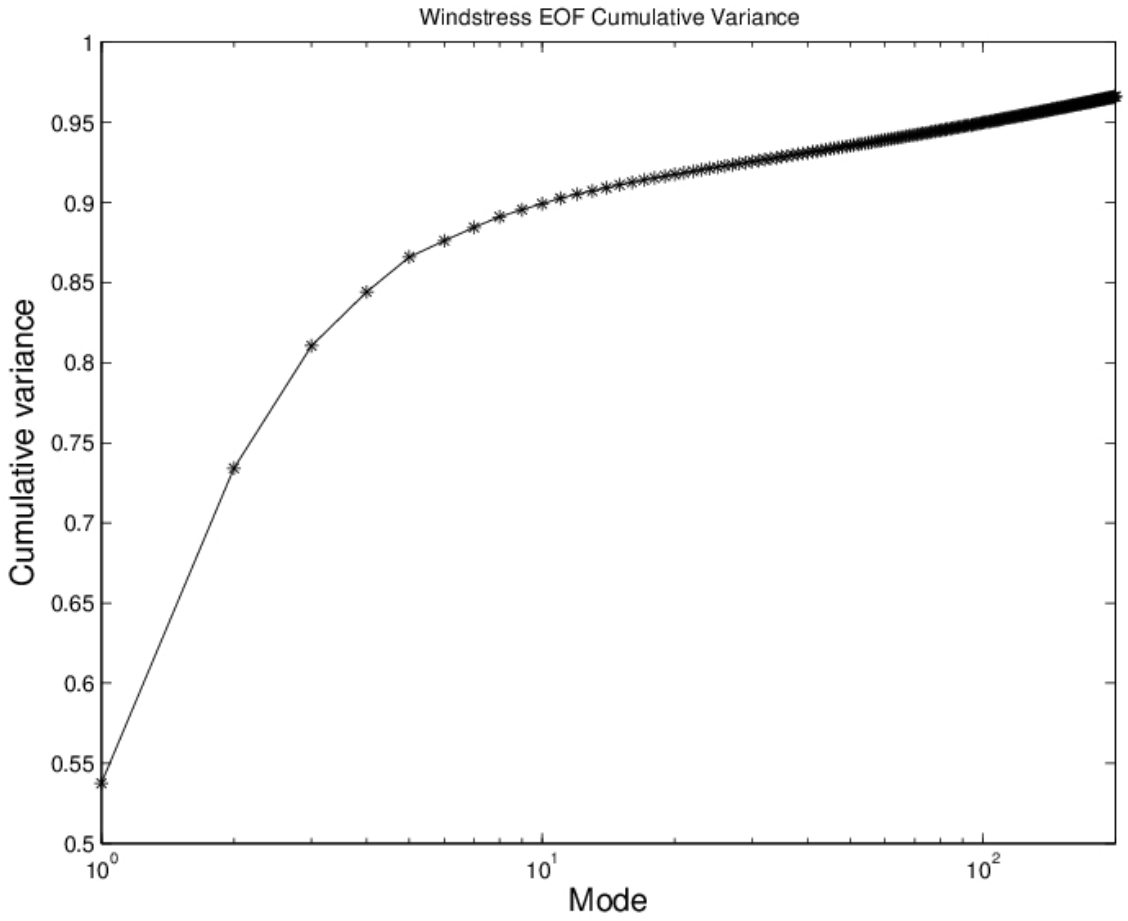

Figure 2.18: Cumulative varaince plot for the Windstress EOF. The x-axis is logarithmic in scale. The y-axis is cumulative variance.

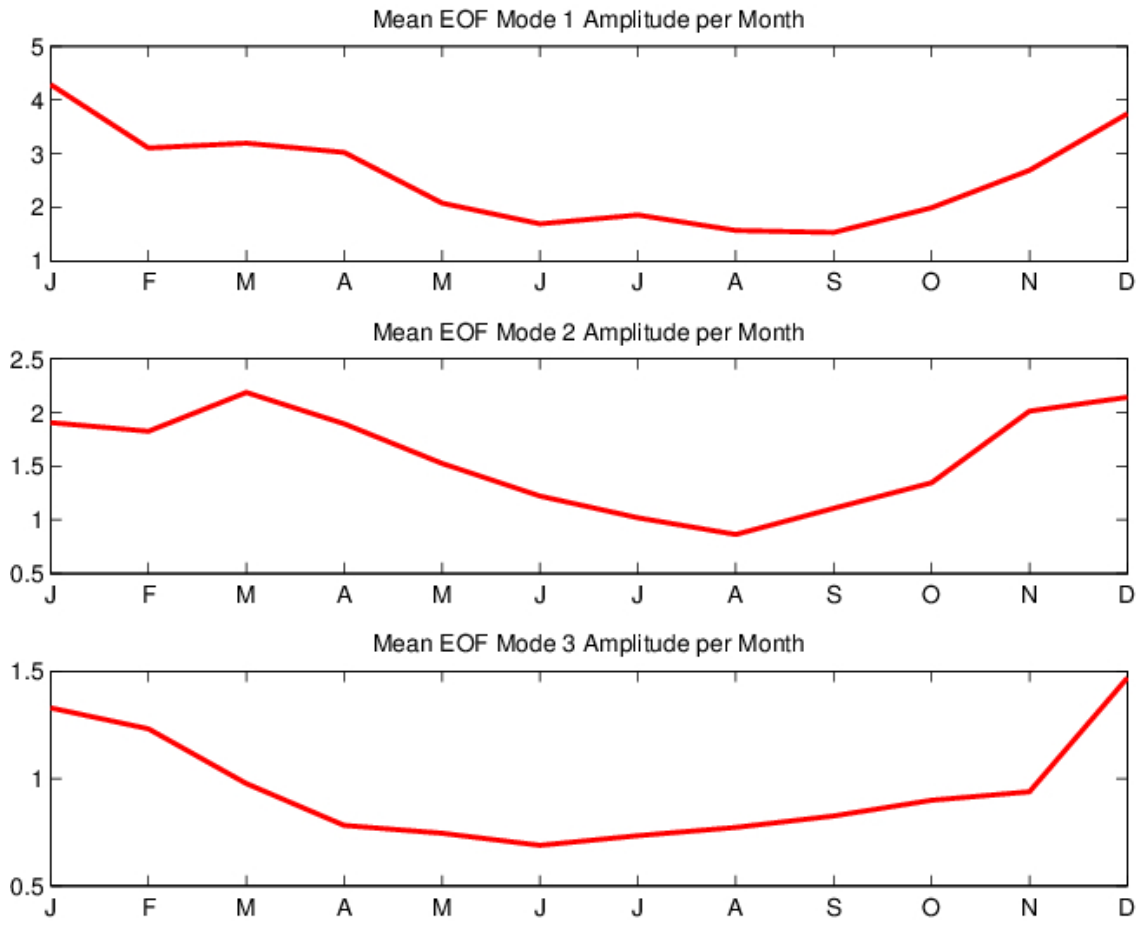

Figure 2.19: Mean monthly windstress EOF timeseries amplitudes for mode 1 (top), mode 2 (middle), and mode 3 (bottom).

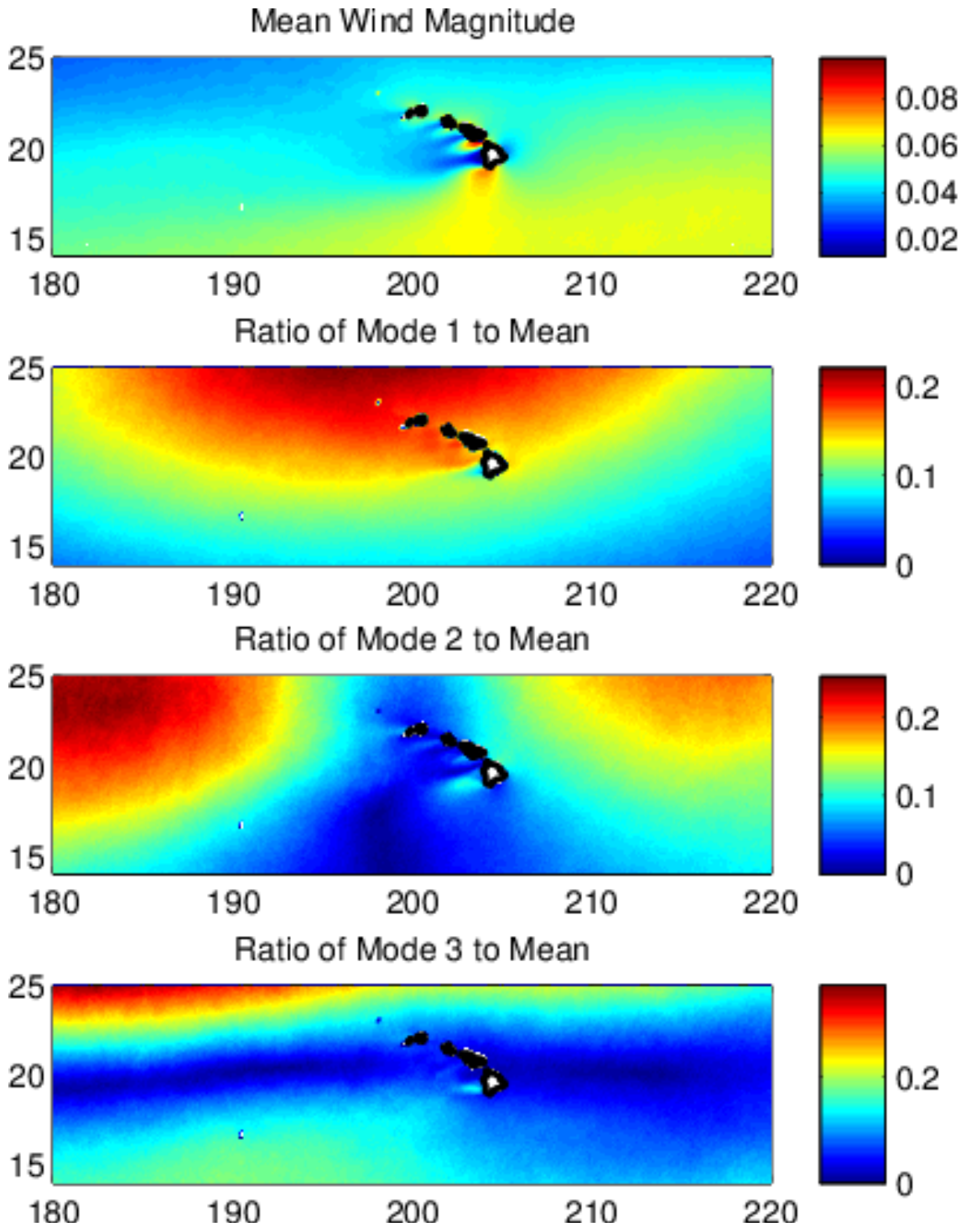

Figure 2.20: (a) Mean wind stress (N/m^2), (b) EOF mode 1 normalized by the mean wind stress shown in (a) above, (c) same as (b) but for Mode 2, (d) same as (b) but for Mode 3.

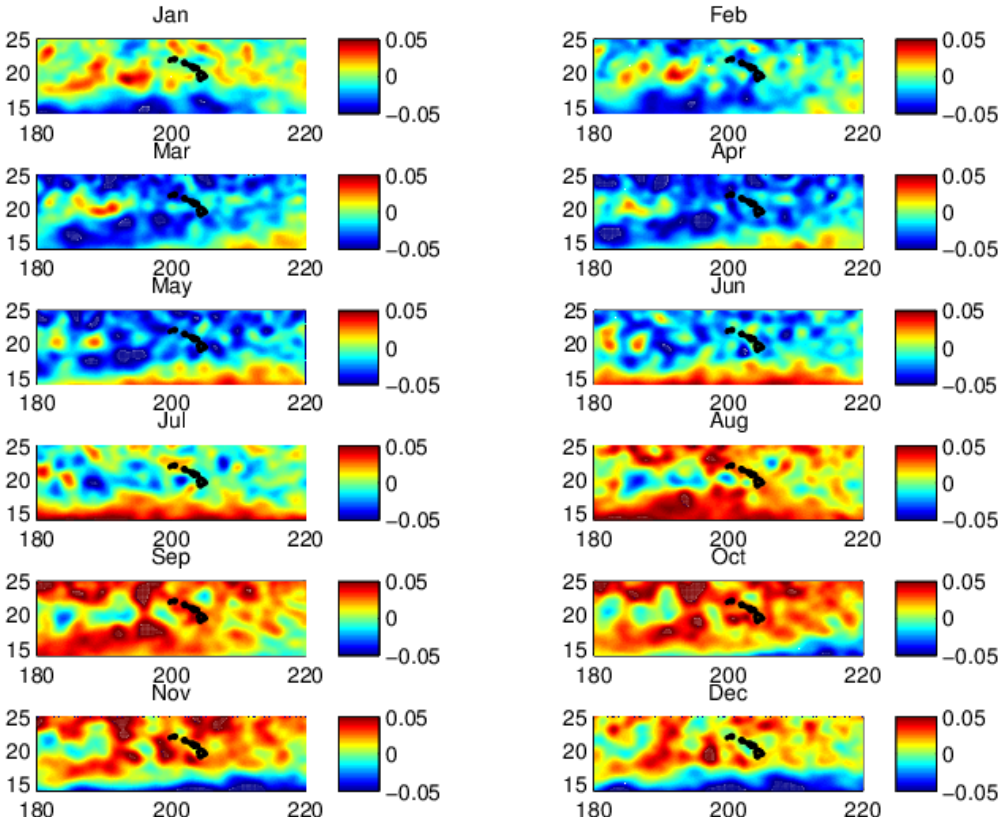

Figure 2.21: Mean sea surface height anomalies (m) for each month.

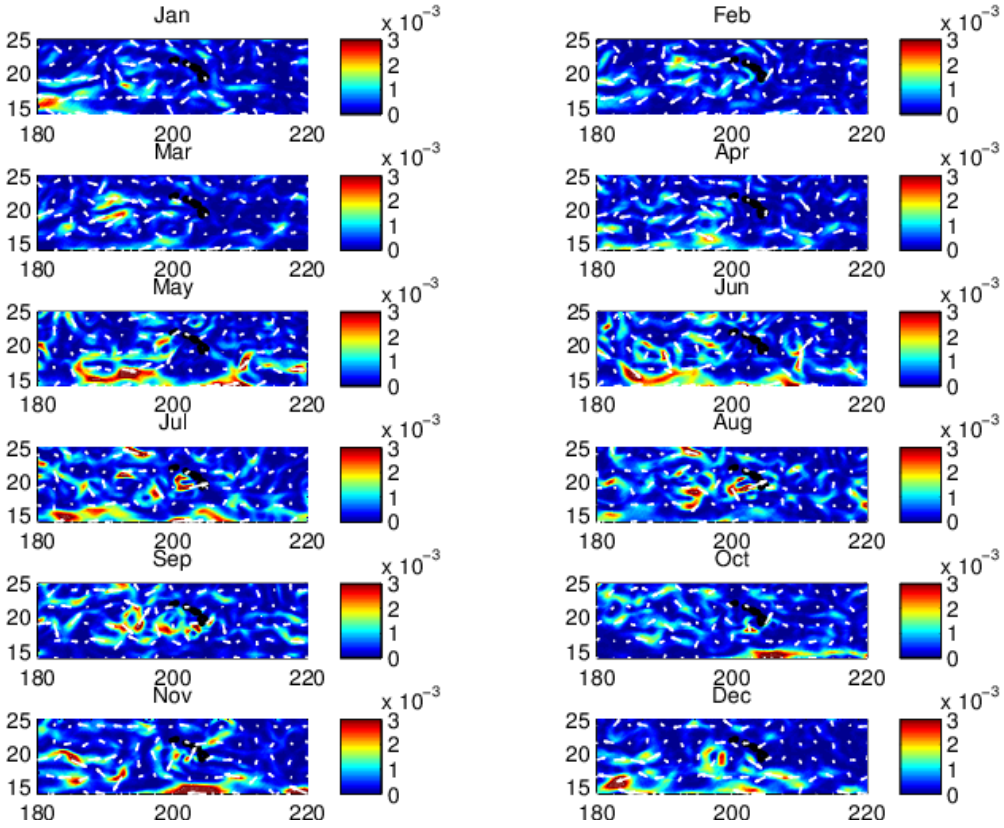

Figure 2.22: Mean monthly EKE from AVISO geostrophic Currents in m^2/s^2 in the lee of Hawai'i.

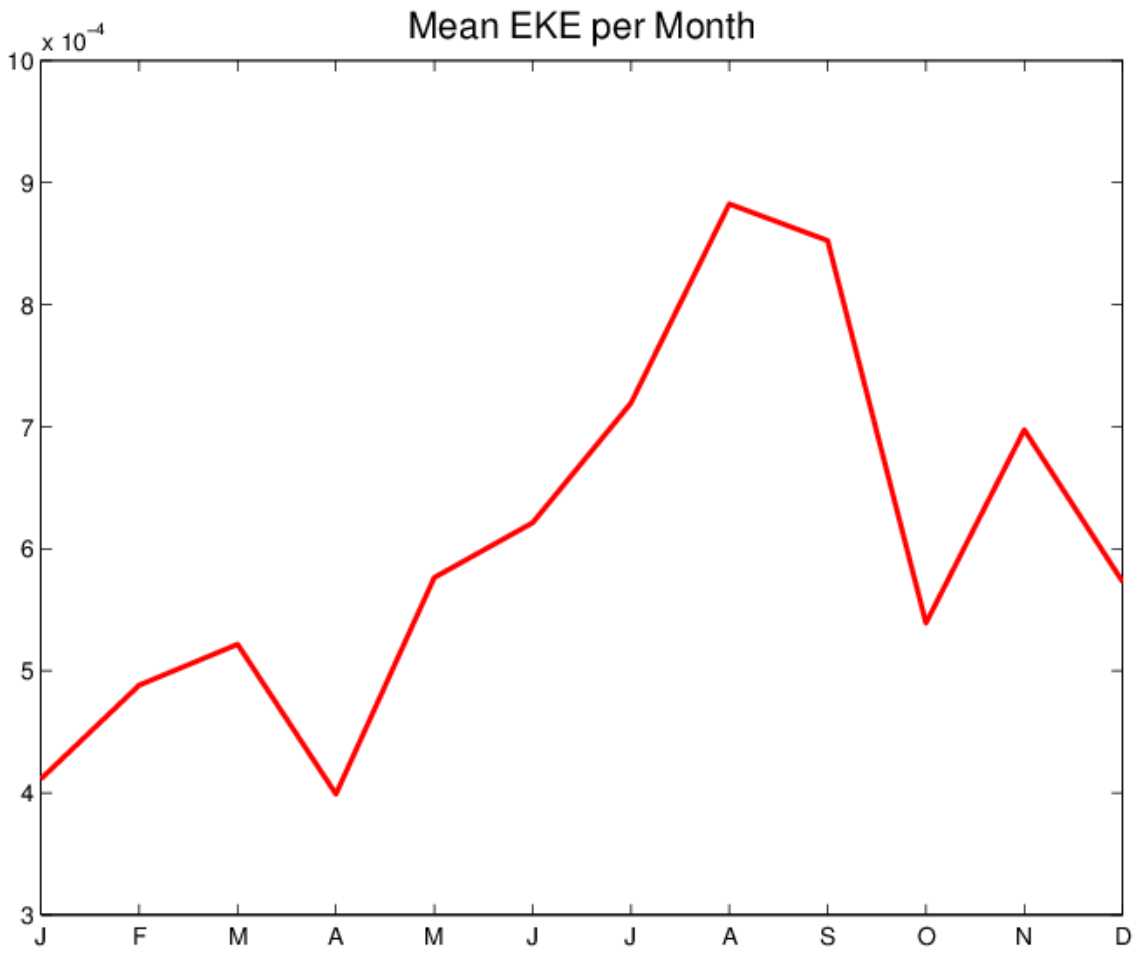

Figure 2.23: Mean monthly EKE from AVISO geostrophic currents in m^2/s^2 in the HLCC region

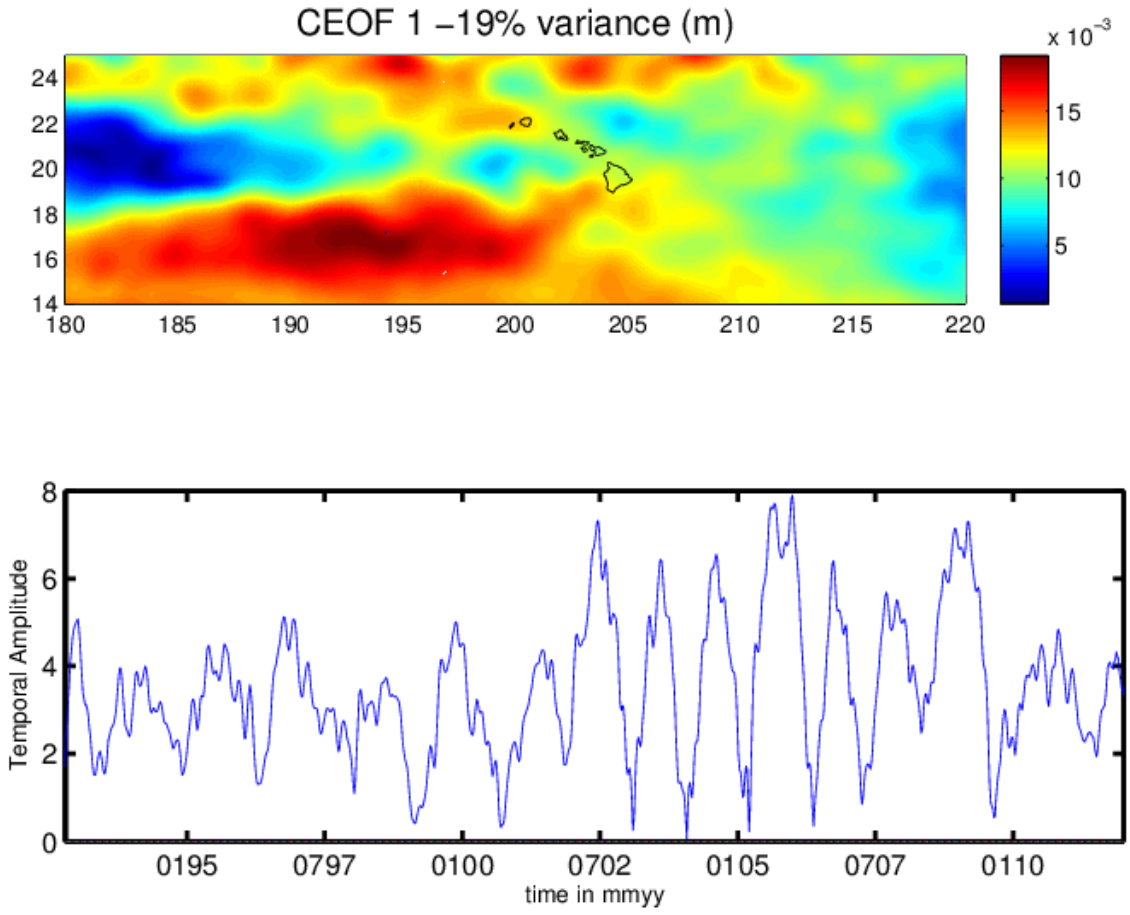

Figure 2.24: Complex EOF Mode 1 from SLA data. This mode is a match to the sum of EOF modes 1,2 and 3 from SLA.

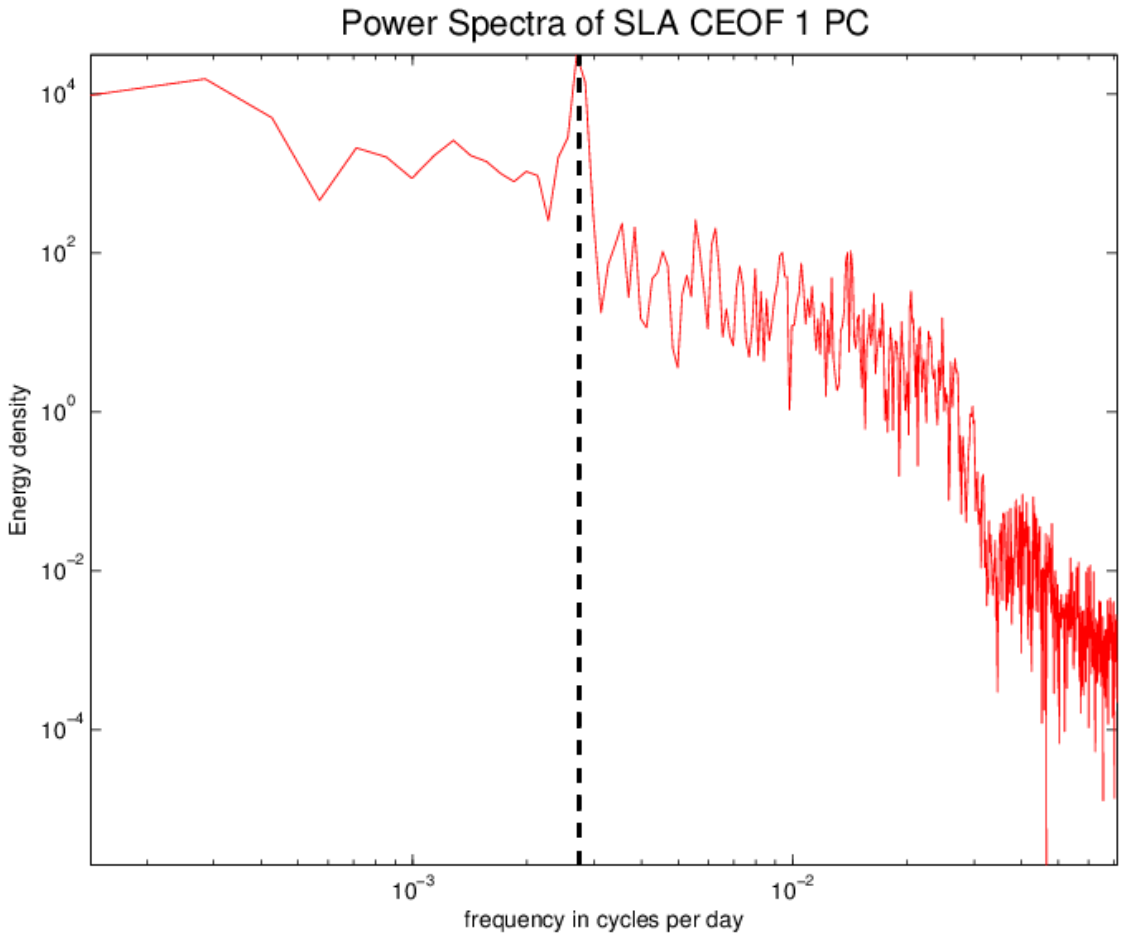

Figure 2.25: Spectrum of sea surface height CEOF mode 1. The dashed line represents a period of one year.

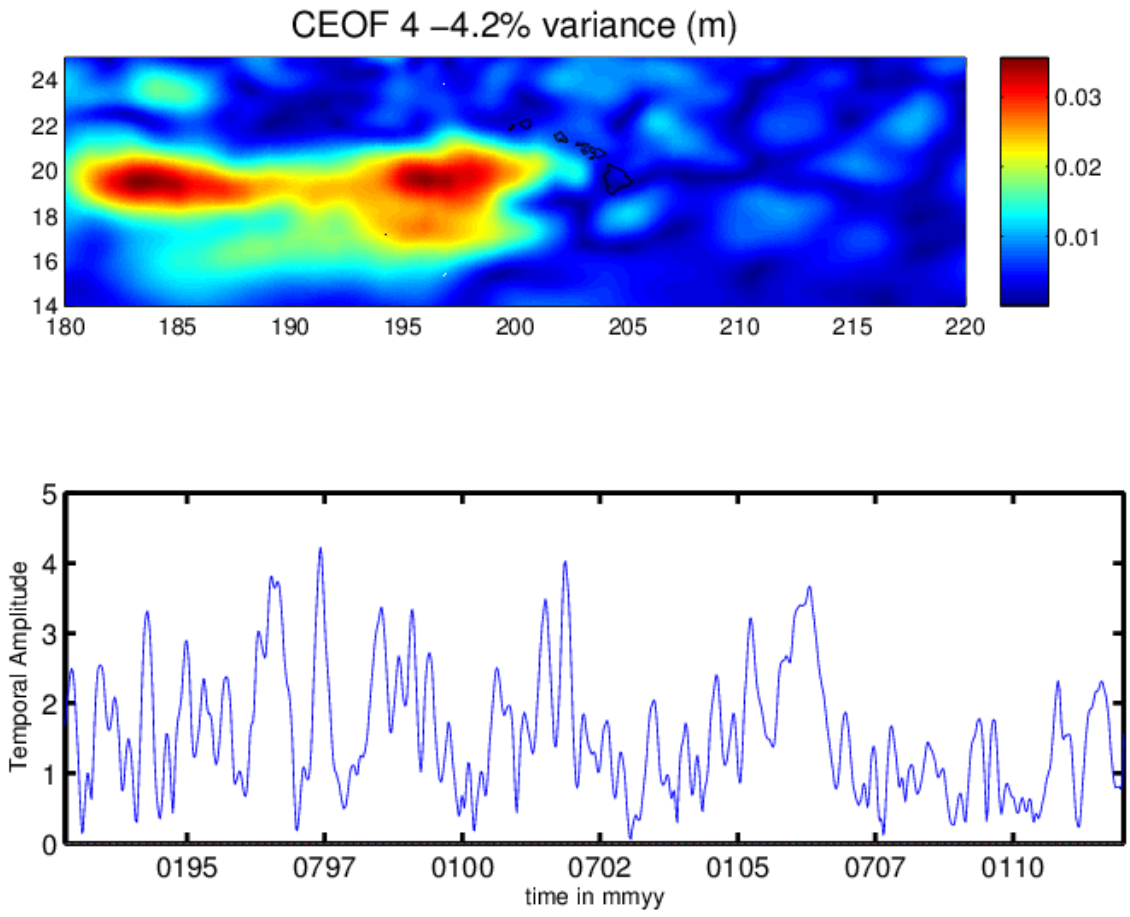

Figure 2.26: Complex EOF Mode 4 from SLA data. This mode is a match to EOF mode 6 and 7 from SLA.

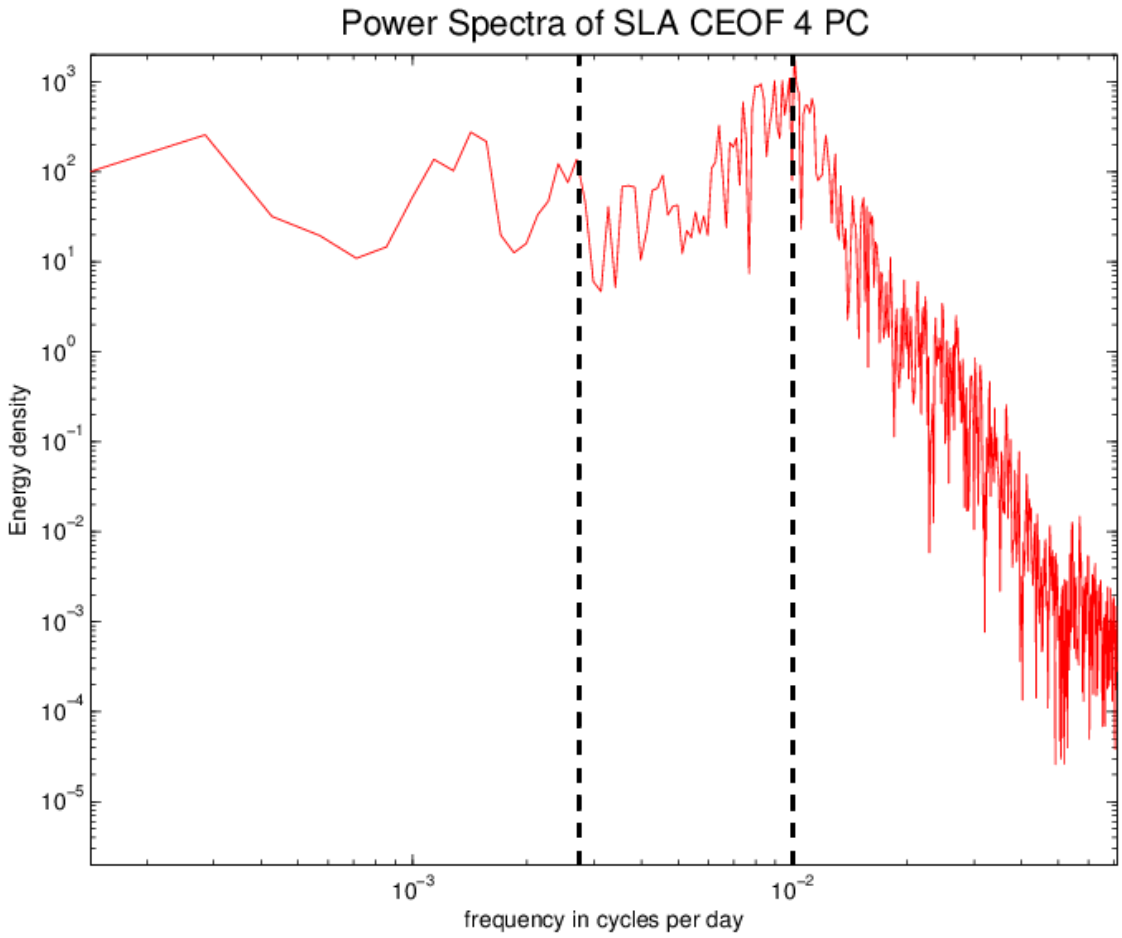

Figure 2.27: Spectrum of sea surface height CEOF mode 4. The two dashed lines represent periods of one year, and 100 days.

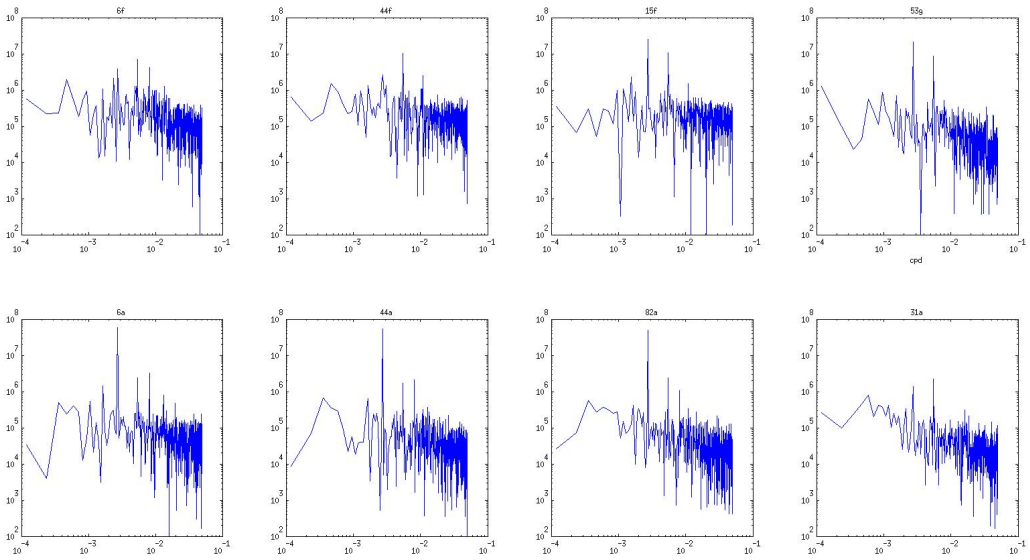

Figure 2.28: Fourier analysis of 8 different along-track SLA time-series. The order of the plots matches geographic position. The left two spectra are from positions east of the islands, the right six are downstream of the islands. The top row are positions at 19 °N, the bottom row are 17 °N.

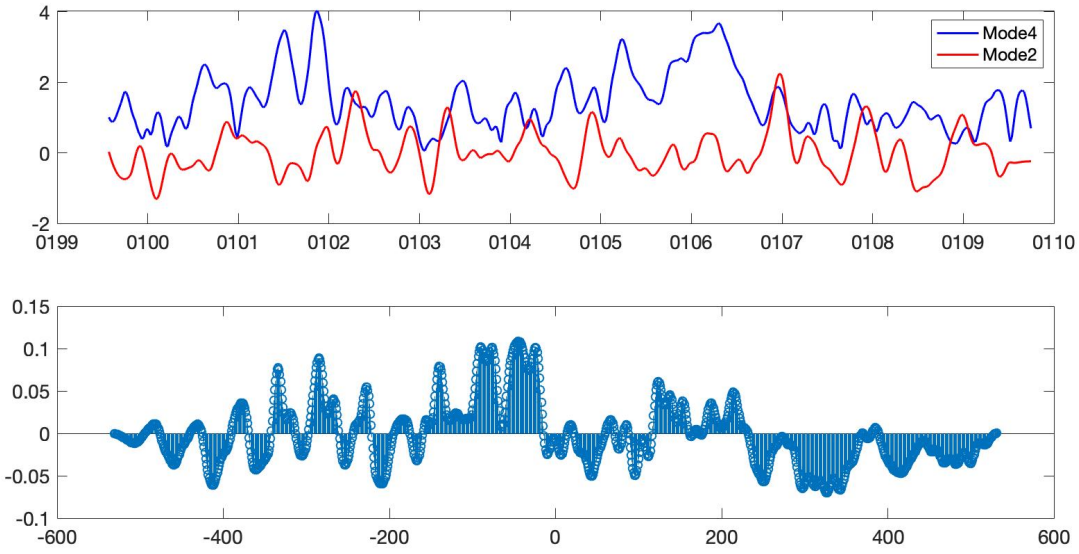

Figure 2.29: Top: Plot of temporal amplitudes of sea level anomaly mode 4 (blue) and wind stress mode 2(red). Bottom: positive and negative time lag coefficients for each time series.

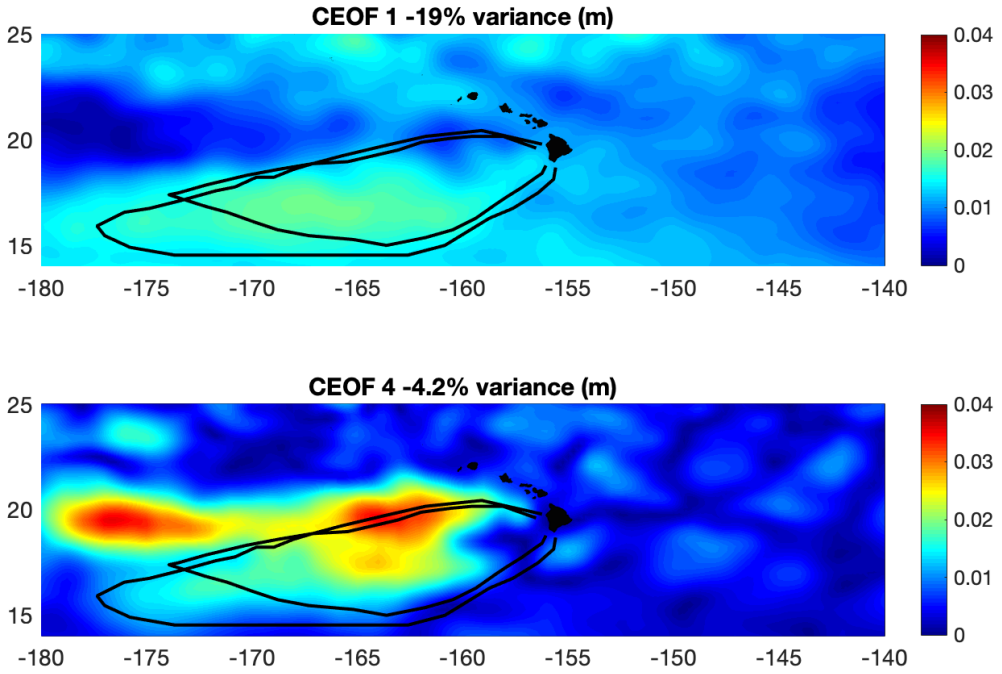

Figure 2.30: Top: Complex EOF mode 1 from SLA data. Overlaid in black is the outline of the anticyclonic zone created by the 25 years of drifter data. Bottom: Same as top, but for SLA CEOF mode 4.

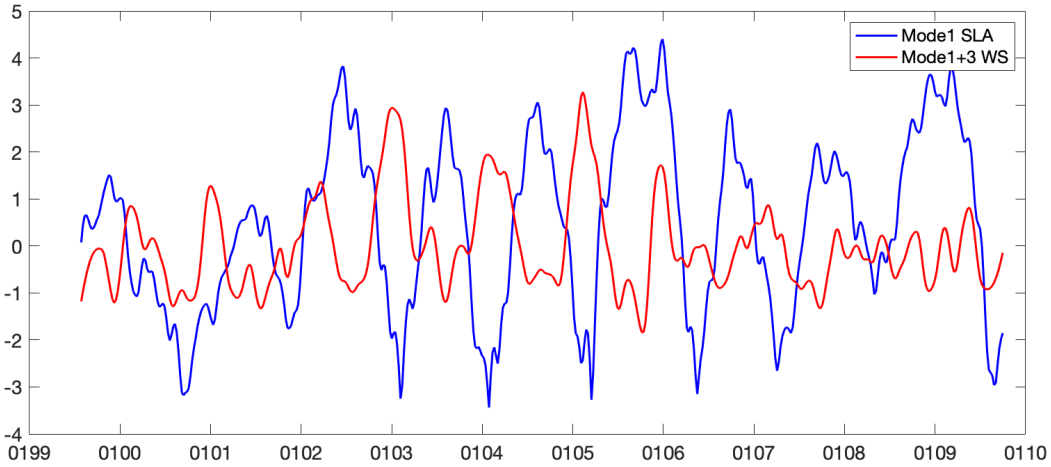

Figure 2.31: Plot of temporal amplitudes of sea level anomaly mode 1 (blue) and combined wind stress modes 1 and 3(red)

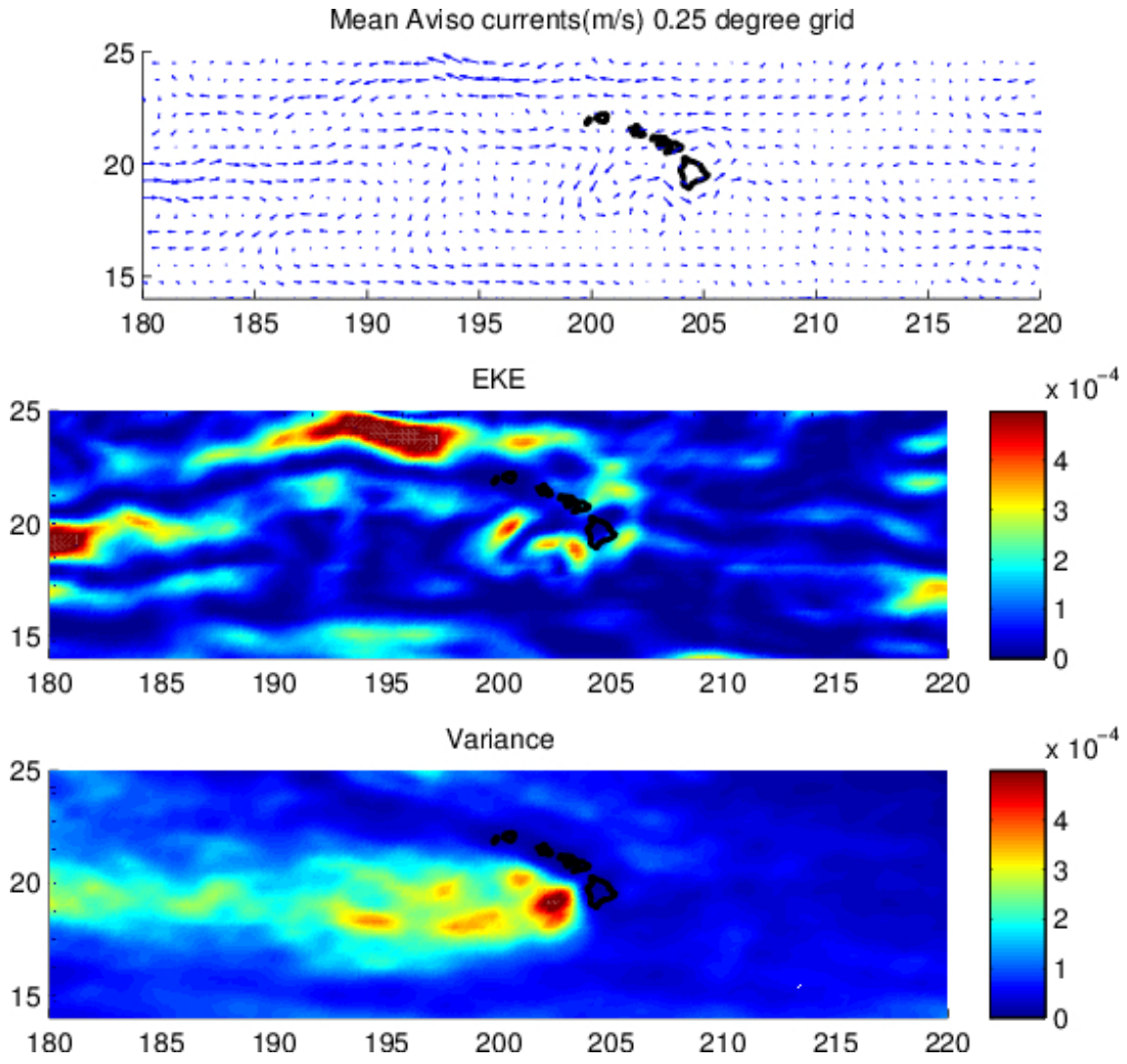

Figure 2.32: Top: Mean AVISO geostrophic currents from 1992-1012. Middle: EKE for mean AVISO geostrophic currents (m^2/s^2, 1/4 degree resolution) from 1992-2012. Bottom: AVISO geostrophic currents variance (m^2/s^2, 1/3 degree resolution) from 1992-2012.

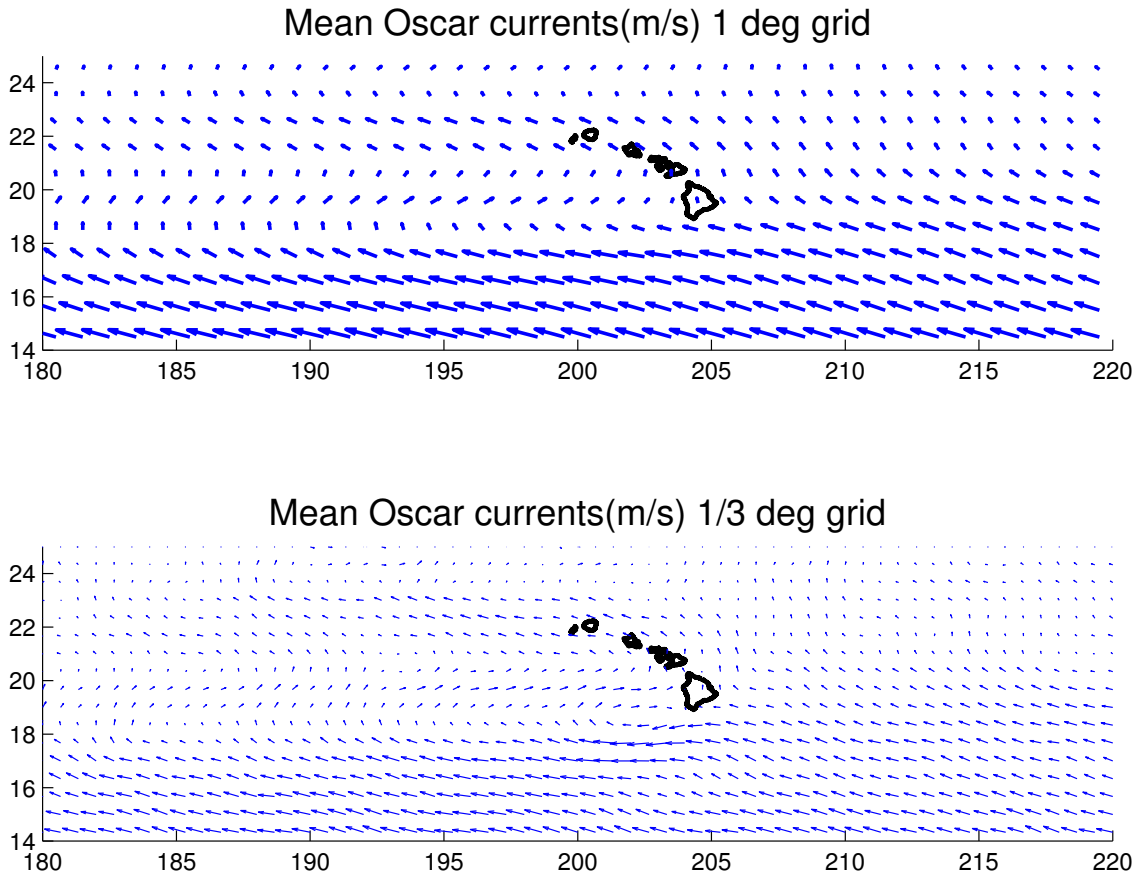

Figure 2.33: Top: Mean OSCAR currents (m/s, 1 degree resolution) from 1992-2016. Bottom: Mean OSCAR currents at 1/3 degree resolution, every other vector plotted.

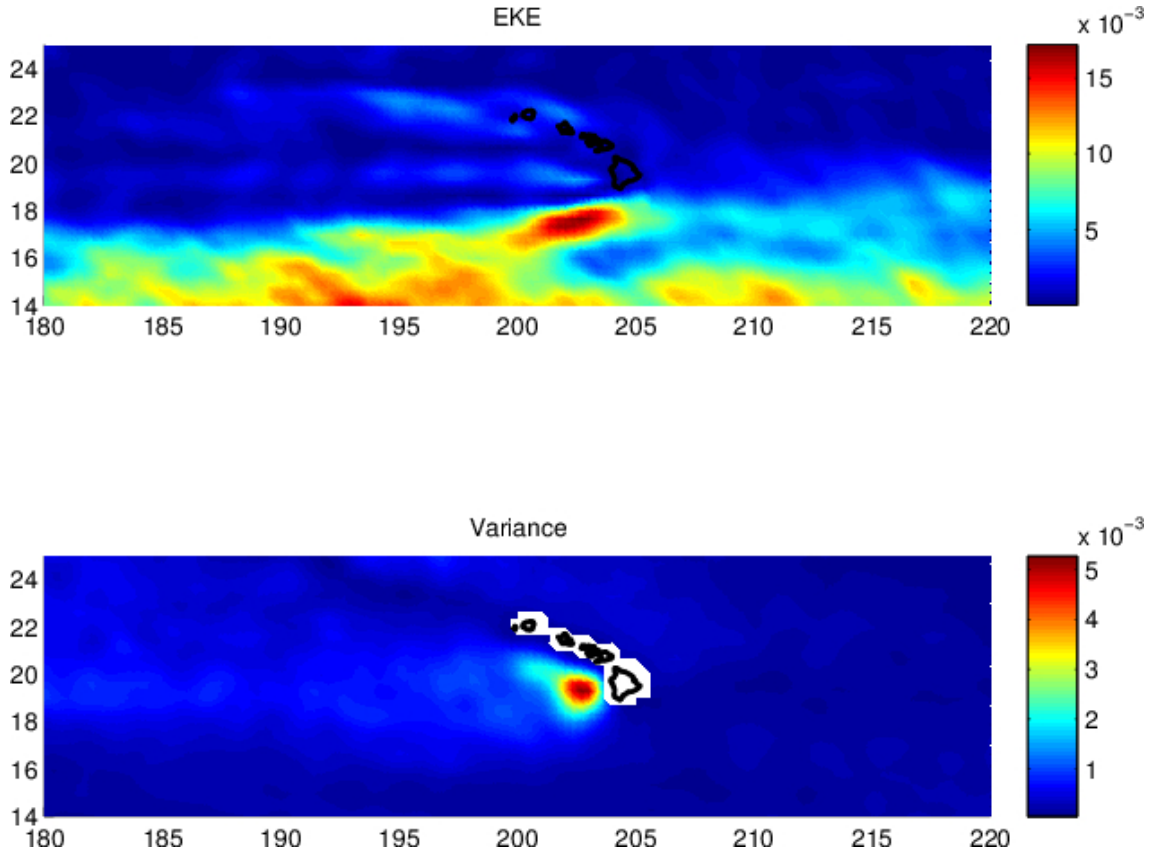

Figure 2.34: Top: EKE for mean OSCAR currents (m^2/s^2, 1/3 degree resolution) from 1992-2016. Bottom: OSCAR currents variance (m^2/s^2, 1/3 degree resolution) from 1992-2016.

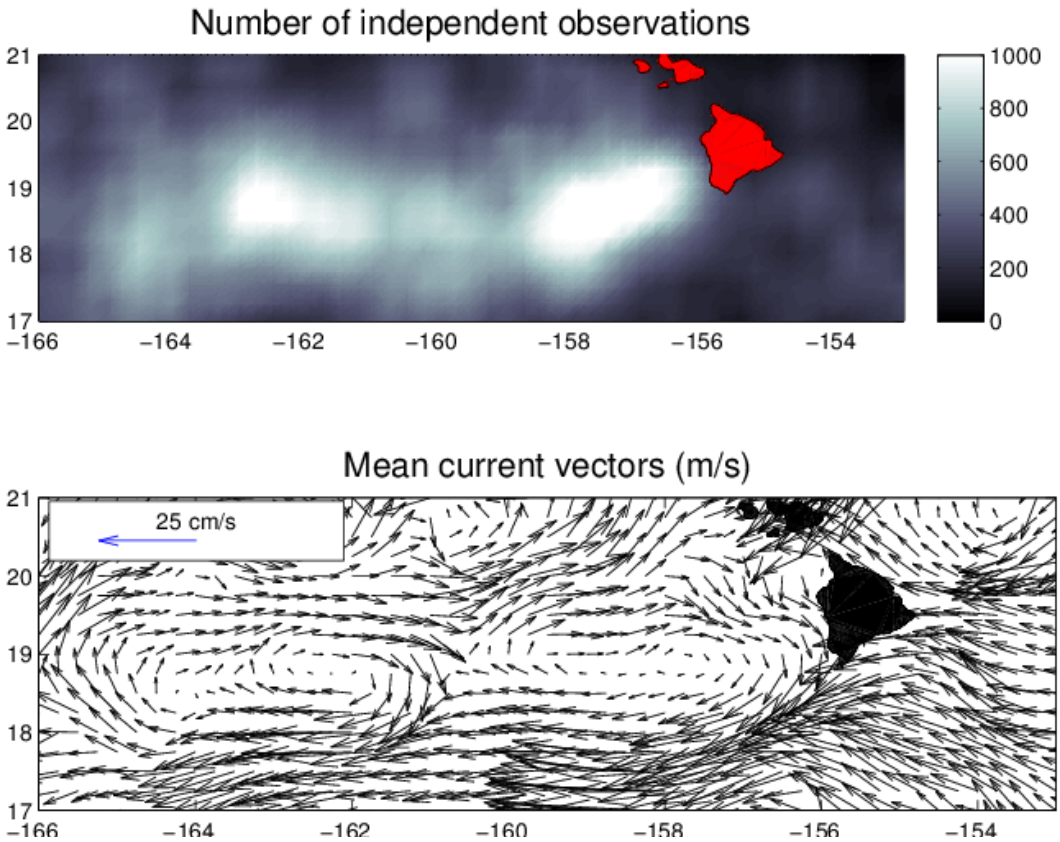

Figure 2.35: Top: Number of independent observations calculated using only anticyclonic looping drifting buoy tracks. Bottom: Mean currents calculated from only anticyclonic looping drifting buoys.

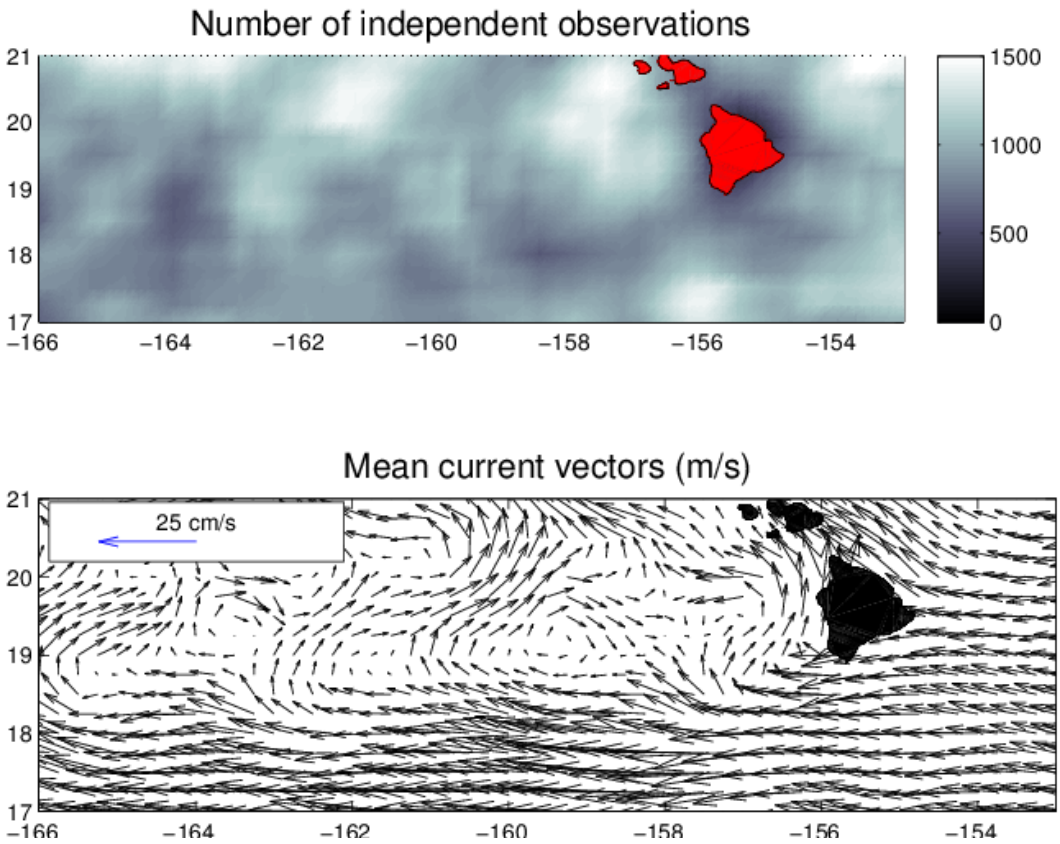

Figure 2.36: Top: Number of independent observations calculated using only non-looping drifting buoy tracks. Bottom: Mean currents calculated from non-looping drifting buoys.

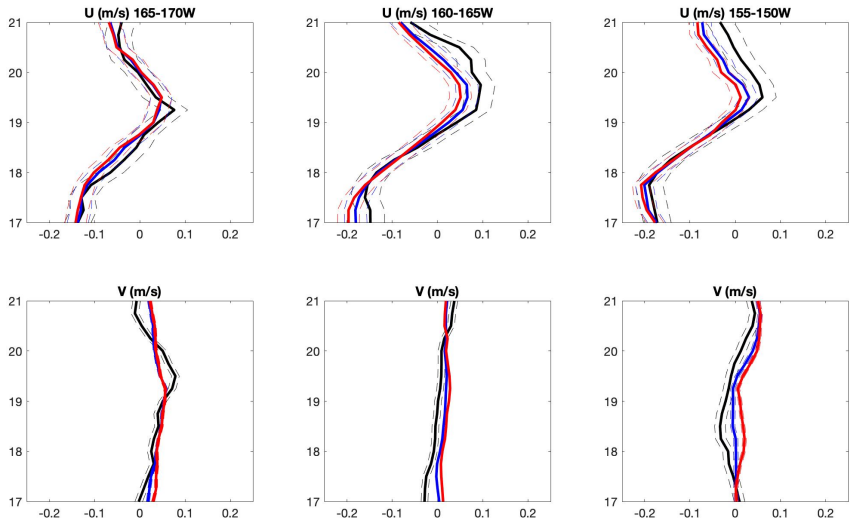

Figure 2.37: Top Row: Zonally averaged zonal (U) currents in m/s in the longitude band 170-165°W, left,165-160°W,middle, and 160-155°W, right. The solid blue line is the zonally averaged current from all 832 drifting buoys. The solid black line is the zonally averaged current from only anticyclonic looping drifting buoys. The solid red line is the zonally averaged current from all drifting buoys except anticyclonic loopers. The correspondingly colored dashed lines are the 95% confidence intervals. Bottom row: same as top row, but for zonally averaged meridional (V) currents in m/s

Chapter 3

Drifter Statistics in West Oahu Coastal Waters: Observations of Island Lee Dynamics

Abstract

Ocean island lees have been well studied in many regions, including the Hawaiian Islands and Canary Islands. However, in the Hawaiian Islands, most of the research has been on the lee created by the largest island, the island of Hawai'i. The smaller islands have lee regions that can be hard to detect with satellite data due to low spatial resolutions. Here, using drifter data and high frequency radar, a year long observational study was conducted in order to investigate the island lee created by Oahu, a smaller, but regionally important island. A distinct cyclonic zone was observed off the northwestern corner of Oahu, with a distinct anticyclonic zone observed off the southwestern corner of Oahu, matching theoretical predictions from wind-stress curl dipoles in the island's lee. The zones could be observed in both the HFR currents and the mean currents derived from the drifting buoys. Vorticity balance analysis indicates that vortices, both cyclonic and anticyclonic, that formed during normal northeast trade wind conditions are primarily wind-induced. However, cyclonic vortices formed in Oahu's western waters even when the trade winds reversed, indicating these vortices were not wind-induced, and least one cyclonic vortex formed during both Kona wind events during the study period.

3.1 Introduction

The center of the island of Oahu is at approximately $21.5°N, 158°W$, in the southern portion of the Pacific subtropical gyre in the path of the NEC. The island is characterized by narrow continental shelves and steep slopes on the western and southern sides, with wider shelves and shallower slopes to the north. South of Oahu there is an 800m-deep channel, the Kaiwi channel, that separates Oahu from the long shallow shelf (Penguin Bank) extending from the island of Molokaʻi. The large-scale flow pattern established by the dominant geostrophic currents includes the Northern Hawaiian Ridge Current that flows along the windward side of the island chain and a weaker northerly current along the leeward side of the island chain (Hawaii Lee Current), both caused by the NEC as it bifurcates at the island chain (Lumpkin 1998). The predominantly westward flow south of the island indicates that some of the westward NEC passes through the Kaiwi channel (Castillo-Trujillo et al. 2019), but this channel separating Molokaʻi and Oahu is notoriously fickle and is regarded as extremely dangerous.

The development of cyclonic and anticyclonic vortices are common in the Hawaiian Island region (Lumpkin 1998; Calil et al. 2008). In particular, as discussed in Chapter 2 the southern tip of the island of Hawaiʻi can create anticyclones through wind stress curl caused by the island's topography, as well as shear instability in the North Equatorial Current (NEC) as it separates from the southern tip of the island (Flament et al. 2001; Jia et al. 2011). Vortices of both rotations have also been previously observed in other locations in the Hawaiian Island chain's lee, such as wind stress curl driven cyclones downstream of the northwestern corner of the island of Hawaiʻi (Lumpkin 1998) and anticyclones in the southwestern waters of Oahu (Chavanne et al. 2010b). However, unlike the vortices that form downstream of the island of Hawaiʻi, there are fewer direct observations of these smaller lee eddies downstream of Oahu, and therefore less is known about the timing, frequency, and cause of these submesoscale features. Previous observations of vortices in the lee of Oahu were observed off the island's western side. In particular, an anticyclone was observed by

Chavanne et al. (2010b) which was similar in diameter to the size of the island, and had a maximum central vorticity close to -f, indicating it was limited by centrifugal instability.

The initial orbital periods of the vortices were $\sim$ one pendulum day at this latitude; therefore the initial Rossby numbers (ratio of local to planetary vorticity f) were nearly exactly -1. These observations were interpreted as a case of centrifugally-limited half-inertial flow (Chew and Busnell 1990). The strongest relative vorticity for a stable vortex is $-f$, i.e. the minimum Rossby number is -1. This limit corresponds to an angular frequency $\omega = -f/2$. Vortices with Ro < -1 are destroyed by centrifugal instability and re-form at a Ro in the stable range (Rayleigh 1916; Kloosterziel and van Heijst 1991; Bidokhti and Tritton 1992; Carnevale et al. 1997). Such half-inertial vortices have also been observed at lower latitudes (Flament et al. 1996; Kennan and Flament 2000; Menkes et al. 2012) and in the arctic (D'asaro 1988).

Negative (positive) wind stress curl associated with the wind shear lines in the lee of the islands (Chavanne et al. 2002, 2010a) can also generate anticyclonic (cyclonic) vorticity in the ocean: the Ekman transport converges towards (diverges away from) the shear line, resulting in downwelling (upwelling) (Barton 2001) and could be leading to the development of the vortices seen off Western Oahu. Cyclonic eddies spun up by cyclonic wind-stress curl and positive Ekman divergence result in upwelling. They share many biophysical properties with coastal upwelling systems, including increased primary production, and have therefore been the subject of many interdisciplinary studies (Calil et al. 2008; Aristegui et al. 1997). They are not limited by centrifugal instability, and can therefore have cyclonic vorticity exceeding f without being unstable. On the contrary, negative Ekman divergence due to anticyclonic wind-stress curl does not have significant biological signature other than horizontal advection, and have not been studied much. The Western waters off Oahu are popular for fishing and the productivity in the region could be impacted by the recurrence of submesoscale vortices formed in the island's lee.

Here we attempt to use observational data from surface drifters and high frequency radar to investigate the flow characteristics in the lee of Oahu. In addition we quantify the frequency and timing of the vortices' appearances off Oahu, as well as their significance to the area's biological productivity.

3.2 Data

In order to investigate the flow properties in the lee of Oahu, a year-long observational study utilizing High Frequency Doppler Radars (HFR) was completed on the western side of the island of Oahu in 2016 (a map detailing HFR coverage is shown in Figure 3.1). During the observational period five HFR were active on Oahu. Total coverage of the southern and western coastal Oahu waters was available 337 out of 366 days during the study, however there were no days without at least partial coverage. Figure 3.2 displays the temporal coverage of each of the five HFR during 2016. HFR radial currents were combined from overlapping HFR units to create vector currents at a $2km$ resolution which were then averaged hourly. The HFR vector currents from all five instruments provided full coverage of the southern and western coastal waters off Oahu, from near-shore out to 100 km. For the year-long observational period, hourly currents were averaged daily to produce a 24-hour mean map of surface vector currents in the coverage area, reducing high-frequency noise in the signals. Cohesive vortices were identified using criteria similar to those set by Chavanne et al. (2010b) where the center of the vortex was defined as the location within the rotating feature that reached a minimum velocity, the maximum velocity of the vortex determined by averaging the azimuthal velocities from the center outwards, and the radius being the distance from the center of the vortex to the maximum velocity. In addition, the vortex needed to be present in the HFR data for two consecutive days where at least 2/3 of the vortex was visible in the HFR vector currents.

In addition to the HFR, 75 surface drifters were used during the observational period with data collection beginning in September, 2015. There were two variations of surface

drifters deployed during this study. Of the 75 drifters, 66 of them were Coastal Ocean Dynamics Experiment (CODE) type drifters that measure flow in the top meter. The CODE drifters were equipped with Argos GPS transmitter and recorded position and sea surface temperature every 30 minutes. The average lifespan of the CODE drifters was 45 days. The last nine surface drifters were a Microstar surface drifter with a diamond shaped drogue centered at 1-m depth (but extending to 1.3m) that had lifespans up to six months. The Microstar drifters were programmed to record and transmit via Iridium their geographic position every thirty minutes.

Drifter deployments were conducted in two nearby locations in the lee of Oahu. Seven repeated deployments of 2-4 CODE drifters occurred around 5nm offshore of Barber's Point, Oahu (shown in Figure 3.1 by the yellow circle) at Station Kahe. Six of these deployments were conducted via the Hawaii Ocean Time Series (HOT) cruises, while one of the deployments was conducted by a vessel of opportunity. An eighth deployment of 4 CODE drifters was conducted 4nm offshore of Honolulu Harbor approximately 18nm to the ESE of Station Kahe by a second vessel of opportunity. This location was used due to inaccessibility of Station Kahe due to heavy seas. The deployments ran from September 2015 until May 2016. In addition to the small deployments at Station Kahe, one gridded cluster deployment consisting of 9 Microstars was conducted on May 17, 2016 in position $21°13.9'N, 158°14.4'W$ (shown in Figure 3.1 by the green circle). The location of the cluster deployment was chosen based off of a center of anticyclonic vorticity detected in the HFR. The drifters used in the cluster were placed in a gridded pattern with 2km spacing. However, initial positions were offset based on the on-scene currents, resulting in a grid pattern at the time the last drifter was placed in the water (cluster deployment lasted 1.2 hours). Nine CODE drifters were deployed at each cluster grid point approximately 200m offset from their Microstar pair. However, due to small differences in their responses to the surface forcing and the successful activation of only seven of the nine, only the Microstar were used to look at flow features from the cluster deployment and those CODE drifters were removed from

the data set (leaving the 66 used here). However, since all of the Station Kahe deployments were the same drifter type (CODE) their use is acceptable for this analysis as there is no conflict in performance. A full description of the differences in the drifter's behavior is provided in Chapter 4. In addition to the Station Kahe deployments, CODE drifters deployed in support of operational oceanographic activities such as search and rescue were also included if they passed through the region outlined in Figure 3.1. This brought the total to 75 CODE style drifters and 84 in total between both types.

For each drifter, the geographical position and sea surface temperature recorded every 30 minutes were extrapolated from the data sets. Missing or bad position data were linearly interpolated for the bottom and top of each hour throughout data gaps. Repeat exact geographical positions that resulted in a speed of zero were ignored and linearly interpolated as if the position was missing. From the clean data, vortices were isolated in the surface drifter data when a single drifter made at least two complete loops in a vortex, or when a drifter completed only one loop it was used if other drifters existed in the same vortex at the same time and multiple loops could be established. Vortex center, radius and velocity were calculated from the drifter data after the mean translational speed was removed.

3.3 Flow statistics using drifters

From the 84 drifters, there are just over 2000 drifter days coverage in the lee region. Between all three sources of surface drifters, there are sufficient observations to be able to investigate flow dynamics in the near lee of Oahu. Outside of the Oahu region, the statistics become less robust due to smaller number of observations. The number of independent observations for each 0.25° grid is shown in Figure 3.3. The highest concentration of observations is in the direct lee of Oahu's western shore where both the Station Kahe and cluster deployments were conducted. This area of high drifter observations coincides with coverage of the western Oahu HFR. Although the drifters traveled well outside the

direct lee of Oahu, the number of observations diminishes rapidly away from the deployment locations as they disperse in space and time.

The initial behavior, represented by the first 48 hours after launch, of the Station Kahe deployments is shown in Figure 3.4. The deployments depicted are shown in order of first to last deployments. The first launch occurred in September, 2015 (Figure 3.4a, top-left) and the last launch was in May, 2016 (Figure 3.4h, bottom-center). The drop position of the first drifter launched in the group is represented by a black x. For reference, the one launch that occurred away from Station Kahe was the sixth deployment, shown in Figure 3.4f and will be referenced from this point forward as Station Aux. All others occurred near Station Kahe. The second launch at Station Kahe was completed in two parts, two of the four CODE drifters were deployed on the beginning of the cruise and two CODE drifters were deployed on the return to port, explaining the apparent divergence of the drifters.

Of the eight launches, there were four occurrences of the drifters heading northwest towards the island of Kauai. This movement would appear to follow the Hawaii Lee Current, but it is only apparent in half of the deployments. During the other half of the deployments, the Hawaii Lee Current was absent and the drifters moved in dissimilar directions. When the Hawaii Lee Current was absent, the drifters covered less distance and remained closer to the drop site for a longer period of time, resulting in a slower dispersion.

The results of the cluster deployment are shown in Figure 3.5 and their dispersion over the first 21 days is shown in Figure 3.6. Even as the cluster deformed, the drifters remained in their relative positions for the first two days. A detailed discussion of the initial drift is provided in Chapter 4. During the first three weeks, the drifters separation increased exponentially when three of the drifters became trapped in the anticyclone. The rest of the cluster continued to the west. Thus the primary feature driving the cluster's movement was the presence of a large anticyclone off the southwest corner of Oahu. The anticyclone persisted in the vicinity for 16 days, keeping the drifters in the HFR coverage region longer

than when anticyclones were not present. The development and characteristics of the anticyclone are discussed in detail in section 3.4, below.

Another interesting feature observable in the cluster deployment is the eastward movement of four drifters near latitude band 19.5°N. This latitude band coincides with the center of the Hawaiian Lee Countercurrent (HLCC). The HLCC is an eastward current with mean speeds $\sim 10\, cm/s$ that is centered at 19.5°N (Flament et al. 1998). It was shown by Chavanne et al. (2002) that the HLCC can be forced by Sverdrup transport induced by wind stress anomalies in the lee of the islands. Lumpkin and Flament (2013) followed this by examining the role of lee vortices in maintaining the HLCC. They found that the anticyclonic vortices to the south of the HLCC played a key role by providing eddy to mean barotropic kinetic energy conversion in the HLCC. Lumpkin and Flament (2013) also found that the HLCC strength was weakest in April/May and peaked in August-January. The cluster was deployed in May 2016, but the drifters entering the HLCC did not reach that point until late June, as the HLCC was building. The drifters had a mean speed of $11\, cm/s$ during their eastward zonal movement through the HLCC.

Spaghetti diagrams of all the 84 drifter's trajectories in the vicinity of Oahu show some key features of island's lee dynamics. Figure 3.7 shows all the drifter trajectories, broken down into 1-day segments, and color coded by mean direction. The large amount of purple color off the western coast of Oahu and some near the western coast of the island of Hawai‘i follow the Hawaii Lee Current. There is very little purple, or northwestward movement between the island of Hawai‘i and Oahu. Most of the drifters that passed through this region were actually moving to the southeast. However, the flow to the northwest is strong between the islands of Oahu and Kauai. The drifters follow the Hawaii Lee Current past Oahu with most joining the Northern Hawaiian Ridge Current on the windward side of Kauai. Other persistent features are the presence of anticyclones off the southwest corner of Oahu and cyclones off the Kona coast, on the island of Hawai‘i. These recurring vortices block the dominant geostrophic flow. To see the background flow not under the influence

of these vortices, any drifter that was trapped in vortices in these regions were removed (13 drifters in total). The trajectories of the non-rotating drifters are now shown in Figure 3.8. With the rotating drifters removed, the presence of the Hawaii Lee Current, the Northern Hawaiian Ridge Current, their intersection and then later bifurcation around Kauai are exaggerated.

Mean currents were calculated from the drifter trajectories in the vicinity of Oahu. The calculations were confined to the region near Oahu with the greatest number of observations. Mean currents were calculated for a region outlined by 21°N to 22°N and 159°W to 157.5°W. The box was broken down into a 0.05° grid with 0.1° smoothing. The mean zonal and meridional currents and their variance was calculated for each box in the grid if it contained at least two full days of drifter data. All boxes with less than two drifter's days observations were discarded. The drifter derived mean currents show weak and variable flow on the south shore and west shores of Oahu (Figure 3.9). Strong northwestward flow is apparent in the Kaʻieʻiewaho channel separating Oahu and Kauai. The drifters' mean flow through the Kaiwi channel separating Oahu and Maui is predominantly eastward. This disagrees with previous observations where the mean flow through the channel parallels the island chain and is thought to be caused by the Northern Hawaiian Ridge Current bifurcating around the island (Burks 1967; Lumpkin 1998; Costa et al. 2016). The drifters that did pass through the Kaiwi channel tended to stay close to shore and the flow could be tidally driven. However, no drifters passed through the Kaiwi in the westward direction. Also of note is the counter-rotating flow patterns seen between 159°W and 158.5°W. In that longitudinal band, the southern region between 21°N and 21.4°N is rotating anticyclonically, whereas the flow in the northern region from 21.4°N to 21.8°N is cyclonic.

The mean currents from the drifters come from 9 months of drifter tracks, from September-May. For comparison, Figure 3.10 shows the monthly mean currents calculated from the Oahu HFR. The vectors are uniform in length, but color coded by velocity. The fastest currents occur off the western coast of Oahu with generally weaker currents off the

south shore of the island. Temporally, the strongest currents occur in March and May with monthly mean currents at 16 and 20 cm/s, respectively. The weakest currents occur in January, with a monthly mean of just 9 cm/s. Unlike the drifter-derived mean currents, the counter-rotating flow pattern is not immediately apparent in the HFR mean currents. However, anticyclonic rotation is visible in the monthly mean currents off Barber's Point in January and November. Cyclonic rotation is visible off Kaena in March and September. With the monthly means, both types of vortices are not visible in the data at the same time. To visualize the lee vortices, the HFR data is broken down into daily means where more frequent vortices become apparent.

3.4 Observations of Lee Eddies

During the study period both anticyclones and cyclones were observed in the region of interest. There were five anticyclones observed in the southern and western coastal waters of Oahu by the HFR (Table 1). All five anticyclones formed below latitude $21.15°N$, approximately level with the south corner of Oahu. Of the five anticyclones, three were fairly weak vortices with central vorticity values near $-0.5f$ that were visible in the HFR data for only 3-5 days, and two were strong (near $-f$ vorticity), persistent (in the area of coverage) anticyclones that were visible in the HFR data for 16 days each. The two stronger anticyclones formed in nearly the same location, around $21.1°N, 158.35°W$ and both propagated slowly westward at $4 - 4.5cm/s$. The first strong anticyclone appeared at the end of May and the second strong anticyclone became visible in the HFR surface current field on the first of August. Both of these vortices approached the centrifugal instability limit of $Ro = -1$. The weaker anticyclones remained fairly stationary until they were broken down and no longer visible in the surface currents. Oahu anticyclones remained noticeably closer to the island for longer period of times than the anticyclones formed in the lee of the island of Hawai‘i (Chapter 2). Even two anticyclones that had entrained drifters, and

therefore could be monitored after leaving the HFR area, did not extend past 159°W during their observed lifespan.

There were eight cyclones observed in the HFR data during 2016. The majority of the cyclones formed north of the anticyclones, above latitude line $21.4°N$, while three out of the 8 cyclones formed just to the south of the anticyclonic region at a latitude line of $20.9°N$. Unlike the anticyclones, cyclones are not constrained by centrifugal instability and on four occasions sustained core vorticity values in excess of $+f$, with the strongest cyclone achieving $+1.4f$ for two days while in the HFR area. This particular cyclone moved north out of the coverage area after the second day at peak strength, with a mean forward speed of $8cm/s$. This is contradictory to the anticyclones, which stayed relatively near to the island. Unfortunately, no drifters were trapped in any of Oahu's cyclones and their progression outside of the HFR area was not directly observed.

The presence of each type of vortex throughout the HFR time coverage is shown in Figure 3.11 (top). The five anticyclones (blue stars in Figure 3.11) and the eight cyclones (red stars in Figure 3.11) do not overlap, except for a two day period in June, as an anticyclone exited the coverage to the west, and a cyclone formed in the close lee on the same day. Counter-rotating vortices on the north and south side of the island were not observed to occur at the same time. Vortices occurred in every month except October and December, with an average spacing of 19 days, but irregularly with a standard deviation of ± 15.8 days.

The daily mean wind velocity and direction, as measured at the Honolulu airport is shown in Figure 3.11 (middle). The Hawaiian Islands, located between $19-25°N$, lie in the portion of the global wind belt dominated by the Northeast Trade winds. The locations of the wind belts shift with season, bringing the Hawaiian Islands closer to the mid-latitude storm belt during winter as the Intertropical Convergence Zone dips below the equator (Xian and Miller 2008). This can disrupt the Northeast Trade winds, causing them to reverse. This reversal is known as a "Kona" wind in Hawaii (since the winds now come from the west, it

can bring with it volcanic smog from the Kona area, decreasing air quality) (Morrison and Businger 2001). Overall, the winds during the observational study were predominately from the northeast (306/366 days, 84%), however, there were two main Kona events during this time. The first lasted from the beginning of January until February 10th (40 days) and the second lasted from mid-August until the beginning of September (20 days). During a Kona event, the wind is reversed, which would eliminate the wind-shear region normally located on the Western side of Oahu. If the vortices were purely forced by Ekman pumping caused by wind stress curl in the island's lee, no eddies would be found in their typical regions during a Kona event. No anticyclones were observed during Kona wind events, however, three cyclones were observed during the two Kona events. This implies that another forcing mechanism was involved in these three cyclones.

3.4.1 An Anticyclone case study

The presence of multiple drifters in the May 2016 anticyclone, along with coverage from the HFR, make it a good case study to examine the dynamics of Oahu's lee eddies. All drifters caught in the May anticyclone were extracted from the data set. Just from the cluster deployment, there were three Microstars in the anticyclone. Due to their increased lifespans and decreased leeway (refer to chapter 4) the Microstars were used to study the anticyclone. During the drift period of the cluster, the mean translational speed of the buoys remained both zonally and meridionally negative. Removing the mean translational speed of each drifter revealed the residual movement of the drifter due to shorter timescale features such as these submesoscale vortices. Anticyclonic rotation is evident in three of the buoys in both the total and residual currents and was caused by one anticyclonic vortex. Two drifters completed one loop and one drifter completed three loops inside the anticyclone. The beginning of the first anticyclonic loop was observed in the drifters motion on May 24, 2016 at 0530Z and was last observed on June 6, 2016 at 0330Z, giving a duration of just under 14 days. Vortex characteristics estimated from the drifting buoys yielded a mean period of 3.7 days and a mean radius of 20km (Figure 3.12). The anticyclone was also

visible in the HFR data during May and into June. In contrast to the drifter data, a fully formed anticyclone was not evident until May 25th, with anticyclonic rotation beginning to develop two days later on May 23rd, 2016. The anticyclone was visible in the HFR data for 16 days, until June 8th. The anticyclone formed with its center near $20.9°N, 158.3°W$. Over the course of the 16 days it was visible in the HFR data, it drifted slowly west with a mean speed of 4.5 cm/s until its center fully exited the HFR coverage by June 9th, 2016. The daily mean HFR surface currents and their associated vorticity for May 28, 2016 is shown in Figure 3.12, along with the trajectory of the longest looping drifter. The maximum daily mean anticyclonic vorticity achieved in the core of the vortex during its lifespan was $-0.8f$, calculated from the HFR surface currents. For an anticyclone at latitude $20.8°N$ to be at the centrifugal instability limit with a Rossby number of -1, or vorticity of $-f$, the corresponding period is 2.8 days. For the observed anticyclone with its associated strongest mean vorticity of $-0.8f$, the anticipated period is 3.56 days, which corresponds well to the observed period of 3.7 days calculated from drifter data.

There are multiple ways to measure separation rates using HFR data. Here, two were used to examine the characteristics of particle distribution in and around the anticyclone. The first parameter calculated was the Okubo-Weiss parameter (W) which compares the magnitude of strain to vorticity:

$$W = \sigma_n^2 + \sigma_s^2 - \zeta^2 \tag{3.1}$$

where σ_n is the normal component of strain, σ_s is the shear component of strain, and ζ is vorticity, which are derived from the velocity gradient tensor. Another method to investigate separation is the Instantaneous Rate of Separation (IRoS) (Futch 2009). Also derived from the velocity gradient tensor, the IRoS is similar to a Finite Time Lyapunov Exponent (FTLE) but does not require time integration, and is useful in examining mean statistics in a region.

$$IRoS = \sigma_o + Tr(\eta) \tag{3.2}$$

where $\sigma_o = \sqrt{(\sigma_n^2 + \sigma_s^2)}$ is the full shear component of the flow and $Tr(\eta)$ is the divergence. These parameters were calculated for the anticyclonic feature seen in the HFR data starting on May 24, 2016. The Okubo-Weiss parameter is as expected for a vortex, with strong vorticity in the center region and higher strain along the edges. Drifters located in the blue vorticity dominated regions stay inside the vortex until reaching the red outer limits at which point they are ejected quickly (Figure 3.13). The IRoS shows convergence of particles in the center, to be expected from an anticyclone, and strong dispersion along the outer edges, but especially on the eastern edge. This indicates that the anticyclone is trapping particles and heat at its center, and dispersing them on its periphery. Looking at the satellite sea surface temperature for the peak of the anticyclone, on May 27, shows a strong, warm core vortex, with core temperatures in excess of 3°C warmer than surrounding waters. As anticyclonic vortices rotate, they reach geostrophic balance with an inward Coriolis Force and an outward Pressure Gradient Force. This happens due to convergence at the sea surface creating a dome of water, which then leads to downwelling and a deepening of the thermocline. This creates a warm core to the vortex. These warm cores are not only less biologically productive, but can impact air-sea interactions and heat transport between the ocean and the atmosphere. Differences in air-sea temperatures can influence sensible heat transfer as well as latent heat fluxes caused by evaporation of sea water and subsequent condensation in the atmosphere. A recent study in the southern ocean found that mesoscale eddies are responsible for 20% of the variance in surface heat fluxes and that anticyclonic eddies warmed the marine atmosphere (Villas Bôas et al. 2015).

3.4.2 Forcing

Yang (2008) mapped the trade wind wakes created by both Kauai and Oahu, the first direct observations of these islands' wind wakes. One of the main results from their work was the measurement and mapping of the strong shear lines created in the wake of those islands. For Oahu, Yang (2008) measured the shear line at the flanks of the island to be approximately a change in velocity of 10 m/s over an equivalent distance of 2-5km, with a

downstream distance greater than 100km. The latitude bands of these observed shear lines match the latitude bands associated with the cyclonic and anticyclone vortex formation regions in this study (Figure 3.15). The positive wind stress curl created by the trade wind wake on Oahu's northern corner seen by Yang (2008) matches the region of cyclonic eddy formation observed in this study, as expected. The negative wind stress curl region found by Yang (2008) aligns with the southwest corner of the island during day and the center of the southern coast during night. The diurnal variations were caused by development of westerly sea breezes during day hours. Although the diurnal variations are not visible in the daily averaged HFR data, the anticyclonic vortices form in the region covered by these observed shear lines in Oahu's wake.

Vorticity Balance

The surface vorticity ($\zeta = \partial v/\partial x - \partial u/\partial y$) balance, shown below in equation 3.3, can be used to determine if the eddies are primarily wind-driven.

$$\overbrace{\frac{D\zeta}{Dt}}^{a} = \overbrace{\frac{\partial\zeta}{\partial t}}^{b} + \overbrace{(\mathbf{u}\frac{\partial\zeta}{\partial x} + \mathbf{v}\frac{\partial\zeta}{\partial y})}^{c} = -\overbrace{\mathbf{v}\beta}^{d} + \overbrace{(\zeta + f)(\frac{\partial\mathbf{u}}{\partial x} + \frac{\partial\mathbf{v}}{\partial y})}^{e} + \overbrace{(\frac{\partial F^y}{\partial x} - \frac{\partial F^x}{\partial y})}^{f} \tag{3.3}$$

The total derivative of vorticity (term a, also known as the Lagrangian derivative) is comprised of the local rate of change in vorticity (term b) and the advective rate of change of vorticity (term c). These changes in vorticity can be due to Beta changes (term d), vortex stretching (term e) or stress curl from the wind or ocean (term f). Here the change in latitude on the spatial scale of a lee vortex off Oahu is small and term d can be considered negligible. This means changes in vorticity can be explained by vortex stretching and forcing stresses. Following Chavanne et al. (2010b), the wind stress curl induced vorticity can be approximated by:

$$F = \frac{1}{\rho H_E} curl_z \tau \tag{3.4}$$

using $\rho = 1023 kg/m^3$ for a seawater temperature of 25°C and an Ekman depth of 30m. The terms in the vorticity balance were calculated for Anticyclone 2 that formed in May and Cyclone 7 that formed in August (Table 3.1). The total derivative of vorticity and vortex stretching were calculated from the HFR currents at the location of the center of the vortex over time. The difference between the two terms resulted in a residual, which if wind driven, would be similar in magnitude to the approximation of the wind stress curl vorticity, given by equation 3.4. If the terms are not of the same magnitude, then other forcing, such as shear instability in the currents could be at play.

The spatial results of the vorticity balance terms are shown in Figure 3.16. In the core of the anticyclone, the stretching is weakly positive, the total derivative is weakly negative and the residual is positive. The estimation of the impact of wind stress curl on vorticity is also shown in the bottom right. The negative wind stress curl expected from a wind-driven vortex is present. The mean values averaged of the core of the vortex over a seven day period are shown in Figure 3.17. This makes is a bit easier to see the relationship between the terms. The terms are not in balance over the first four days of the anticyclones life, indicating that the wind stress curl induced vorticity is not enough to generate the vortex, however as the vortex moves into its later stages of life, the residual term is small, and therefore the vortex could be sustained by the wind stress curl in the lee of the island. The large residual early on in the anticyclones life could indicate that ocean stresses helped spin-up the eddy. Unfortunately the early days of the anticyclone's development May 20-22, were missing in the West Oahu radars. The first day of full coverage was the 23rd, when the anticyclone was small, but formed, and therefore its vorticity budget as it was forming is missing. This anticyclone formed during average NE trade winds. During this study, there were three cyclones that formed during Kona wind events. The last cyclone, #7, not only formed in strong Kona winds, but formed in the normally anticyclonic region of the island's lee. Looking at the vorticity balance terms for the cyclone (Figure 3.18), the stretching is strong negative ($\sim -10^{-9}$), the total derivative is weakly positive($\sim 10^{-10}$) ,

and the residual is strong positive ($\sim 10^{-9}$). The wind stress curl vorticity is almost zero ($\sim -10^{-13}$). This cyclone lasted 17 days and experienced Kona winds for the first half of its lifespan. In fact, looking at the wind stress curl induced vorticity in Figure 3.18, the lee side of the island has completely reversed, with the lee-induced wind stress curl dipole located on what is normally the windward side. This means the the cyclone was not wind-induced, but ocean stress induced during the Kona wind event.

3.5 Discussion

One interesting result from this study is the direct observation of the cyclonic, quiet zone, and anticyclonic sectors in the lee of Oahu. These zones have been studied on Island of Hawai‘i, the southernmost and largest island in the chain. Direct observations through surface drifters (Lumpkin 1998) and sea surface height anomalies (Yoshida et al. 2010) reveal the far-reaching impacts of the oceanic island wake created by the $> 4000m$ tall Hawai‘i Island. In addition, several model studies reveal the impact of wind wake forcing on the generation of mesoscale cyclones (anticyclones) on the northern (southern) lee sides of the island (Calil et al. 2008; Jia et al. 2011). However, except for the direct observation via surface drifters, these studies are limited by the spatial resolution of the satellite derived data and/or the model parameters. The models and satellites have high enough resolution to capture the island wake created by Hawai‘i Island, but not all have the resolution necessary yet to capture the smaller scale island wakes created by islands such as Oahu and Kauai. The oceanic wake created by Hawai‘i Island is visible in satellite sea surface anomaly data out to $170°W$ (for reference Hawai‘i Island has a central longitude of $155°W$), a distance of 1600 km (Yoshida et al. 2010). Local measurements of sea surface anomaly data by Mitchum (1995) revealed 90-day oscillations at Wake Island (4000 km from Hawai‘i) that have been attributed to the anticyclones created by Hawai‘i. The wakes created by the smaller, interior islands do not have such reach and are closely confined to the islands' lee sides (Souza et al. 2014). The implementation of HFR on Oahu has enabled visualization of

these smaller lee vortices created by the island, that otherwise would have been washed out in coarser resolution data sets. During the year-long observational period, Oahu's lee was divided into three zones: a cyclonic zone to the north, an anticyclonic zone to the south, and a quiet zone in the middle of the island lee. Figure 3.15 shows the initial positions of the centers of the vortices captured by the HFR along the southern and western coasts of Oahu. The cyclonic zone occurred at the northern edge of the island lee, starting at $21.4°N$, while the anticyclone zone occurred at the southern edge of the island lee, below $21.15°N$. The quiet zone, in between the two, was marked by no vortex formation during 2016. However, this does not mean vortices did not enter the region during the year, but they did not initially form in the quiet zone. The vortices were primarily wind-induced, with the wind-stress curl dipole created by the island inputting vorticity into the lee region. However, for the anticyclone in May, wind stress alone was not enough to explain all of the residual vorticity, indicating ocean shear stresses played a role in the spin-up, but wind stress maintained the vorticity. There were three cyclones that formed in the anticyclonic sector of the lee. Two of these formed during Kona wind events, where the lee side of the island was completely reversed and wind stress curl could not explain their formation. One of the cyclones (cyclone # 4) formed in the anticyclonic sector during normal NE trade winds. However, this cyclone was weak, formed on the western edge of the HFR radar coverage and dissipated after three days.

Distinct cyclonic, quiet, and anticyclonic zones in the direct lee of the island can have implications beyond current direction and magnitude. As discussed earlier in Figure 3.14, the anticyclones can have significant impacts on ocean temperature as they depress the thermocline. The 3°C increase in temperature in the core of the vortex from surrounding water can increase heat flux from the ocean to the atmosphere. These fluxes are used in ocean and atmospheric models. If heat fluxes from eddies are not included, this could lead to errors in the model results. If these anticyclonic and cyclonic sectors are persistent, as they were in 2016, the heat fluxes would also be persistent. Another implication is the change in

biologic productivity associated with persistent vortices. Hawaiian waters are oligotrophic (Figure 3.19) and in general have low productivity offshore due to its position in the Pacific subtropical gyre (Morel et al. 2010). However, the western near-offshore (3-10nm) waters of Oahu are popular fishing grounds due to the proximity of the steep drop off just three miles offshore and the large numbers of sport fish. During an anticyclone event, such as the one in May, the chlorophyll a concentrations are lower than the surrounding waters, shown by the dark blue (almost zero) area off the southwest corner of Oahu (Figure 3.20). This would decrease fisheries over these time periods. This is opposite when a cyclone forms in the cyclonic sector. During a cyclone there is increased cholorphyll a concentrations. For comparison, Figure 3.21 shows the chlorophyll concentration during a cyclone in early May. This cyclone occurred in the same month as the anticylone and therefore negates seasonal influences on chlorophyll concentrations. The chlorophyll is much higher in the cyclonic sector during the vortex, indicating a higher productivity.

3.6 Conclusion

Although Oahu is smaller than the island of Hawai‘i, it still displays a persistent island wake, with a cyclonic zone to the north, a quiet zone in the middle and an anticyclonic zone to the south. The vortices formed in the wake do not travel great distances from the island, instead remaining in the near lee and therefore in the HFR coverage for up to 17 days, making some of the vortices near stationary. During normal NE trade winds, the vortices are primarily wind-induced from the wind stress curl dipole forming in the lee. However, cyclonic vortices do form in the western waters of Oahu during Kona wind events. During Kona events, the leeward side becomes the windward side and the wind-stress curl dipole disappears in the western coastal waters. These cyclones formed during Kona wind events all formed in the normally anticyclonic zone in the southern section of the island lee and without wind-forcing must therefore be caused by ocean stress induced vorticity changes.

Table 3.1: Top – Anticyclone characteristics observed from High Frequency Radar. Bottom – Cyclone characteristics observed from High Frequency Radar.

$Anticyclone$	DOB	$Duration(days)$	$Radius(km)$	$Vorticity$	$Period$
1	29FEB	3	47	$-0.50f$	5.6
2	23MAY	16	20	$-0.80f$	3.5
3	14JUL	4	32	$-0.59f$	4.7
4	01AUG	16	21	$-0.96f$	2.8
5	02NOV	5	21	$-0.44f$	6.2
$Cyclone$	DOB	$Duration(days)$	$Radius(km)$	$Vorticity$	$Period$
1	23JAN	3	27	$0.52f$	5.1
2	06FEB	4	31	$0.80f$	3.4
3	13MAR	14	22	$1.1f$	2.5
4	13APR	4	47	$0.47f$	6
5	09MAY	5	36	$1.3f$	2.1
6	05JUN	8	36	$0.5f$	5
7	18AUG	13	42	$1.4f$	2
8	03SEP	17	37	$1.3f$	2.1

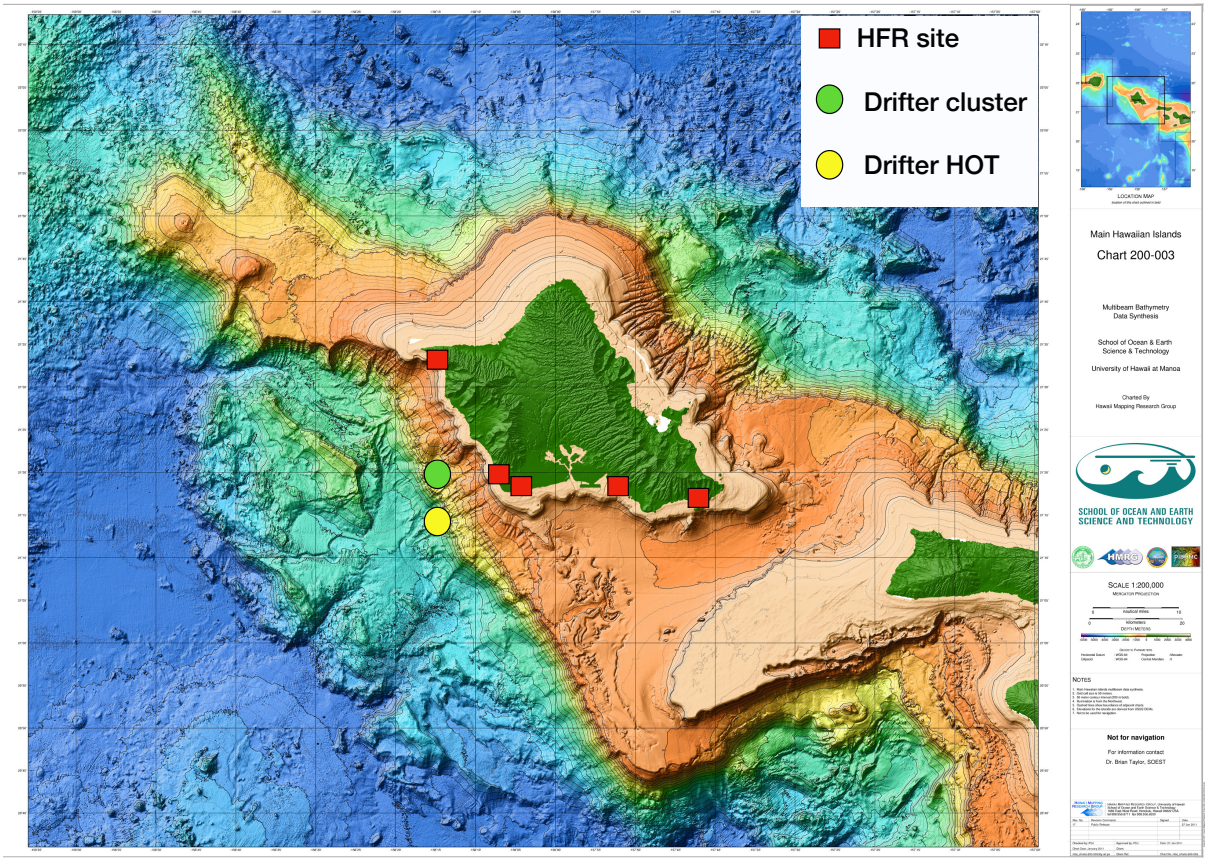

Figure 3.1: Experiment set-up. The red boxes represent the 5 High Frequency Radar sites. The yellow circle marks the location of two surface drifter cluster deployments. The green circle represents the location of the monthly deployments of three drifters via the Hawaii Ocean Time Series (HOT) cruises. Bathymetry from Main Hawaii Islands Multibeam Bathymetry and Backscatter Synthesis.

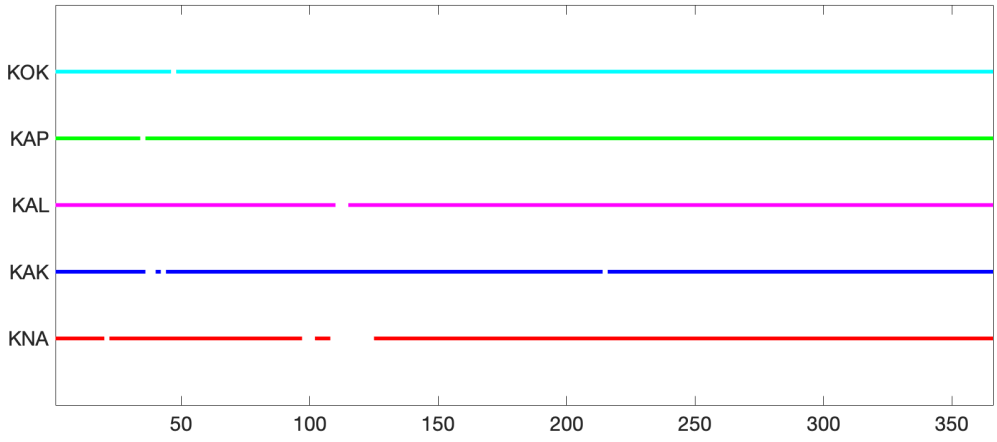

Figure 3.2: Temporal coverage of each radar during 2016. The x-axis is the day of the year. The y-axis is each individual radar. KOK (Koko Head, $21.26°N, 157.7°W$), KAP (Kapolei, $21.31°N, 158.11°W$), KAL (Kalaeloa, $21.29°N, 158.08°W$), KAK (Kaka'ako, $21.29°N, 157.85°W$), KNA (Kaena, $21.56°N, 158.25°W$)

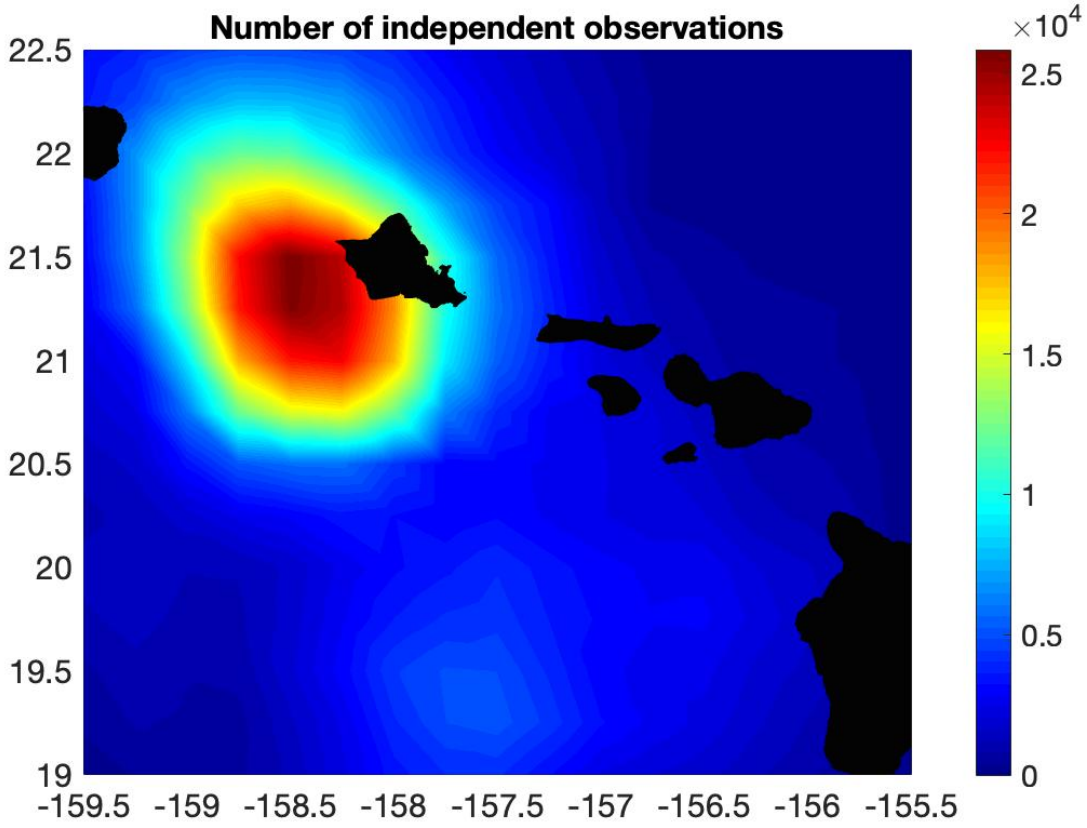

Figure 3.3: Number of observations in each 0.25° grid in Oahu waters.

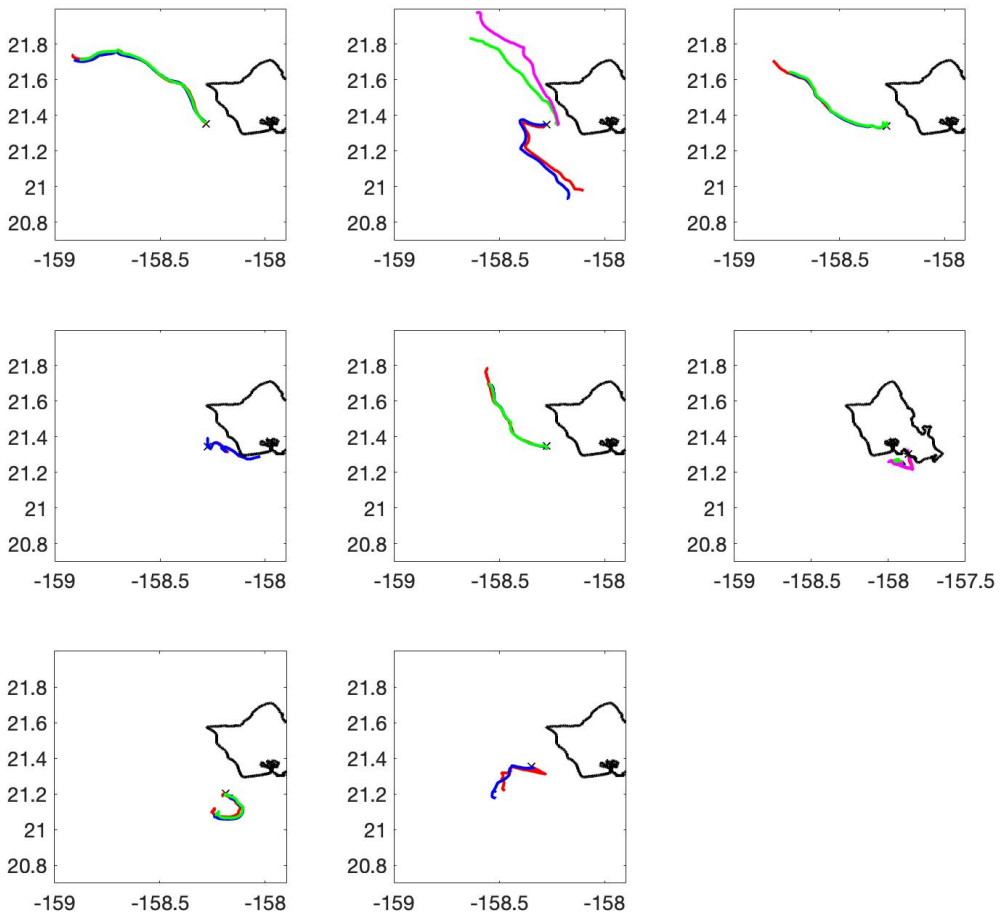

Figure 3.4: All 6 HOT cruise deployments and two deployments by the CG auxiliary. Deployments started in September 2015 (top left) and ended in May 2016 (bottom right).

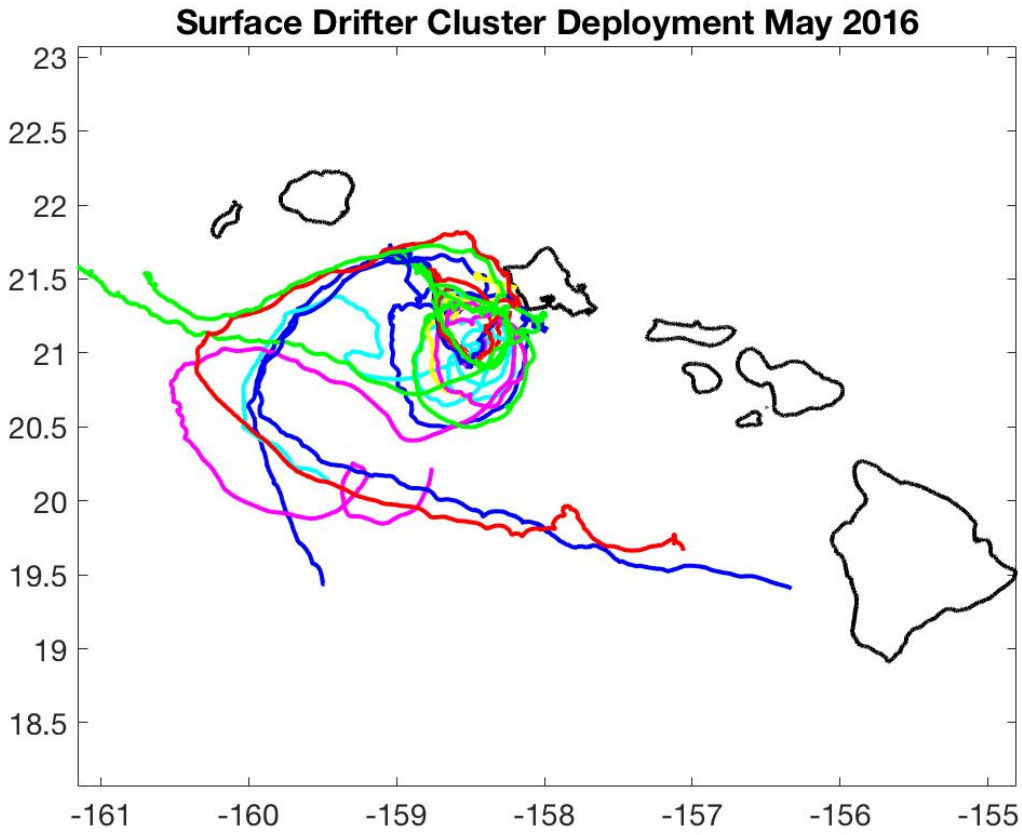

Figure 3.5: Cluster deployment trajectories from May 2016 deployment of 18 drifting buoys. Tracks are 30 days.

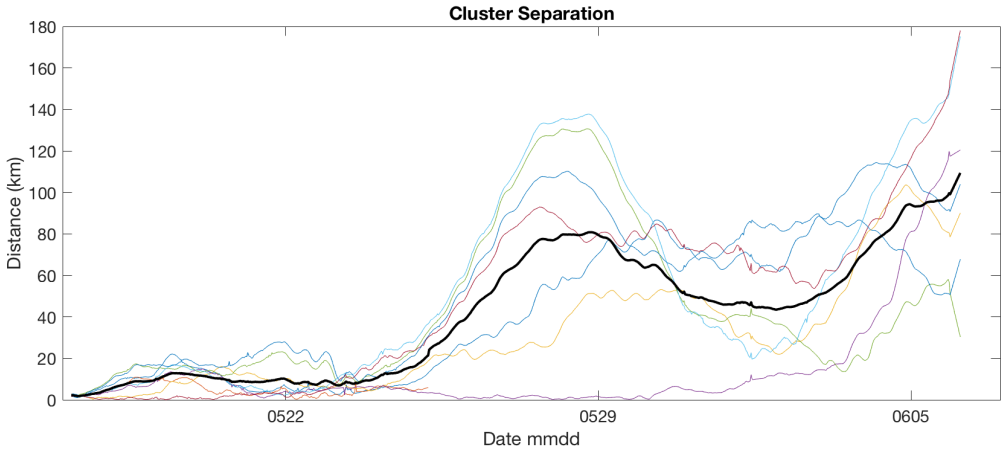

Figure 3.6: Cluster separation over the first three weeks. The cluster was deployed in May 2016.

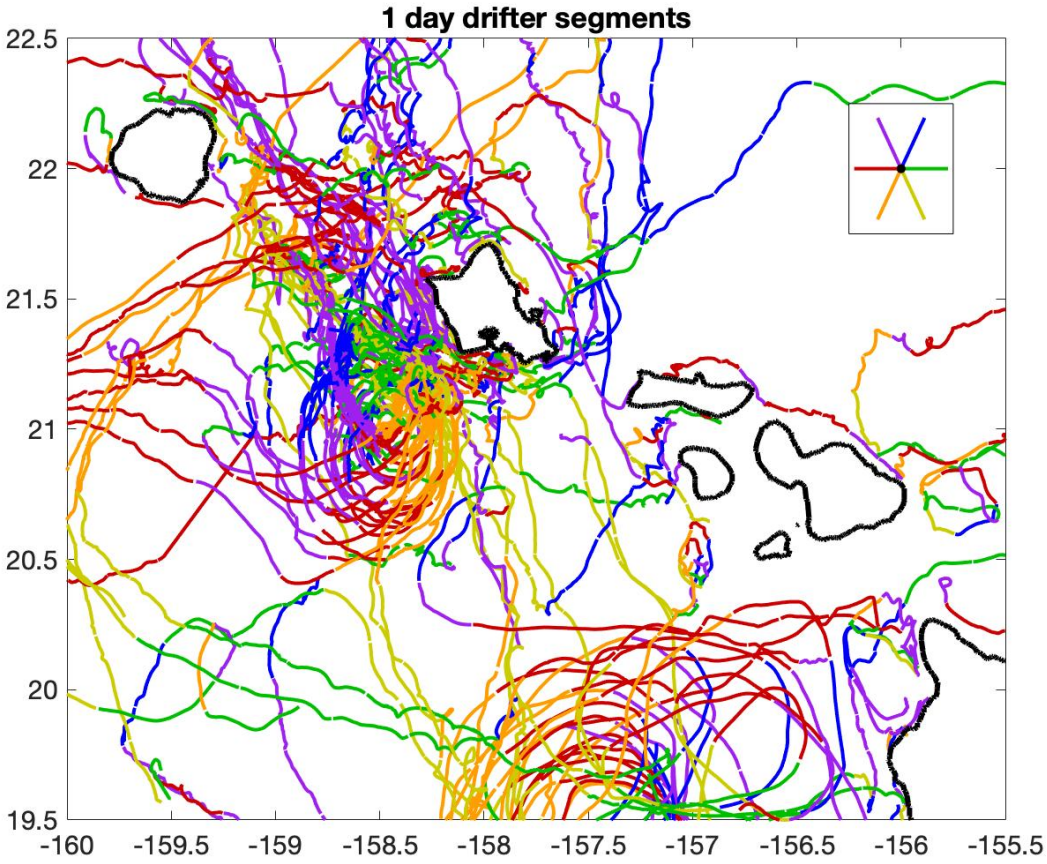

Figure 3.7: All drifters west of Oahu, broken down into 24 hour segments and color coded by direction

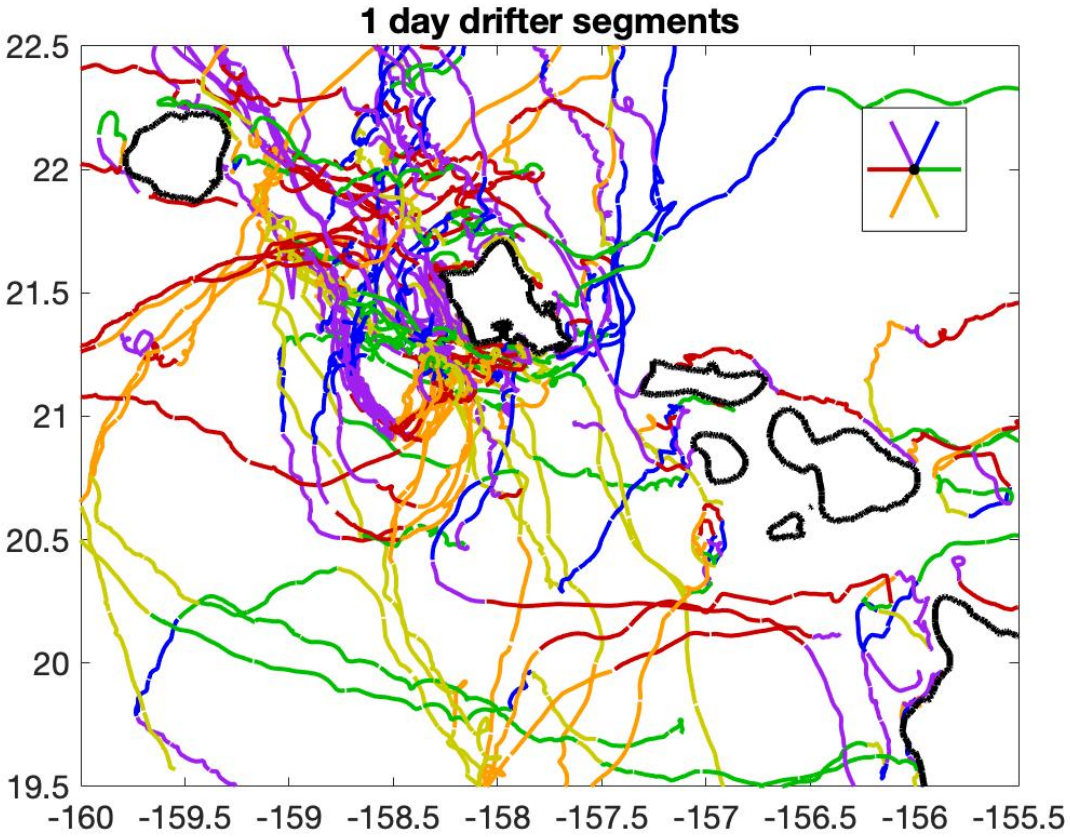

Figure 3.8: All non-rotating drifters west of Oahu, broken down into 24 hour segments and color coded by direction

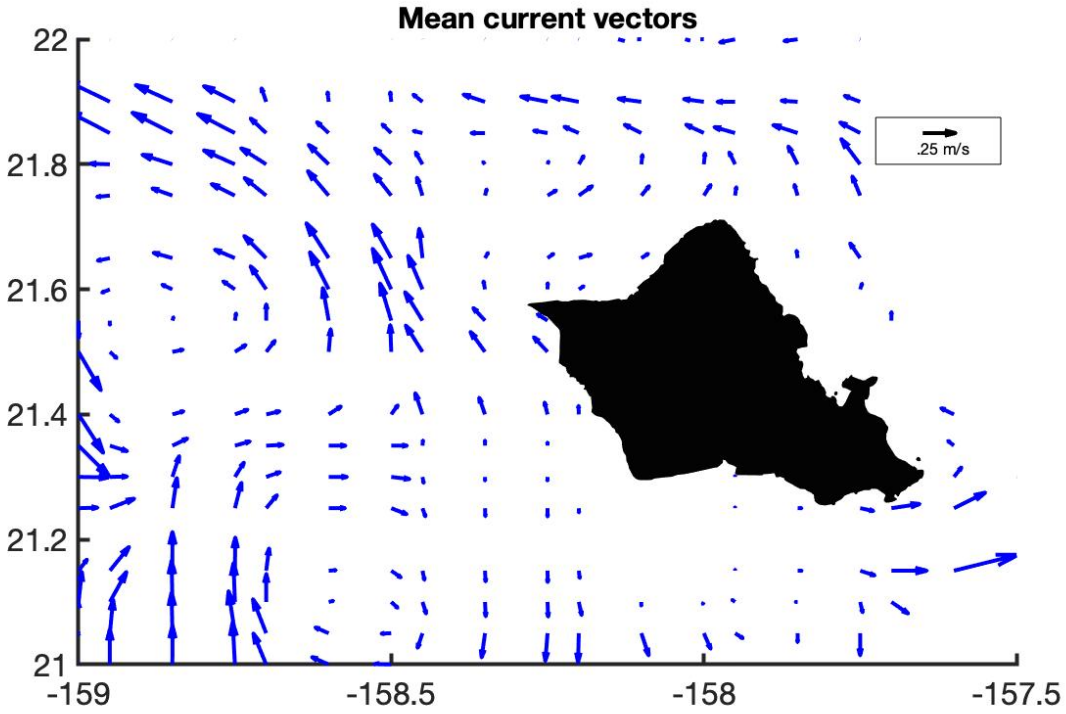

Figure 3.9: Mean currents calculated from surface drifter observations in 2015-2016 in the vicinity of Oahu

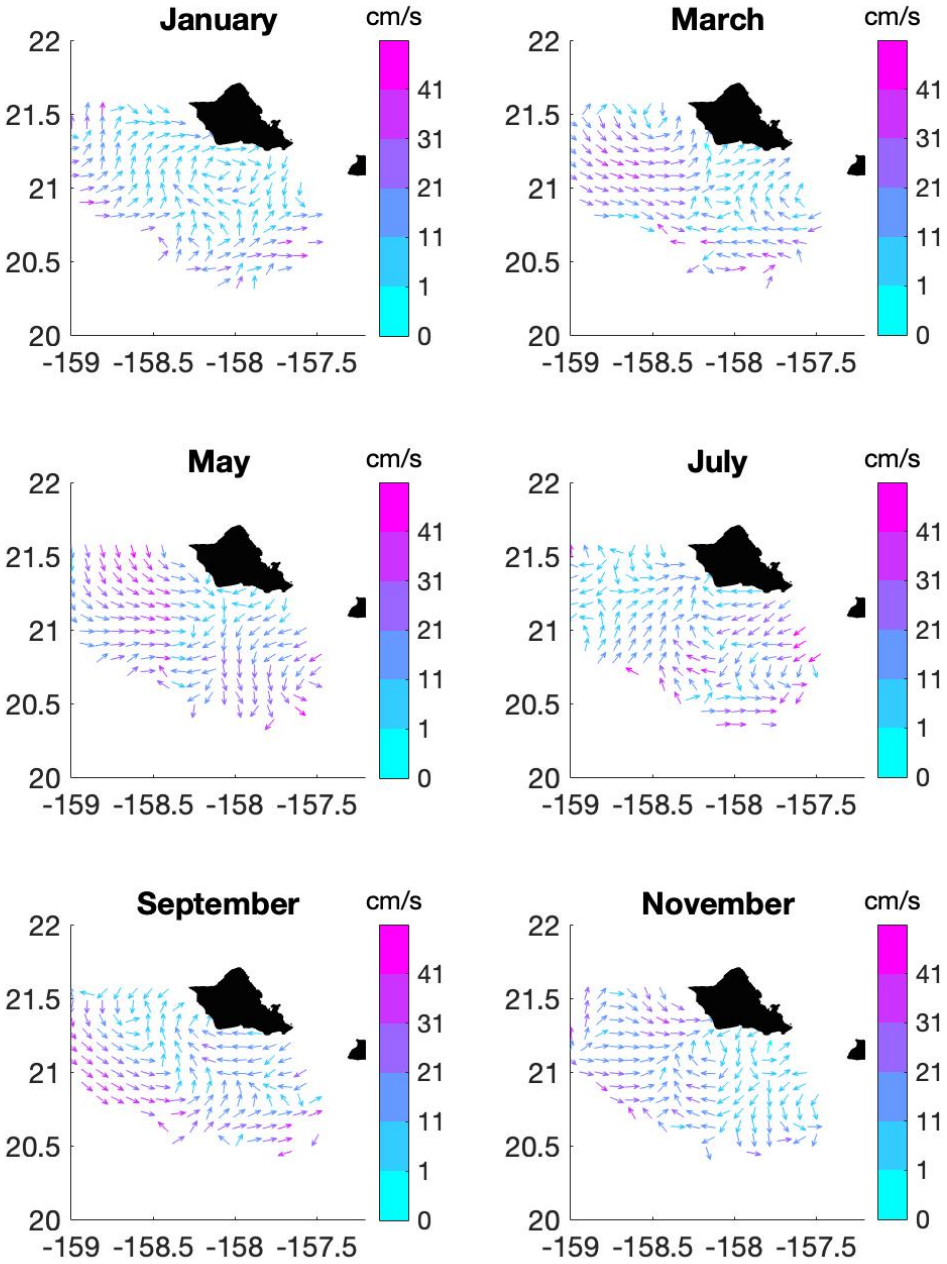

Figure 3.10: Monthly mean currents calculated from HFR off Oahu

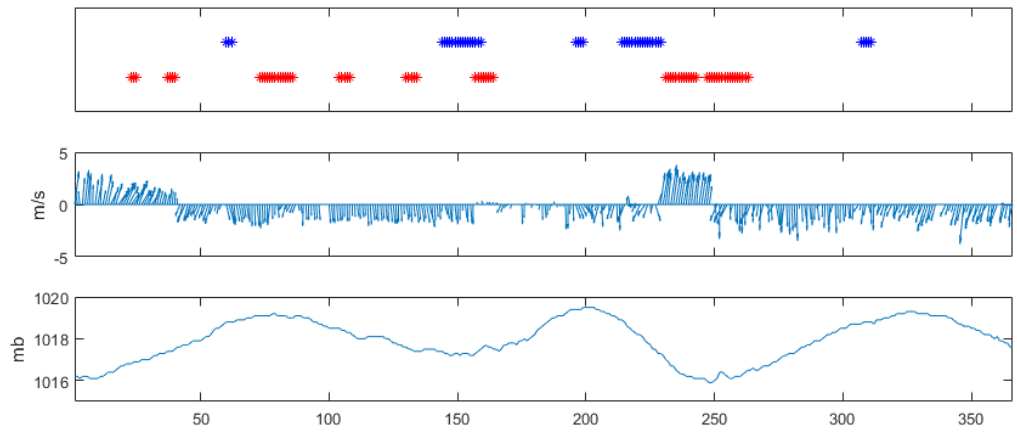

Figure 3.11: Top - The presence of anticyclones (blue stars) and cyclones (red stars) as observed in the HFR data for 2016. The x-axis is the day of the year (366 days, a leap year). Middle - Daily mean wind direction (in degrees clockwise from true North) and daily mean wind speed (in m/s). Bottom - Daily mean atmospheric pressure (in millibars). Both wind and atmospheric pressure were recorded at Honolulu International Airport, on Oahu.

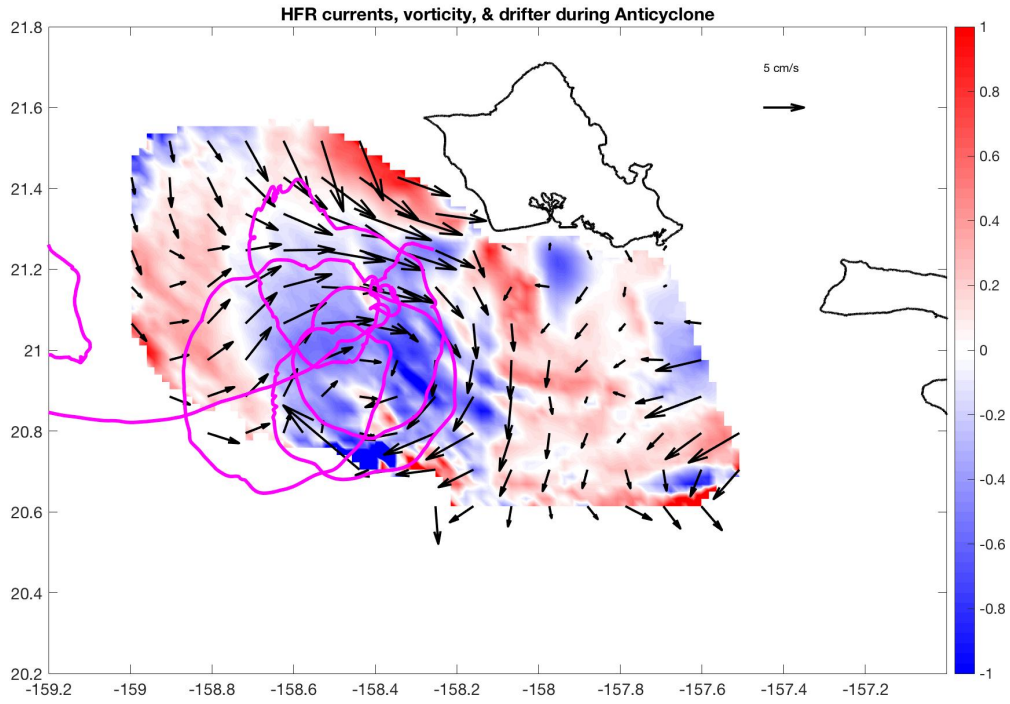

Figure 3.12: An overview of the May 2016 anticyclone located by both the High Frequency Radar surface currents (black vectors) and the surface drifters (only one buoy trajectory shown for clarity). Overlaid is the normalized relative vorticity (ω/f) calculated from the High Frequency Radar surface currents over 24 hours.

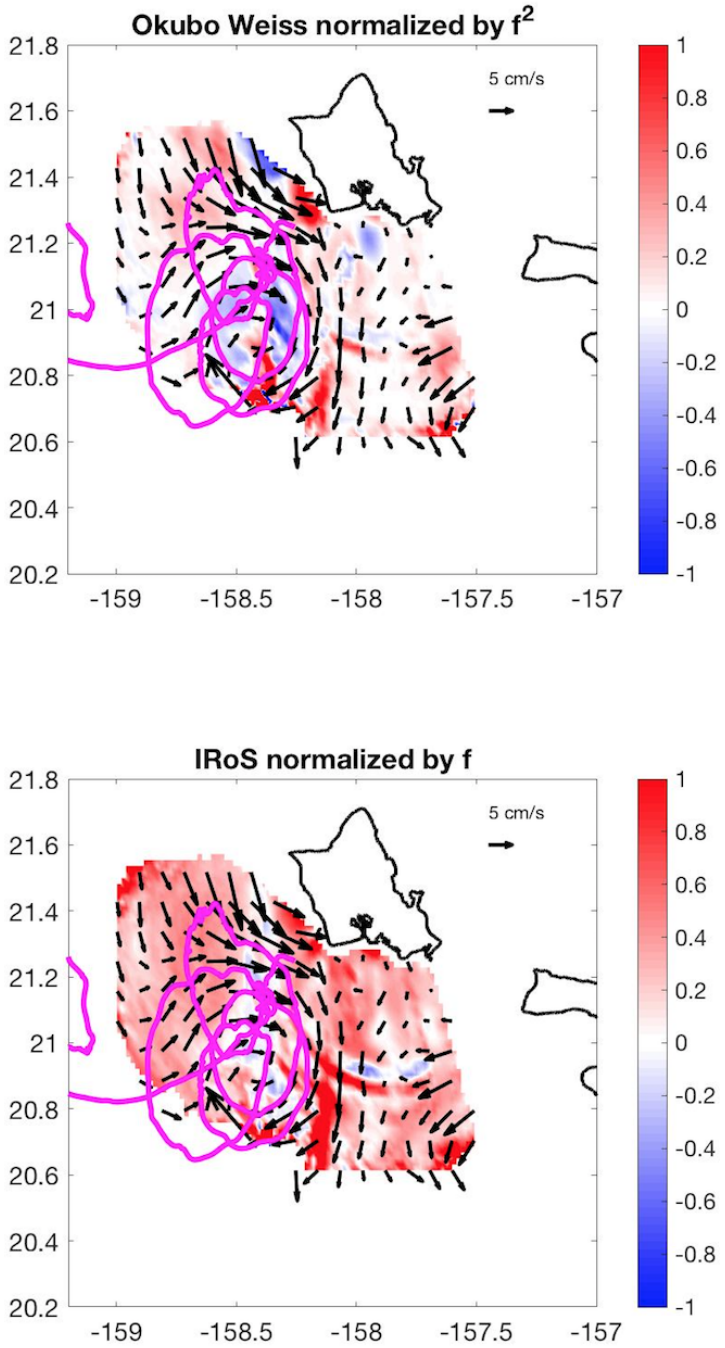

Figure 3.13: Top - Okubo Weiss Paramater normalized by f^2. Bottom - IRoS normalized by f.

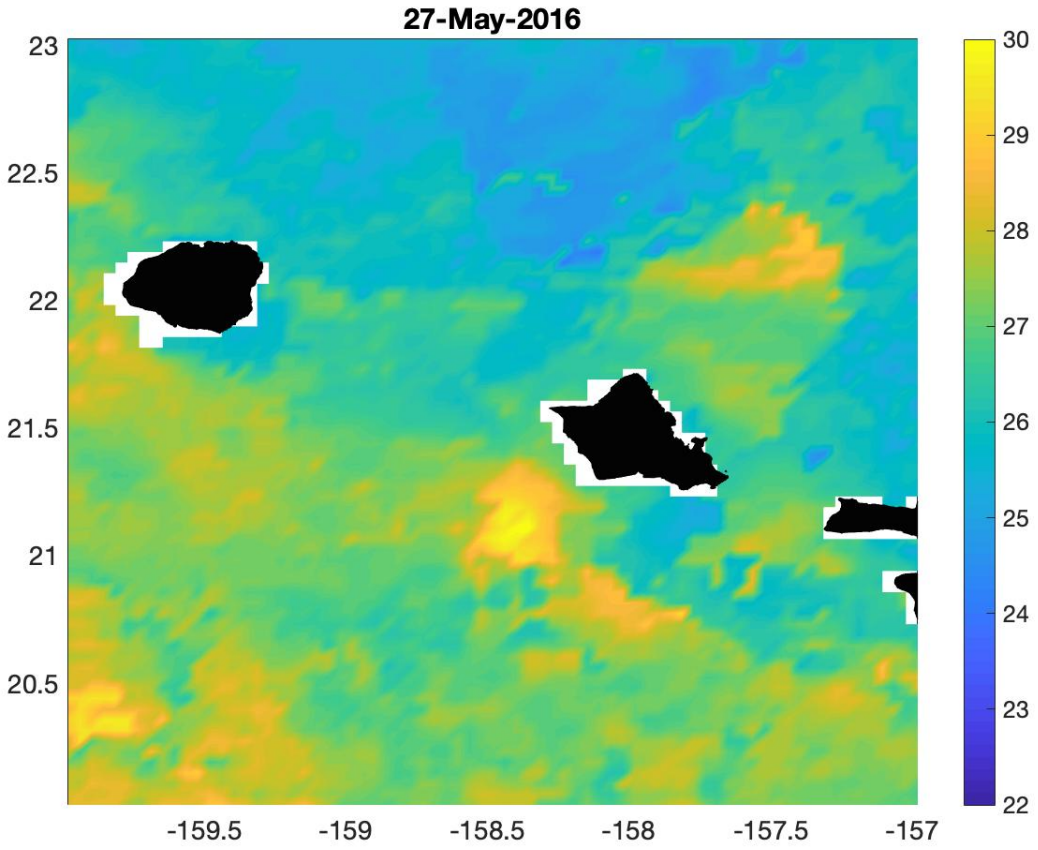

Figure 3.14: Mean sea surface temperature in degrees Celsius during the lifespan of the May 2016 anticyclone

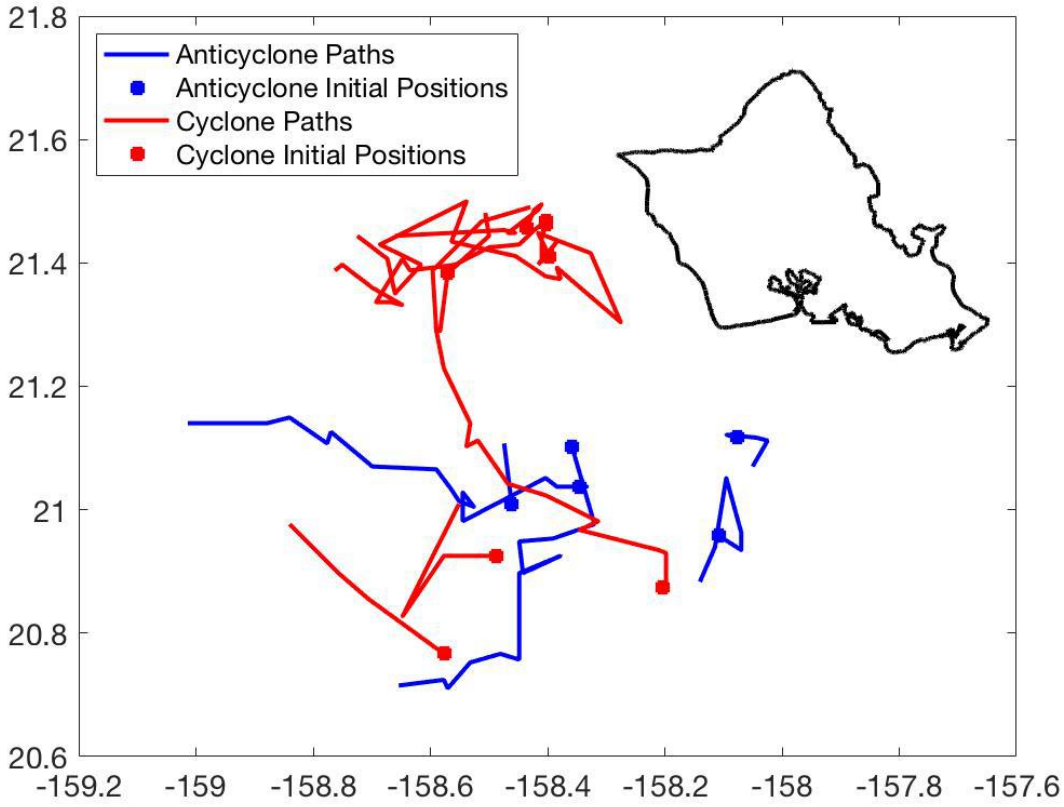

Figure 3.15: Travel patterns for both cyclones (red) and anticyclones (blue) observed from the High Frequency Radar surface currents in 2016. Boxes represent the initial position of the center of the vortices and the lines show the path of the center of the vortices during their lifespan in the High Frequency Radar coverage.

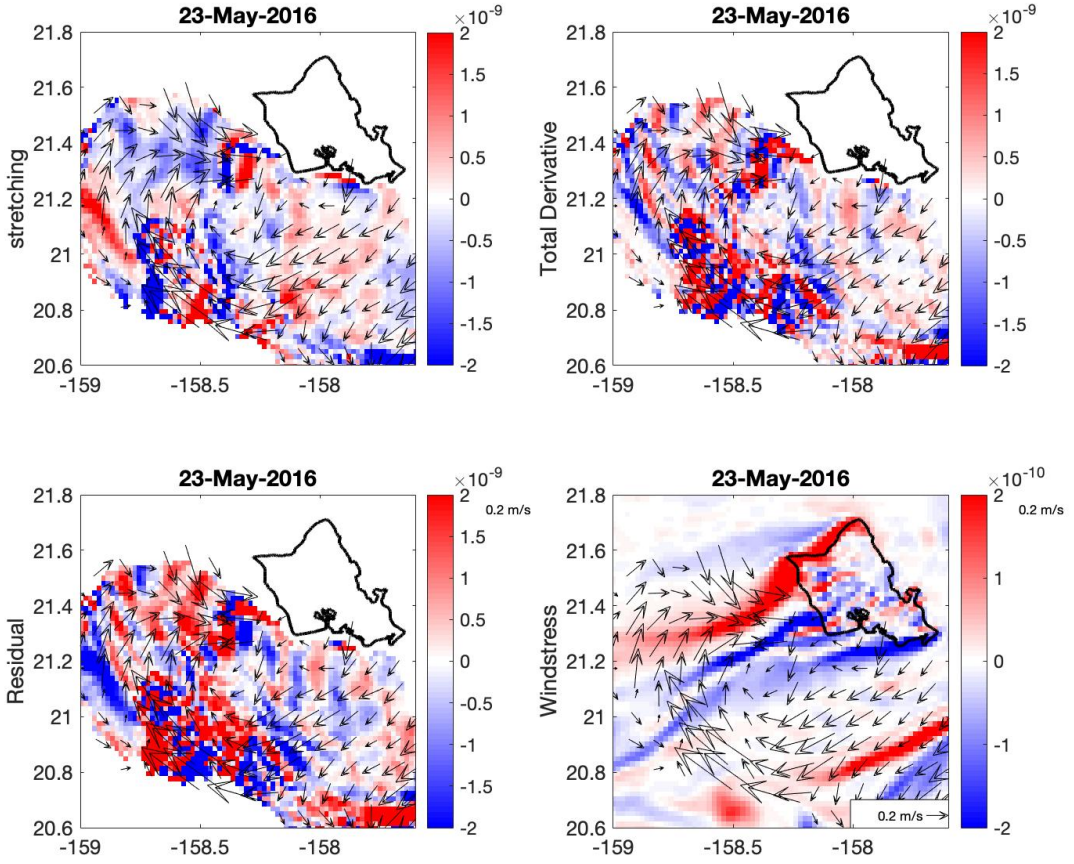

Figure 3.16: A snapshot of the vorticity balance terms for anticyclone # 2 in May, 2016. Units are s^{-2}. Show is the stretching term (top left), the Lagrangian Derivative (top right), the Residual (bottom left) and an estimate of Vorticity from Wind stress curl (bottom right).

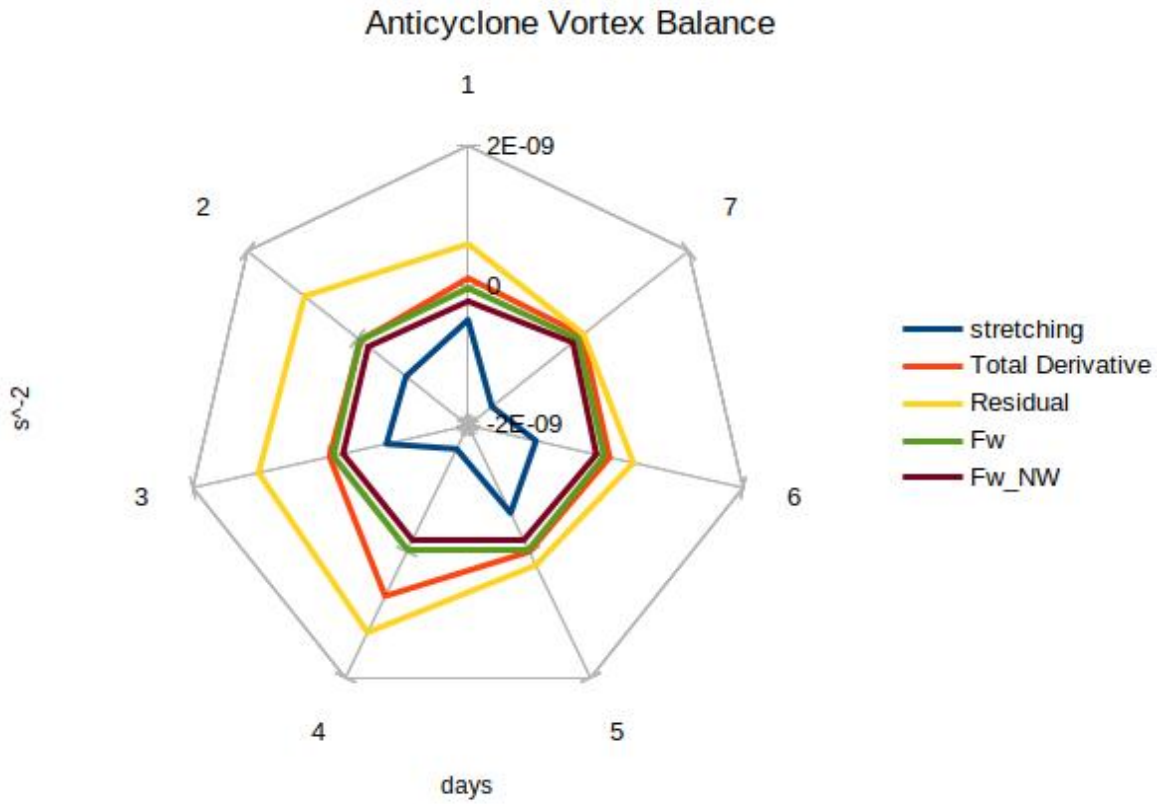

Figure 3.17: A timeseries of the vorticity balance terms for anticyclone # 2 in May, 2016. The terms are unbalanced are unbalanced for the first four days of the anticyclones life, but near balance for the next 3 days.

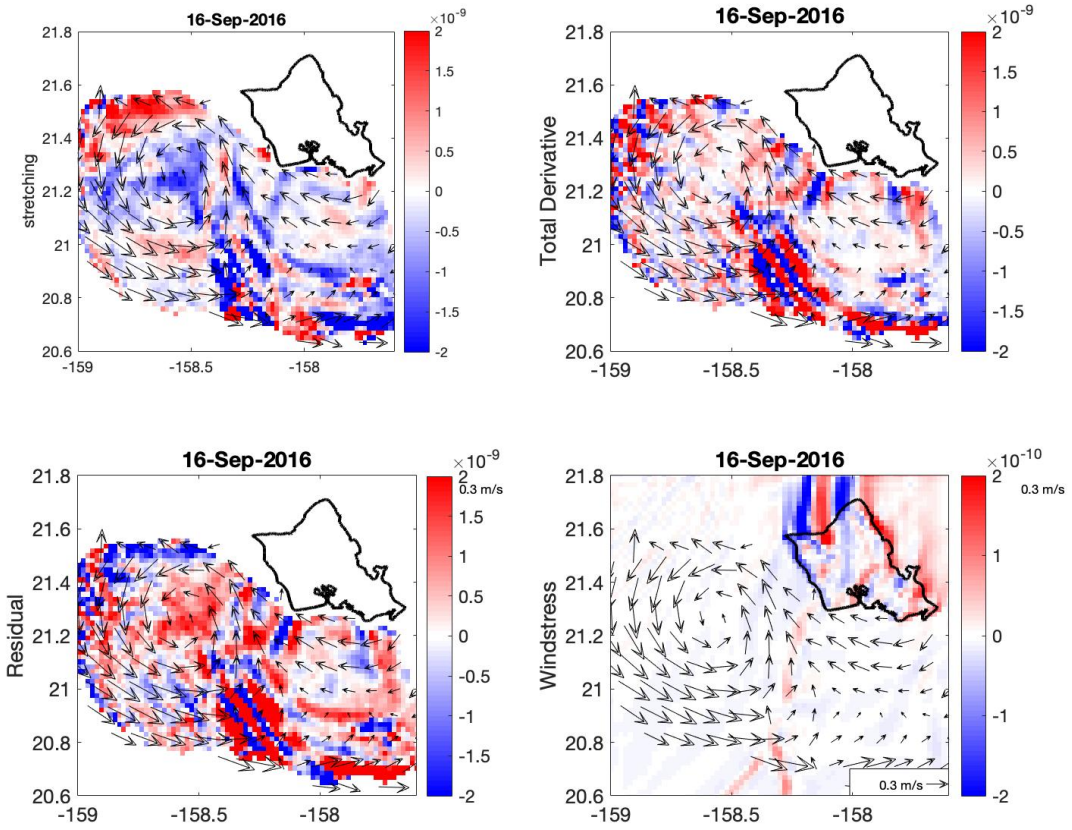

Figure 3.18: A snapshot of the vorticity balance terms for Cyclone # 7 in August, 2016. Units are s^{-2}. Show is the stretching term (top left), the Lagrangian Derivative (top right), the Residual (bottom left) and an estimate of Vorticity from Wind stress curl (bottom right).

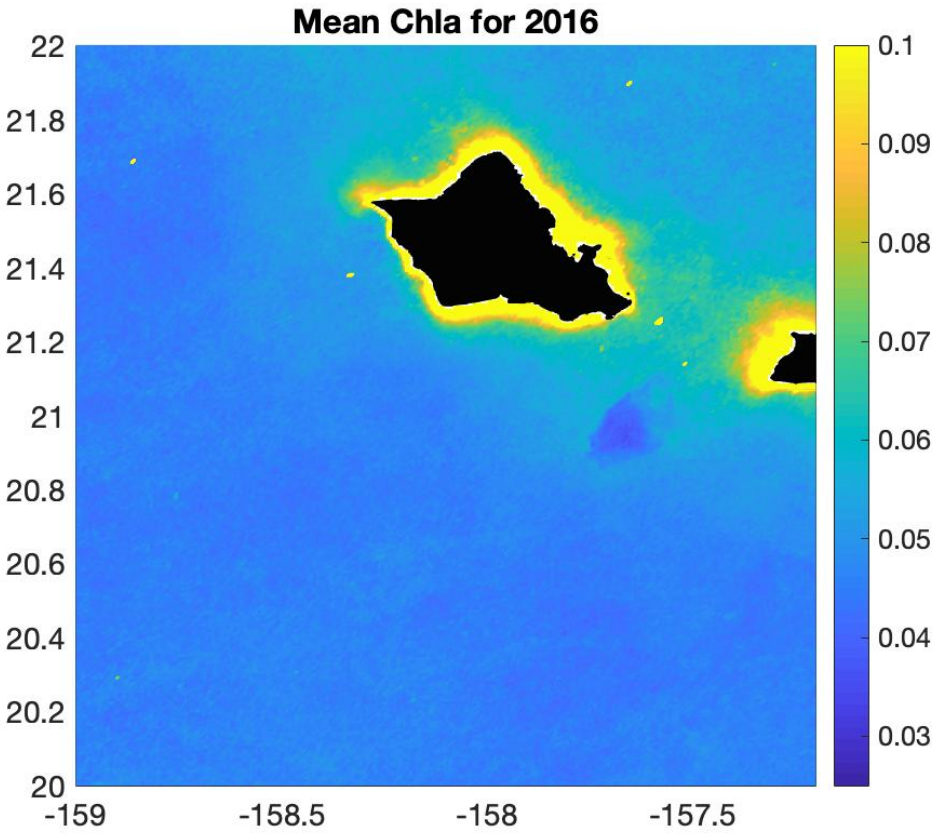

Figure 3.19: Mean chlorophyll a concentration for 2016

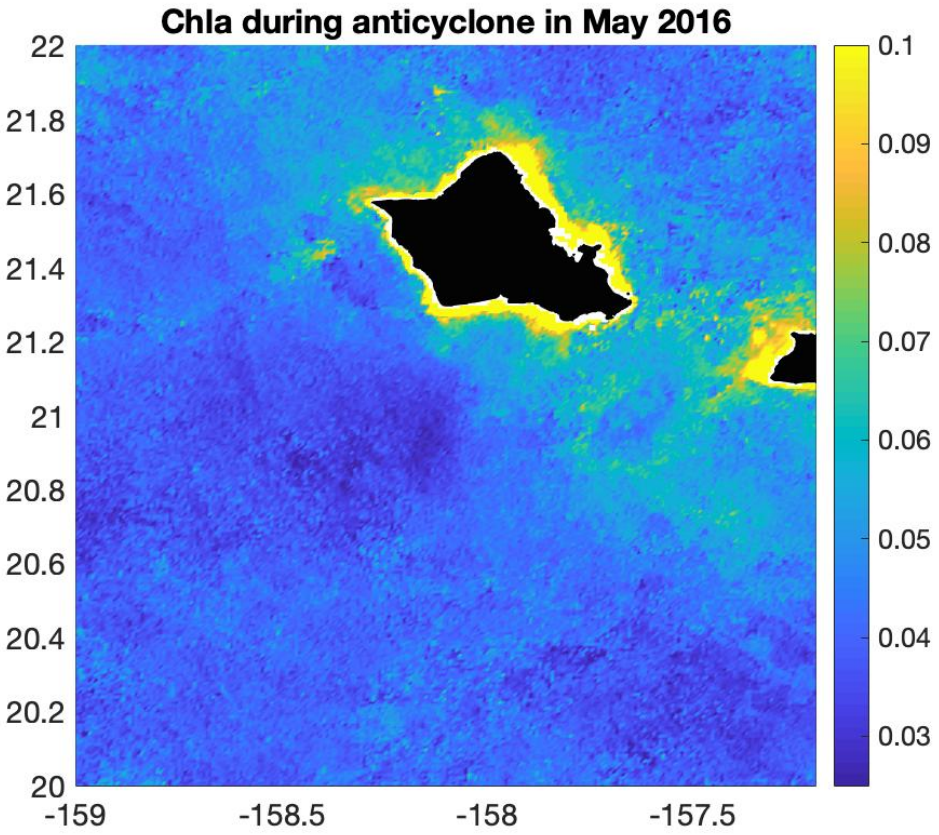

Figure 3.20: Mean Chla during duration of May 2016 anticyclone

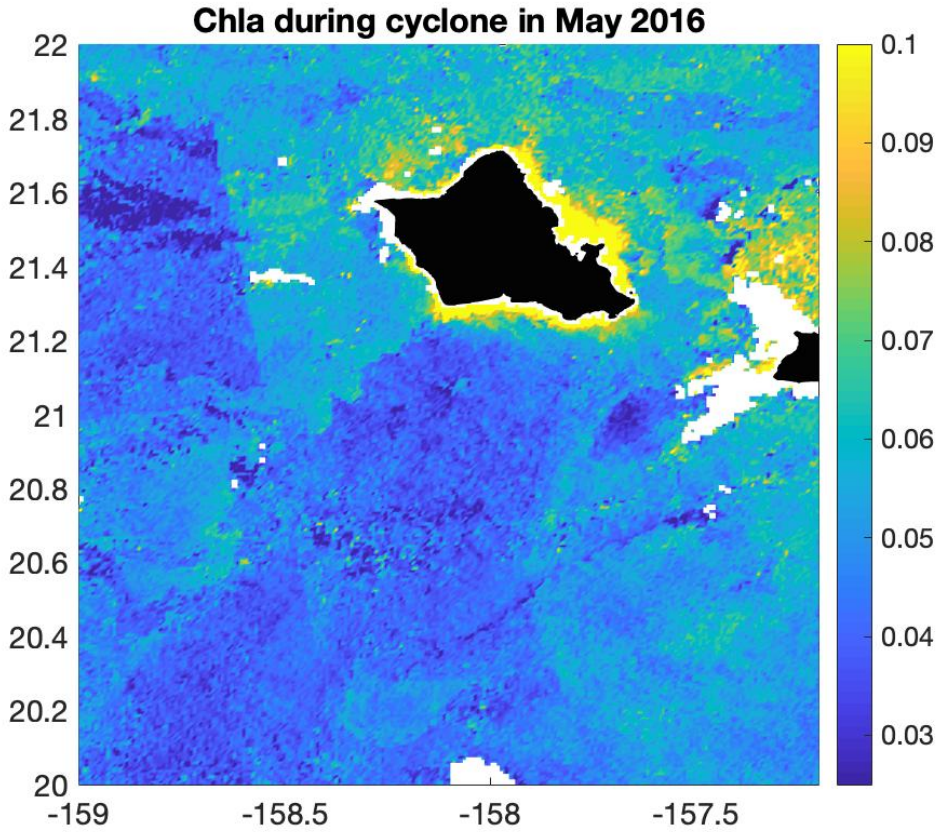

Figure 3.21: Mean Chla during duration of May 2016 cyclone located off northwest corner of Oahu

Chapter 4

An Estimation of Surface Drifter Leeway using Indirect Methods

Abstract

*Assumed non-slip surface drifters are often used in ocean studies to verify model-based currents and as the basis for indirect leeway estimates of search objects. However, no drifter is purely non-slip and quantifying the drifter's response to leeway forces is important in order to fully and accurately utilize the drifter's data. Here two surface drifter varieties, a Pacific Gyre Microstar and MetOcean Davis SLDMB were deployed in a gridded cluster formation off Oahu as part of a separate investigation into submesoscale flows. However, the deployment of the two varieties of surface drifters provided a nice data set to compare drifter behavior. The separation rate of the drifters over the initial drift period was noticeably different, with the Davis drifters having pair separation up to 8 km in 24 hours, exceeding the background noise separation rate of 1-2 km modelled in simulated drifters. In addition, indirect leeway estimates of each drifter revealed the Davis drifter had significant crosswind leeway (*1.2% *of the wind speed) that exceeded previous measurements. The crosswind leeway movement matched both the direction of the surface Ekman layer and the dominant direction of wave-induced Stokes drift. These results indicate a need for further studies using accelerometers and current profilers to determine which leeway forces contribute to the drifters' large crosswind leeway.*

4.1 Introduction

Surface drifters are often used to measure or validate ocean currents. These drifters usually have a minimal profile above the waterline to reduce wind impacts and are designed to drift with the top 1-2 meters of ocean current. One important use for surface drifters in operational oceanography is the validation of ocean current predictions from numerical models during search and rescue (SAR) evolutions. During a SAR evolution, surface drifters are deployed at the last known position (LKP) of the search object, and the magnitude and direction of the drifters movement is compared to output from various available numerical models. This information is then used to place a search pattern in a location with the highest probability of success. This use assumes that the leeway coefficients for the surface drifter are either known, or zero (meaning the surface drifter is only impacted by ocean currents, not wind forcing). Leeway, as defined by Allen (2005) is the movement of an object on the ocean's surface relative to the wind. Leeway can be broken down into a leeway rate (the speed of the object's drift through the water caused by the wind, usually measured in a percent of the wind speed) and leeway divergence (the angle of drift relative to the downwind direction). A diagram demonstrating each component of leeway is shown in Figure 4.1. Each object has different leeway coefficients due to size, freeboard, and sail area above and below the waterline. Leeway is calculated using either the direct method by measuring drift through water using attached current meters or the indirect method of subtracting an estimate of current drift from the total drift (Allen and Plourde 1999).

Effective surface drifters are designed to minimize slippage. Slip is unwanted motion in a drifter, defined as the difference between the movement of the drifter and the equivalent depth-averaged current velocity. Rockewell Geyer (1989) investigated the causes of slip in order to determine the water-following properties of drogued drifters. The causes of slip discussed included drag induced by shear currents (a difference in current velocity at the surface compared to the current velocity at the mean depth of the drogue), wind drag (referred to earlier here as leeway), and wave rectification. Davis (1985) discussed in more

detail the action of wave motion on a surface drifter. Their drifter design (discussed below, and used in this experiment) was created to minimize oscillatory motion caused by waves by averaging out the wave-induced drag coefficient over the depth of the drifter. They showed that to do this it required either a spherical shape, or a drifter that did not tilt in wave motion. While resolving all three causes of slip are ideal, it is often difficult to do. To investigate the slippage of surface drifting buoys we evaluated two main designs of surface drifters commonly used in SAR evolutions. Both designs are known as Self-Locating Datum Marker Buoys (SLDMBs). The first design is the Davis Drifter (Davis 1985; Davis et al. 1982), also often referred to as a CODE (Coastal Ocean Dynamics Experiment) -style drifter produced by MetOcean. This design has four underwater drag producing vanes at right angles from one another that catch the top 1-m currents. The vanes meet at a center metal rod that runs the length of the drifter. The vanes are attached to small floats using flexible line that keep the drifter buoyant and the instrument package above water. The floats are attached at the outermost limits of the vanes to reduce tilting motion. The second design is a Microstar drifter produced by PacificGyre that has a diamond shaped drogue centered at 1-m depth. Unlike the Davis Drifter, the Microstar has only a singular spherical 8 in. float above the surface. Detailed dimensions are shown in Figure 4.2.

Earlier works looked into the water-following properties of surface drifters. Kirwan et al. (1975) parameterized the drag forces acting a drogued drifter to estimate the effect of wind. They theorized the difference between water velocities and drifter velocities could be up to a 50% difference and as much as a 45° offset in angle. Results from a field experiment agreed with their predicted drag values. Rockewell Geyer (1989) obtained precise measurements of slip for mixed-layer drifters with 5-m long holey-sock drogues. The slip velocities ranged from $1 - 4cm/s$ in the downwind direction. This was followed by Niiler et al. (1995) who compiled results from multiple drifter studies looking at the slip of 15-m holey-sock and TRISTAR drogues. These were direct measurements of slip that compared well with previous theoretical estimates, however they were limited to less than $10m/s$ winds. Drogues

attached to surface drifters are often lost before the drifter electronics die out. Once the drogue is lost, the wind and shear-drag forces are altered. Poulain and Warn-Varnas (1996) found that undrogued drifters tended to move 12° to the right of the wind and with a speed of 1.6% of the wind speed. This was followed by Pazan and Niiler (2001) who investigated the difference in the leeway of drogued drifters to undrogued drifters. However it wasn't until Poulain et al. (2009) that the first direct measurements of a Davis type drifter was conducted. Due to the size of SLDMB drifters, direct measurements of leeway are difficult. Direct leeway measurement requires a current meter to be attached to the drifter, which can alter its drift characteristics if not placed properly, also most available current meters are large and hard to attach to the small SLDMBs. One previous study, presented at the 2002 LAPCOD meeting (Poulain et al. 2000) found that Davis-type drifters had no significant leeway in the downwind direction, but had measurable leeway in the cross-wind direction ($0.1 - 0.2\%$ of the wind speed) as well as significant leeway to the right of the wind caused by vertical velocity shear ($0.3 - 0.5\%$ of the wind speed). Because the leeway of SLMDB drifters is assumed to be zero, these are often used as the baseline for indirect measurements of leeway. This allows leeway to be estimated for objects without a current meter, if the object is near an SLDMB field, as discussed in Morris et al. (2008). However, if there is leeway inherent in the SLMDB design, this can lead to errors in the other object's leeway measurements if calculated indirectly from SLMDB drift. Here we use data from a drifter deployment conducted offshore of Oahu, Hawaii to investigate the leeway and drift properties of two types of SLMDB drifters.

4.2 Methods

Two different drifting buoy makes were used in this study. The first, representing the Davis Drifter was the SLDMB made by metOcean. These were second generation SLDMB drifters that transmit their data via the Argos network. They were programmed for SAR mode, meaning that for the first 24 hours after deployment they transmitted every 10

minutes, then they transmitted for their remaining lifespan at 30 minute intervals. Their expected operating life at $10°C$ is a minimum of 15 days (metOcean 2016). The second buoy make was the PacificGyre Microstar drifter, also configured for SAR. These Microstar drifters transmitted via Iridium and were programmed to record and transmit every 30 minutes, giving them expected lifespans of 1-3 months.

The SLDMBs were deployed in a cluster formation in the coastal waters off Southwestern Oahu in May, 2016. A 3x3 gridded pattern, with $2\,km$ cross ($2.8\,km$ diagonal) spacing was used in the deployment with the center grid point at $21°13.9'N, 158°14.4'W$. One Microstar drifter was deployed at each grid point (nine locations, grid positions referenced by number from top left as 1, moving left to right, then top to bottom with position 9 in the bottom right). One Davis Drifter was deployed alongside each Microstar with approximate 200m spacing. The initial positions of the grid points were offset based on the on-scene currents, resulting in a square grid at the time the last drifter was placed in the water. The cluster deployment lasted 1.2 hours. Warm sea surface temperatures ($> 24°C$) in the region meant the drifters battery lives were not reduced due to cold temperatures. Lifespans for the metOcean SLDMBs for this deployment were between 30-65 days, while the PacificGyre Microstars lasted upwards of 6 months. Of the eighteen surface drifters deployed in the cluster, all nine Microstars successfully deployed, but only 7 Davis Drifters successfully deployed. Two Davis drifters tested positive before the deployment (grid positions 5 and 8), but did not activate once in the water. Two Microstar drifters were picked up by fishing vessels on days 3 and 18 of the deployment. Given the availability of surface drifter data, emphasis in this study was placed primarily on the first 48 hours (when all nine of the Microstars and all of the seven Davis that activated upon deployment were available) and secondary analysis was the first 30 days. After 30 days, the Davis drifter batteries began to die, making analysis of drift characteristics less robust due to a sharp decrease in available data points.

For this comparison, the geographical position and sea surface temperature recorded every 30 minutes were extrapolated from each drifter, starting with the bottom of the hour after deployment concluded (0430Z). Missing or bad position data were linearly interpolated for the bottom and top of each hour throughout data gaps. Repeat exact geographical positions that resulted in a speed of zero were ignored and linearly interpolated as if the position was missing.

4.3 Drifter Dispersion

The first ten hours of the drift were dominated by westward flow, after which the mean velocity shifted to the southwest (Figure 4.3a). Tidal currents at the time of launch were slack and then building to maximum flood until 1100Z. According to NOAA National Ocean Service (2018), average flood direction in southwestern Oahu coastal waters is $122°T$ at a speed of $0.9kts$. The drift of the cluster during the first 10 hours was west northwestward, as opposed to the southeastward flood, indicating the initial movement of the drifters was not tidally dominated. The flow patterns shown in Figure 4.3b-d indicate the buoys remained in the same flow regime for the first 2 days.

An estimate of dispersion was calculated by finding the average root mean square separation of each drifter from the center of the cluster over the first 24 hours for each drifter type (Figure 4.5). As discussed above, for the first ten hours the drifters moved westward and the shape of the cluster was maintained, with an average root mean square separation of 3km. However, after 10 hours, the cluster was stretched in the meridional direction with a North-South limit of 17km at 24 hours of drift. The spaghetti diagram showing the first 48 hour trajectories and resultant cluster stretching is shown in Figure 4.4. Both the Davis and Microstar drifters maintained similar cluster deformation, ending the 24 hour drift with an average root mean square separation from the center position of 8.5 and 7 km respectively. However, just looking at the deformation of each cluster's shape does not highlight the differences in drift patterns between each buoy type.

A second estimate of dispersion was calculated by finding the average root mean square separation of each drifter pair over the first 24 hours. In contrast to the previous estimate, which looked at how the shape of the cluster distorted, this estimate focused on how each neighboring pair of drifters separated. The calculation was run for each Microstar pair, each Davis pair, and each Microstar to Davis pair. For the Microstar to Microstar separation (Figure 4.6, top, with blue shaded regions indicating standard errorbars), the initial mean separation (2.2 km) is set by the grid spacing (2km horizontal and 2.8km diagonal) of the initial positions. The cluster then moved in a cohesive fashion, with pair separation remaining fairly stable, ending 24 hours later with a mean separation of just 2.3km. The Microstar to Microstar pairs had a separation rate of $< 0.1\, cm/s$. This indicates that even as the cluster was being stretched, the relative positions of the drifters to each other in the cluster remained the same (i.e. the drifters that started in the southern part of the grid moved south, and the northern positions stretched to the north). This is in contrast to the behavior of the Davis drifter pairs. The separation of each Davis-Davis drifter pair was calculated over the first 24 hours in the same manner described above. The mean separation (in km) with standard errorbars (blue shaded region) is shown in Figure 4.6, bottom. The initial mean separation (2.7 km) was set by the grid spacing (2km horizontal and 2.8km diagonal) of the initial positions, as was the case for the Microstar. The Davis cluster appeared to follow the same flow pattern as the Microstar cluster (Figure 4.4), but each pair separated in a near linear fashion at a much faster rate than the Microstar drifter pairs. A linear regression of the separation over time resulted in a slope of $0.15\, km/h$, r^2 of 0.92, ending with a mean separation of slightly over 10 km in 24 hours, or an 8-km disengagement when the initial spacing is removed. A large increase in pair separation would indicate that the relative positions of the drifters in the cluster did not stay the same over the first 24 hours of drift. This can be confirmed by looking at the separation between each Microstar and Davis drifter pair. At the initial positions of the cluster grid, these drifter pairs started 200m apart. If both types of drifters maintained their relative positions in the cluster, this average separation should not substantially increase.

However, that is not the case. As shown in Figure 4.6, middle, the separation after 24 hours reached a mean of 4.1 km. A linear regression of the separation revealed a slope of 0.084 km/h, r^2 of 0.95. Looking at the individual tracks, Davis drifters tended to detach from their Microstar pairs, and in multiple cases moved in opposite directions from their pair, changing their relative position in the cluster. The Davis drifters tended to creep to the northwest as their Microstar pair moved to the westsouthwest. So even though the clusters deformed in the same manner, the behavior of each drifter types in the clusters did not match. This indicates that there is a significant difference in the resultant movement of each drifter type, even when subjected to the same forces. So what is the cause of this difference? Is it a difference in leeway due to drifter design or is it an artifact of the errors caused by different quality positioning sources? And secondly, which drifter separation rate and behavior more closely resembles the background flow? For the first question, if the separation is caused by varying leeway, the motion of the drifters could be explained by examining leeway forcing. This was completed by indirectly measuring the leeway of each drifter type. For the second question, in order to investigate how drifter separation compares to background flow, simulated cluster deployments were drifted using two ocean models: Hybrid Coordinate Ocean Model (HYCOM) surface currents and Hawaii Regional Ocean Model (HROMS) surface currents and compared to the actual trajectories and separation behavior.

4.3.1 Predicted drift of a zero leeway surface drifter

In the U.S., the Search and Rescue Optimal Planning System (SAROPS) program is used to predict the drift of search objects. SAROPS uses a Monte Carlo simulation to drift up to 10,000 particles and produce a probability map. There are two forces acting on a particle in SAROPS: ocean currents and wind, which it applies to the particle through the leeway coefficients specific to that search object (information on the determination of leeway coefficients can be found in Allen 2005 and Allen and Plourde 1999). For each time step, the simulation takes the closest three zonal and meridional velocity points and uses

a weighted average to drift the particle. In addition, at every time step uncertainty is added to the drift. The simulation perturbs the speeds by using a random draw from a normal distribution, however random draws for each particle for increasing time steps are correlated:

$$\rho(\Delta t) = e^{-\alpha \Delta t} \tag{4.1}$$

where α is chosen so that $e^{-\alpha 60} = 1/2$. At the end of the simulation, SAROPS generates a probability map for that time using the density of the particle distributions at the end of the simulation. For SLMDBs, the leeway is assumed to be zero in SAROPS and these particles are drifted using only the surface currents, wind is ignored. A simulation of zero leeway SLMDB drift over the time period of the cluster deployment was conducted using the same drift algorithm described above. Two sources of ocean surface currents were used to force the drift model, current predictions from HYCOM and HROMS. Surface zonal and meridional ocean currents were extracted from both HYCOM and HROMS once every three hours for a rectangular area defined by the limits $19° - 25°N$ and $164° - 155°W$. This box was chosen based on the outer limits of the trajectories of the surface drifters after 30 days. Horizontal grid spacing for HYCOM was 0.08° or approximately 9km, while it was 4km for HROMS.

The simulations were run for the first 48 hours, and for the full 30 days. Figure 4.7 shows the actual trajectories of the Microstar drifters after 48 hours compared to the drift predictions from Hycom (red lines) and HROMS (blue lines). Over the first 10 hours while the drifters moved west-northward with an average speed of 25 cm/s, HYCOM recreated a similar pattern. However, after 10 hours, the paths of the drifters diverged from the predictions. The actual drifters moved in the southwest direction and remained relatively coherent. HYCOM moved the cluster northward, and HROMS back to the east, towards Oahu. Looking at the 30 day predictions (Figure 4.8) highlights a major difference between actual and predicted. The drifters encountered a persistent anticyclone located to the southwest of the island of Oahu that was not resolved in either HYCOM or HROMS

models. However, even though both models did not replicate the actual trajectories of the drifters, the output can be still be used to simulate clusters. The dispersion of these simulated clusters can be used to validate or invalidate the behavior of the actual drifter clusters. For each data source (HYCOM and HROMS) a simulated cluster deployment was run with zero leeway and using the 9 initial cluster grid positions. Start time of the simulation matched the start time of the actual cluster deployment (0430Z17MAY2016 when the final drifter in the grid was deployed). The average root mean square separation of each simulated drifter pair over the first 24 hours is shown in Figure 4.9. The separation of the simulated drifter pairs mirrored the behavior observed by the Microstar pairs, when separation between neighboring pairs remained nearly fixed at the initial grid spacing over the first 24 hours. This indicates that given the flow conditions, the drifters in the cluster should have maintained their relative positions and the behavior of the Microstar drifters is what should have been expected from both sets of buoys, assuming zero leeway.

4.3.2 Comparison of Drifter Speeds

The speed of the drifters was calculated for every time step by taking the distance between the previous and current geographical position, calculated using the haversine formula for the great circle distance between two points, and dividing through by the time interval (30 minutes). The daily mean speed of each drifter type was calculated for the full 30 days. Neither drifter type had daily mean speeds consistently outside the 95% confidence intervals during the 30 day period. The mean daily speeds ranged from $15\,cm/s$ to $45\,cm/s$ over the 30 day period. During the first three days, while both drifters remained in the same flow pattern, mean drift speeds were nearly identical, as seen in Figure 4.10 however, after three days the drifters separated and their mean speeds diverged. While the mean speeds of each drifter type were similar, the speeds of individual drifters and the distribution of speeds for each drifter type was different, even during the initial drift period when the drifters remained in the same flow regime. Histograms of drifter velocities over the first 48 hours are shown in Figure 4.11. Only the first 48 hours of drift was used for this comparison because the drifters

remained together, in the same flow pattern, and all drifters that activated upon deployment were still active. After three days one drifter was no longer transmitting and the comparison of drifter speeds after three days would more likely reveal changes due to differences in ocean currents, rather than differences in buoy performance. The mean speed of the Microstar drifters over the first 48 hours was $21.2 \pm 12.6\, cm/s$. The mean speed of Davis drifters was slightly higher but had much higher standard deviation, $22.9 \pm 26.0\, cm/s$. This is shown in Figure 4.11: bottom right, the Davis drifters had an uneven distribution with a much higher occurrence of slow speeds (from $0 - 5\, cm/s$) and a larger number of drifters that showed increased speed ($> 40\, cm/s$; up to $95\, cm/s$). The high occurrence of extremely low speeds remained even after the repeat geographical positions were interpolated. For comparison, histograms of simulated drifter speeds are shown in Figure 4.11:top left (HROMS) and top right (HYCOM), for the first 48 hours of the simulation. HROMS simulated drifters recorded the lowest mean speed at $13.2 \pm 6.1\, cm/s$, which is $8\, cm/s$ slower than the observed drifter's mean speeds. HYCOM drifters recorded an average speed of $17.3 \pm 7.3\, cm/s$, which is $3.9\, cm/s$ slower than observed.

4.4 Leeway of Surface Drifters

One explanation for the disparity in drifter dispersion and speed could be due to differences in the leeway drift of each drifter type. The addition of motion induced by wind forces could increase the speed, or change the direction of a drifter's movement. However, in order to estimate leeway from these drifters, it must be calculated indirectly.

4.4.1 Estimating Leeway indirectly

The leeway of an object does not just represent the result of wind on a drifting object. As detailed in Brushett et al. (2014a), the total drift of an object is the sum of the drift caused by the currents and the drift caused by leeway. However, inside both of these sources of drift are subcategories. The drift caused by currents can be thought of as the superposition of the

drift caused by surface currents and the drift caused by stokes drift (small scale currents caused by both local sea waves and swell). The drift caused by leeway can similarly be broken down into the drift caused by wind upon the surface of the ocean and the impact of waves. Without instrumentation measuring pitch and roll, the impact of waves cannot be differentiated from wind-driven leeway. In addition, without direct measurement of speed through the water, the leeway must be calculated indirectly.

Direct calculations of leeway require measuring speed and direction through the water, as well as local wind velocities. Linear regressions to compare the speed through water to the wind speed (using 10m winds as standard) allow an estimate of leeway drift to be calculated, often measured in a percent of the wind speed, represented by the slope of the linear regression. In this method ocean currents have been negated due to the use of speed through the water as opposed to speed over ground. For indirect estimates of leeway, surface current velocities must be removed from the velocity of the drifter before leeway is calculated. In both methods, these leeway estimates include impacts from stokes drift, waves, and wind. It has been shown by Breivik and Allen (2008) that leeway impacts caused by wave motion can be ignored for objects smaller than one half of the wavelength of the average wave. The mean peak wave period obtained from the Wave Watch III model for the first 48 hours in the deployment region is around 10s. Assuming deep water waves due to a depth exceeding 1000m, a 10s wave corresponds to $\sim 156m$ wavelength. These small drifters easily meet that criteria. This means that measurements of leeway for the surface drifters will comprise motion caused by winds, stokes drift caused by sea waves and stokes drift caused by swell. The leeway caused by the stokes drift from local wind driven sea waves will predominantly be in the downwind direction. Leeway caused by stokes drift from swell could occur in any direction and would therefore be wrapped into both the downwind and crosswind leeway estimates.

In order to remove the surface currents from the drifter's motion, the surface velocities must be known. In most calculations of indirect leeway on small objects, these

measurements of surface currents come from drifters deployed alongside the object. The drifter is assumed to have zero leeway and acts as a proxy for measurements of surface current speed. However, in this case, the drifter is the object of interest and zero leeway cannot be assumed. Estimates of surface current velocity could be gained from using available observations, such as High Frequency Radar (HFR), or modelled current data (such as HYCOM and HROMS). However, HFR available in the region does not cover the entire domain of the drift and the poor performance of HYCOM and HROMS in predicting the drift direction and magnitude, as well as the discrepancies in mean velocities exclude them from consideration. Instead the mean behavior of the drifters themselves were used to adjust the individual drifter speeds at each time step. In order to do this, the drifter speed data for the leeway calculation was confined to the first 48 hours, when the drifters remained in a cohesive grouping. The 48 hour window was broken down into two periods: the first 10 hours when the drifters moved to the west, and the next 38 hours when the drifters moved to the southwest. For each window, the mean zonal and meridional velocities of all the drifters over that period was subtracted from the drifter's movement, leaving behind the residual. This residual does not necessarily correspond directly to speed through the water, but instead represents the movement of the drifters caused by smaller scale processes such as surface Ekman forcing, wind leeway, stokes drift and waves. Since these are all of interest in leeway calculations, this residual can be used an estimate of the speed through the water for leeway calculations. Hourly wind data for the leeway estimate was retrieved from the Weather Research and Forecasting (WRF) regional model for Maui-Oahu at 2-km resolution. For each drifter position at each time step, the wind speed and direction was interpolated from the neighboring four gridded WRF data points. The estimated drifter speed through the water was then matched with the 10m wind speed and direction for the position over the 48 hour period.

4.4.2 Leeway Results

Results showed that both drifters had measurable leeway. Leeway results are detailed in Table 4.1 for the Microstar drifter and in Table 4.2 for the Davis drifter. Leeway speed was calculated by regressing the drifter's speed through the water to the wind speed. The slope of the line represents the leeway speed of the drifter, units are normally represented as a percent of the wind speed. The leeway regression of each drifter is shown in Figure 4.12. The red line (and associated 95% confidence intervals, red dashed lines) are the best fit linear regression of the wind speed compared to drifter speed through the water. The green line (and associated 95% confidence intervals, green dashed lines) forces the y-intercept to zero. If leeway drift were due purely to wind forcing (i.e. discounting waves/stokes drift) if the wind is zero, the leeway should also be zero. The convention for leeway measurements in operational oceanography is to use the constrained value (Brushett et al. 2014a; Allen 2005) as it is applied to the wind values to calculate drift, therefore, the same process will be applied here in order to the values to be comparable. For the Microstar drifters, the unconstrained linear regression had a slope of less than 1% of the wind speed, but when constrained to a zero y-intercept had and leeway speed of 1.6% of the wind speed. The Davis drifters had similar results, with an unconstrained leeway speed of 1% and a constrained leeway speed of 1.6% of the wind speed. However, when the leeway was broken down into downwind and crosswind components, differences between the two drifter types was observed (Figure 4.13). The Microstar drifters had downwind leeway regressions, both constrained and unconstrained with negative slopes, indicating that the drifters tended to move in the upwind direction. This is opposite of the Davis drifters, which displayed 0.4% downwind leeway. Both drifter types showed the greatest leeway impacts in the crosswind direction. The Microstar drifters had a crosswind leeway of 1.4% of the wind speed unconstrained, and 0.7% when the regression was constrained through zero. The Davis drifters were even more impacted in the crosswind direction with an unconstrained crosswind leeway of 2% of the wind speed, and a constrained crosswind leeway of 1.2% of the wind speed. The angle of the crosswind component from the wind ranged from 10-50

degrees to the right of the wind. For comparison, other objects with similar crosswind leeway include objects with notably more freeboard, such as a 5.3m Panga boat with 2 people on board (1.5%), a 4.2m empty sunfish (0.48%), and a person in the water, face down, deceased (0.46%) (Allen et al. 2010; Brushett et al. 2014a).

4.5 Discussion

Since the leeway was calculated indirectly by removing the mean drifter velocities, the resultant leeway coefficients could contain drift from wind forcing, Stokes drift, or from residual motion in the surface currents such as those caused by local winds. In direct leeway measurements, both wind forcing and Stokes drift are captured in the leeway estimates making previous leeway coefficients comparable. However in this indirect method, the residual surface current flow is an additional force on the drifters and must be investigated. Surface Ekman drift caused by local winds could contribute to the residual motion of the drifters. (Poulain et al. 2000) found that Davis-type drifters leeway to the right of the wind caused by vertical velocity shear ($0.3-0.5\%$ of the wind speed). Differences in Ekman velocities at the surface compared to the mean depth of the drifter's drogue could contribute to vertical velocity shear.

Ekman (1905) quantitatively described the results of wind forcing on the surface layer of an ocean on a rotating earth. Assuming a steady, homogeneous flow with friction on a rotating Earth, the balance of forces reduces to the Coriolis and friction[1]:

$$-fv = A_z \frac{\partial^2 u}{\partial z^2} \quad \text{and} \quad fu = A_z \frac{\partial^2 v}{\partial z^2} \tag{4.2}$$

with surface boundary conditions

$$\tau_x = \rho A_z \frac{\partial u}{\partial z}|_{z=0} = 0 \quad \text{and} \quad \tau_y = \rho A_z \frac{\partial v}{\partial z}|_{z=0} = 0 \tag{4.3}$$

[1]Assuming the only movement is caused by wind. If the wind driven layer is sitting on a lower geostrophic layer, then $U = u_e + u_g$ and the pressure gradient force is included

Using complex variables so that $V = u + iv$, this system of equations can be reduced to second order homogeneous differential equation:

$$\frac{\partial^2 V}{\partial z^2} - a^2 V = 0 \quad \text{where} \quad a = \sqrt{\frac{if}{A_z}} \tag{4.4}$$

where f is the Coriolis parameter and A_z is the vertical eddy, or kinematic, viscosity. Assuming a solution in the form of $V = Ae^{az} + Be^{-az}$ and applying the boundary condition that as $z \to -\infty$, velocity goes to zero, the solution becomes:

$$V = \hat{A}e^{\frac{z}{D_e}}[cos(\frac{z}{D_e} + \phi) + isin(\frac{z}{D_e} + \phi)] \tag{4.5}$$

Here, D_e is the Ekman depth, defined as $D_e = \sqrt{\frac{2A_z}{f}}$ and ϕ is the angle of current to the wind. Applying the surface boundary conditions, equation 4.3, and for simplicity making the assumption that the wind is only zonal, the solution reduces to

$$u = V_o e^{\frac{z}{D_e}} cos(\frac{z}{D_e} + \frac{\pi}{4}) \tag{4.6}$$

$$v = V_o e^{\frac{z}{D_e}} sin(\frac{z}{D_e} + \frac{\pi}{4}) \tag{4.7}$$

where the complex velocity has been broken down into its real component (u) and imaginary component (v). The amplitude constant, V_o is $\frac{\tau_x}{\rho\sqrt{A_z f}}$. This result is the classical Ekman spiral with a surface velocity that is 45° to the right of the wind in the northern hemisphere, and a depth averaged transport that is 90° to the right. This result depends on the assumption that the vertical eddy viscosity is constant with depth. Although a somewhat unrealistic assumption, there have been observations of Ekman spirals in coastal regions (Chereskin 1995). However, we can use this relationship to estimate the vertical shear caused by the wind-driven layer on the drifters. The surface current caused by Ekman flow can be found by setting $z = 0$ in equations 4.6 and 4.7:

$$u(0) = V_o cos(\frac{\pi}{4}) \quad \text{and} \quad v(0) = V_o sin(\frac{\pi}{4}) \tag{4.8}$$

The profile of the Ekman layer currents will decay exponentially at a rate given by:

$$\sqrt{u^2(z) + v^2(z)} = V_o e^{\frac{z}{D_e}} \tag{4.9}$$

Using a value of $A_z = 2e^{-2}m^2/s$ and the mean wind velocity from WRF of $7.4m/s$ yields an $8.4cm/s$ surface Ekman current[2]. Using Eq. 4.9, the current at 2m depth is $7.6cm/s$, giving a vertical shear, $\frac{\partial V}{\partial z} = 0.004s^{-1}$. A vertical current shear could cause the Davis drifter to tilt in the direction of the surface Ekman flow, which would cause the heavy GPS unit on the top of the drifter to be off-center, increasing the angle of tilt. Once skewed, the drifter would have increased leeway due to increased freeboard. The Microstar drifter appears to be less influenced by shear due to the design, due to the large drogue being completely centered well below the waterline and the lack of a central inflexible rod. Vertical shear caused by the surface Ekman layer could explain some of the differences in the behavior of the two drifter types. The mean WRF 10-m wind stress and the resulting surface Ekman currents over the first 48 hours of the drift is shown in Figure 4.14. The red vectors represent the mean wind stress (N/m^2) over the first two days of the drift. The dominant direction is to the ENE, representing the Northeast Trade winds. The resulting Ekman surface current (black vectors) direction is to the northwest. This direction matches the anomalous movement of some of the Davis drifters, where drifters initially in the southern portion of the grid moved northwest, while their Microstar counterparts moved southwest. The surface Ekman transport to the northwest could also contribute to the large crosswind component of both drifter's leeway estimates.

Another possible cause for the large crosswind leeway could be from Stokes drift. Stokes drift is the net movement caused by a surface wave field in the direction of wave propagation (Stokes 1847) and can be thought of as the difference between the average wave-induced Lagrangian velocity from an Eulerian velocity (van den Bremer and Breivik 2018). Wave

[2]The vertical eddy viscosity was estimated using relationship between wind speed and latitude as described in Ekman (1905) and Pond and Pickard (1983)

induced Stokes drift can transport mass in the upper layer of the ocean, and has been observed both in the ocean (Smith 2006) and in the laboratory (Huang et al. 2011). Wave data for the timeframe of the drifter deployment was available from the Hawaiian Regional Wave Watch 3 (WW3) model (Chawla et al. 2013), as well as NOAA buoy 51002 to the southwest of the Island of Hawai'i. Significant wave height (in meters), wave period (in seconds), and wave direction (coming from - colors, going towards - vectors) for the dominant waves is shown in Figure 4.15. In the area of the drifter's release and subsequent travel, the dominant wave direction estimated from WW3 is generally to the northwest. A 48 hour time series comparison between WW3 in the vicinity of the NOAA buoy with observations taken from 51002 concur, flow direction is to the northwest. The net Stokes drift flow in the direction of wave travel can be estimated from

$$A^2 k^2 C_s e^{2kz} \tag{4.10}$$

where A is the wave amplitude, k is the radian wavenumber ($\frac{2\pi}{\lambda}$) and C_s is the phase speed (Pond and Pickard 1983). Using a mean Significant wave height of 2m, a mean peak period of 10s (taken from WW3 for the first 48 hours of the cluster) yields a net Stokes drift of approximately 2.5 cm/s. The direction of the Stokes drift matches the wind-driven surface Ekman current direction over the same time period. The combined sum of these two residual movements could have contributed to the large crosswind leeway component seen in both drifter types. However, the crosswind leeway of the Davis drifters exceeds that of the Mircostar drifters by 0.6% unconstrained and 0.5% constrained. The Davis drifters have been shown to be sensitive to vertical shear at a magnitude of up to 0.5% of the wind speed (Poulain et al. 2000) while the Microstars do not. While both appear to be susceptible to Stokes drift and Ekman currents, the shear over the surface Ekman layer could explain the increased crosswind leeway exhibited by the Davis drifters.

Given the estimates of downwind/crosswind leeway and the wind speed values recorded from WRF over the 48 hour period, the additional velocity imparted to the drifters from

the leeway forces can be estimated. By comparing these values which include wind forcing, Stokes drift and Ekman to the values calculated for Stokes drift and Ekman, the magnitude of wind-forced leeway can be estimated. The mean wind speed recorded by WRF over the 48 hour period was $7.4 \pm 1.8\, m/s$. For the Davis drifters, the downwind leeway (both unconstrained and constrained through zero) was 0.4% of the wind speed, or $2.9\, cm/s$. The dominant wind direction was the standard NE trade winds during the drift period. However, both Stokes drift from the dominant waves and surface Ekman forcing do not align with the downwind direction. This means that the additional velocity in the downwind direction most likely came from wind-induced leeway or from small impacts of sea wave induced Stokes drift. However, the crosswind leeway was 2.0% unconstrained, or $14.8\, cm/s$ and 1.2% constrained through zero or $8.8\, cm/s$. Both Stokes drift and Ekman align with the crosswind direction and their estimated sum ($10.9\, cm/s$) could explain the constrained crosswind leeway, and 73% of the unconstrained crosswind leeway. If you add in the estimated leeway caused by shear found earlier by Poulain et al. (2000) then this could completely explain the crosswind leeway of the unconstrained Davis drifter regression. This additional velocity could account for some of the difference between the modeled surface currents and the observed velocities measured from the drifters. The Microstar drifter's speeds appear to be less impacted by the wind. The crosswind leeway for the Microstars was the largest wind impact, with a crosswind leeway of 0.7% (constrained) which is equivalent to $5.2\, cm/s$ and 1.4% (unconstrained) or $10.4\, cm/s$. Both of these velocities could be explained by both Stokes drift and the surface Ekman current. However, their downwind leeway was negative, indicating an upwind direction of movement. The difference in designs above and below the water could result in the variation between the two drifter's downwind leeway. The Davis drifters have a larger above water signature and a mean drogue depth that is shallower than the Microstar design. In the second generation Davis drifter used in this study, the metal rod running through the middle of the drifter (including the GPS package attached to the top) extends 15cm above the waterline. There are also four foam floats attached to the end of each drogue's wing. The wings of the drogue extend down to 1 m depth from the

surface. This is contrary to the Microstar design where the drogue is centered at 1m depth but extends to 1.3m, with their above surface profile limited to one 8-in diameter sphere that sits directly on the surface. For the Microstar, an upwind movement indicates that the current velocity at the depth of the drogue is driving the drifter movement, as opposed to the near surface wind driven layer or wind forcing on the above water sphere.

Given the discussion above the large crosswind leeway seen in the drifters, particularly the Davis drifter, could be due to a push from the surface Ekman current, vertical shear caused by Ekman profile Stokes drift, or even a combination of all three. The strong crosswind leeway estimated in the Davis drifters may have led to the observed difference in the separation of the drifter pairs. However, due to a lack of direct measurements of drift through the water and tilt, the cause cannot be specified, only hypothesized. In addition, the error in the leeway measurements is large due to the indirect method of estimating speed through the water. However, the rate of separation of the pairs during the initial drift period does indicate that the buoys do not respond in the same manner to the net forces acting on the drifters. With such a large pair separation, the Davis drifters do not seem to act as non-slip drifters, which would follow a pattern created by the simulated drifters (Figure 4.9) and that was observed in the Microstar's pair separation (Figure 4.6). In addition, the Microstar's downwind leeway component was small (0.4%) and the direction was actually upwind, indicating that they are not driven by wind-induced leeway. The Davis drifter's downwind leeway does not align with the other forces and is most likely wind-induced.

Another source of error could be from the different positioning sources and associated latency. The Microstars were Iridium based, where the Davis drifters used Argos positioning. Both drifter types had bad/missing position data during the initial run that needed to be interpolated, however, the Microstars had less than 0.5% of the data that needed to be interpolated. The Davis drifters on the other hand had as much as 9.8% of the data that needed to be interpolated. In addition, Davis drifter positions would repeat if a new fix was not received, resulting in a zero velocity for that time block, then jump to the correct

position and the resulting velocity would jump to unrealistically large values (any value greater than 1.5 m/s was removed). The velocity values that were exactly equal to zero were also removed from the leeway regressions in the Davis drifters because of that reason, as well as the histogram of drifter velocities (Figure 4.11).

Since this experiment was conducted, the Davis drifters used in SAR have been updated, from a generation II to a generation III, iSLDMB, with iridium positioning. The newer Davis designs also sit lower in the water, with the instrument package just resting on the undisturbed sea surface. This will most likely change their drift characteristics. One recommendation from this study would be to repeat the cluster deployment with the new GenIII Davis drifters. Outfitting at least one drifter with a doppler current meter and accelerometer would allow for direct measurements of leeway to be obtained, as well as the tilt of the unit under the influence of vertical current shear in the surface Ekman layer. The switch to Iridium in the GenIII would also remove the discrepancies caused by the different positioning sources.

4.6 Conclusion

The cluster deployment conducted here showed that in this scenario, the Microstar and Davis drifters did not behave in the same way when subjected to the same forces. The Microstar drifter behaved more like a typical non-slip drifter, while the Davis drifter had large crosswind leeway that resulted in increased pair separation over the initial drift period. However, due to the indirect method of determining both drifter type's leeway and the lack of any measure of tilt on the drifters, the specific cause of the difference cannot be determined and further field testing is recommended to narrow the cause of the slip in the Davis drifters. The use of these drifters in operational oceanography and emergency response necessitates that they are non-slip, or the leeway is known. If the Davis drifter is being used as a non-slip drifter, a correction for the large crosswind leeway should be applied.

Microstar Unconstrained Linear Regression

	Slope (%)	Y (cm/s)	S_{yx} (cm/s)
Leeway Speed	0.9	5.3	17.8
DWL	-0.7	1.6	25
CWL	1.4	-5.7	25

Microstar Constrained Linear Regression

	Slope (%)	S_{yx} (cm/s)
Leeway Speed	1.6	17.8
DWL	-0.5	25
CWL	0.7	25

Table 4.1: Linear Regression of Leeway Speed, Downwind Leeway, and Crosswind Leeway for Microstar Drifters. For each component of leeway, the slope (in % of wind speed), the Y-intercept (in cm/s) and the Standard error (S_{yx}, in cm/s) is listed.

Davis Unconstrained Linear Regression

	Slope (%)	Y (cm/s)	S_{yx} (cm/s)
Leeway Speed	1.0	3.9	21.8
DWL	0.4	0	27
CWL	2.0	-5.6	25

Davis Constrained Linear Regression

	Slope (%)	S_{yx} (cm/s)
Leeway Speed	1.6	21.8
DWL	0.4	27
CWL	1.2	25

Table 4.2: Linear Regression of Leeway Speed, Downwind Leeway, and Crosswind Leeway for the Davis Drifters. For each component of leeway, the slope (in % of wind speed), the Y-intercept (in cm/s) and the Standard error (S_{yx}, in cm/s) is listed.

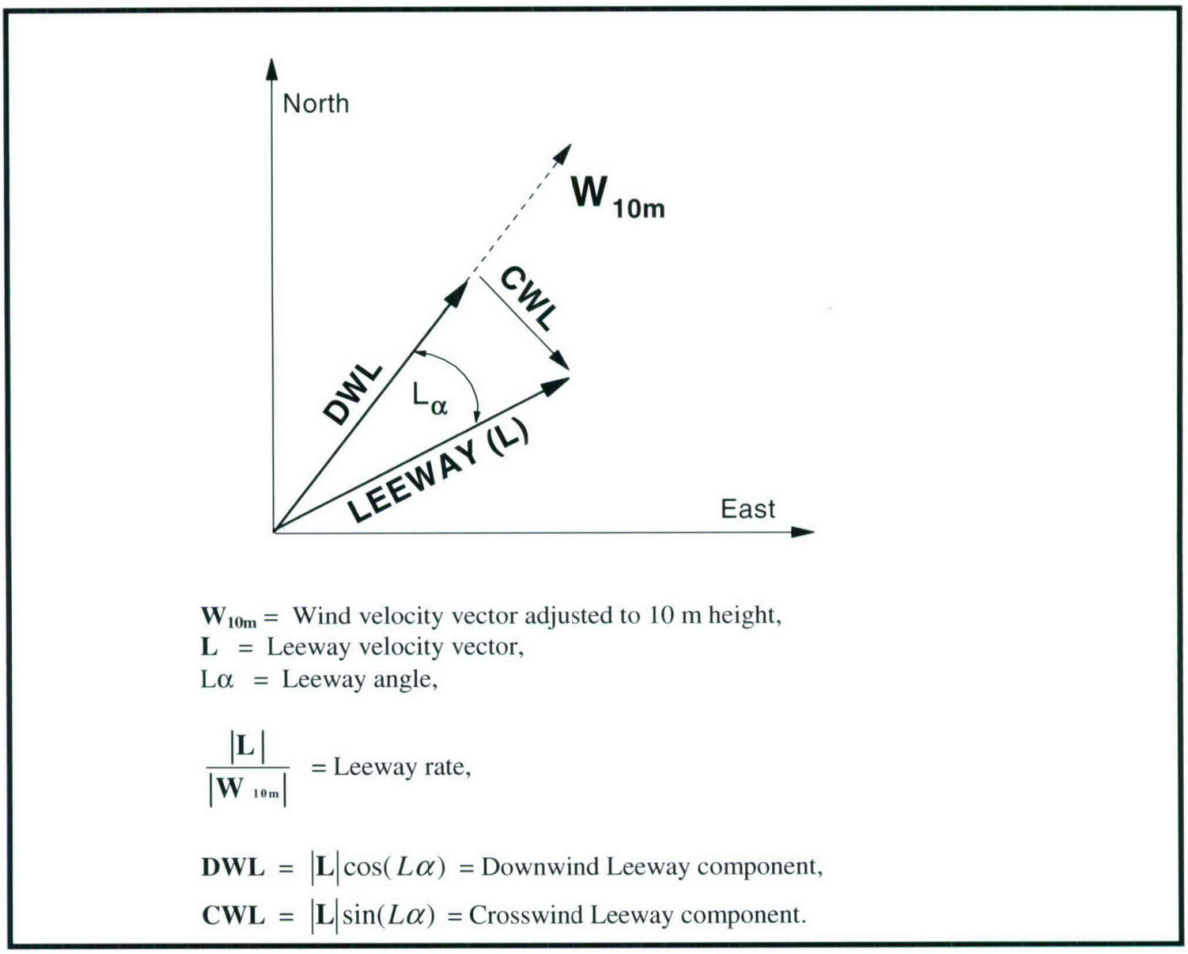

$\mathbf{W}_{10m}$ = Wind velocity vector adjusted to 10 m height,
$\mathbf{L}$ = Leeway velocity vector,
$L\alpha$ = Leeway angle,

$\frac{|\mathbf{L}|}{|\mathbf{W}_{10m}|}$ = Leeway rate,

DWL = $|\mathbf{L}|\cos(L\alpha)$ = Downwind Leeway component,
CWL = $|\mathbf{L}|\sin(L\alpha)$ = Crosswind Leeway component.

Figure 1-1. The relationship between the leeway speed and leeway angle and the downwind and crosswind components of leeway.

Figure 4.1: Schematic showing the components of leeway, from Allen (2005)

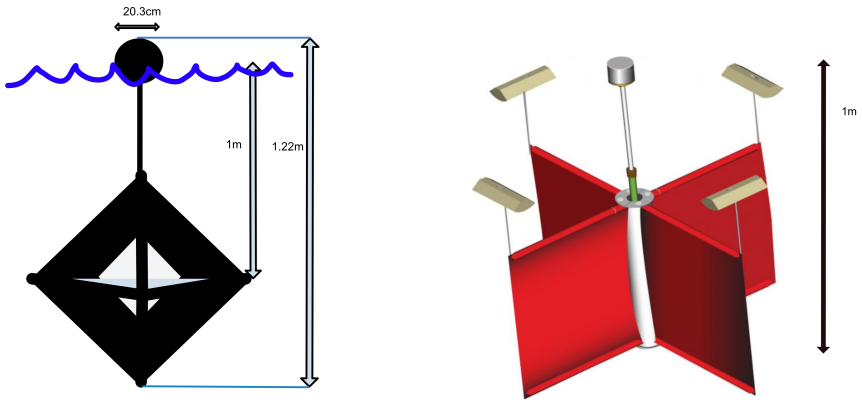

Figure 4.2: Microstar drifter design (left) compared to Davis drifter design (right)

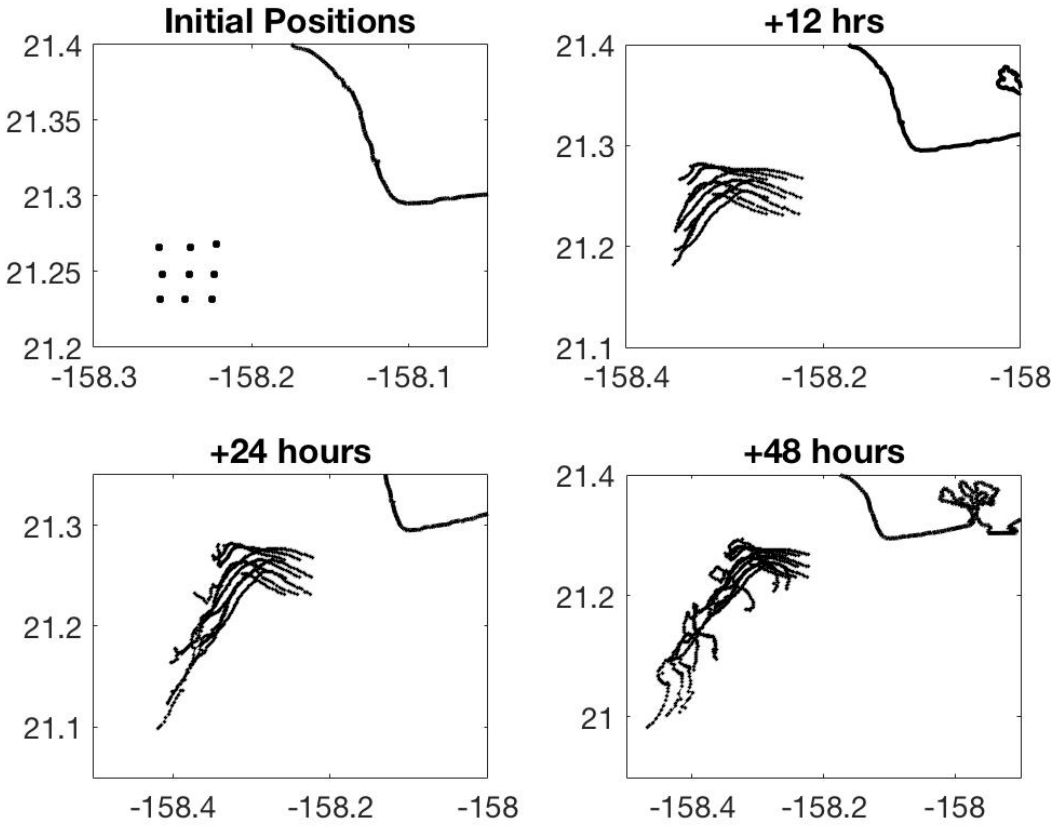

Figure 4.3: Initial deployment locations of the surface drifters, and the trajectory of each drifter 12, 24, and 48 hours after release. The drifter in the center of the cluster grid (position 5) was used as a reference for the dispersion of the group.

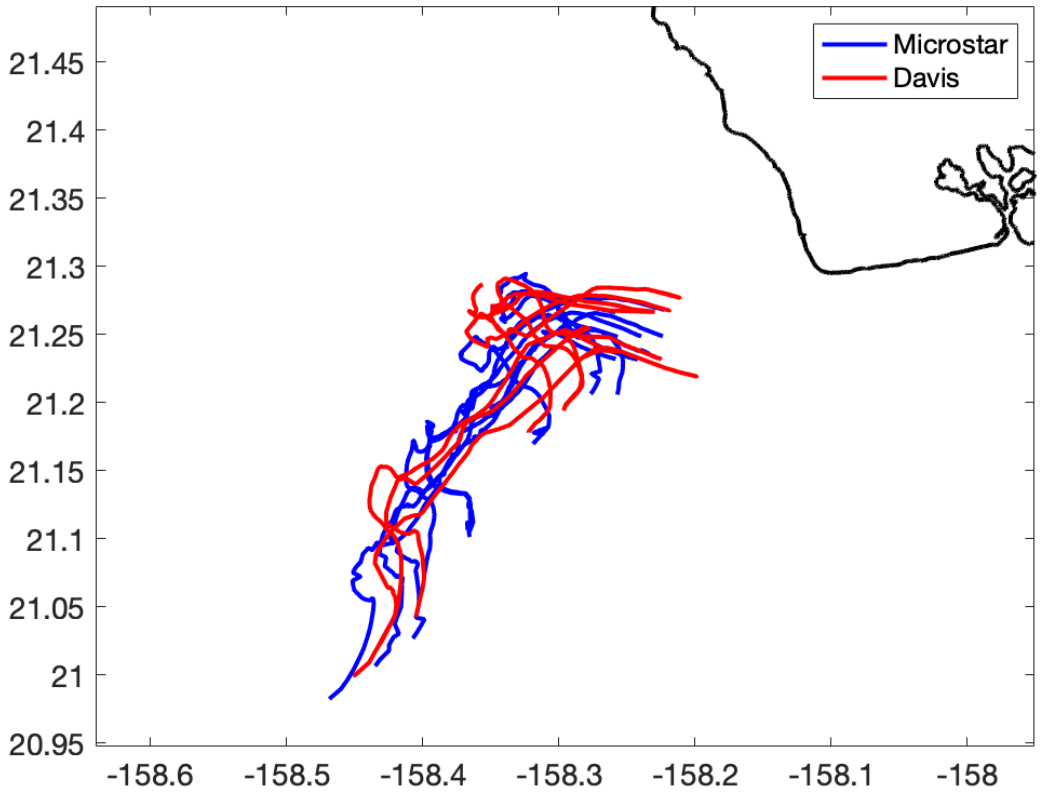

Figure 4.4: Trajectories of all drifters, both Microstars (blue lines) and Davis (red lines).

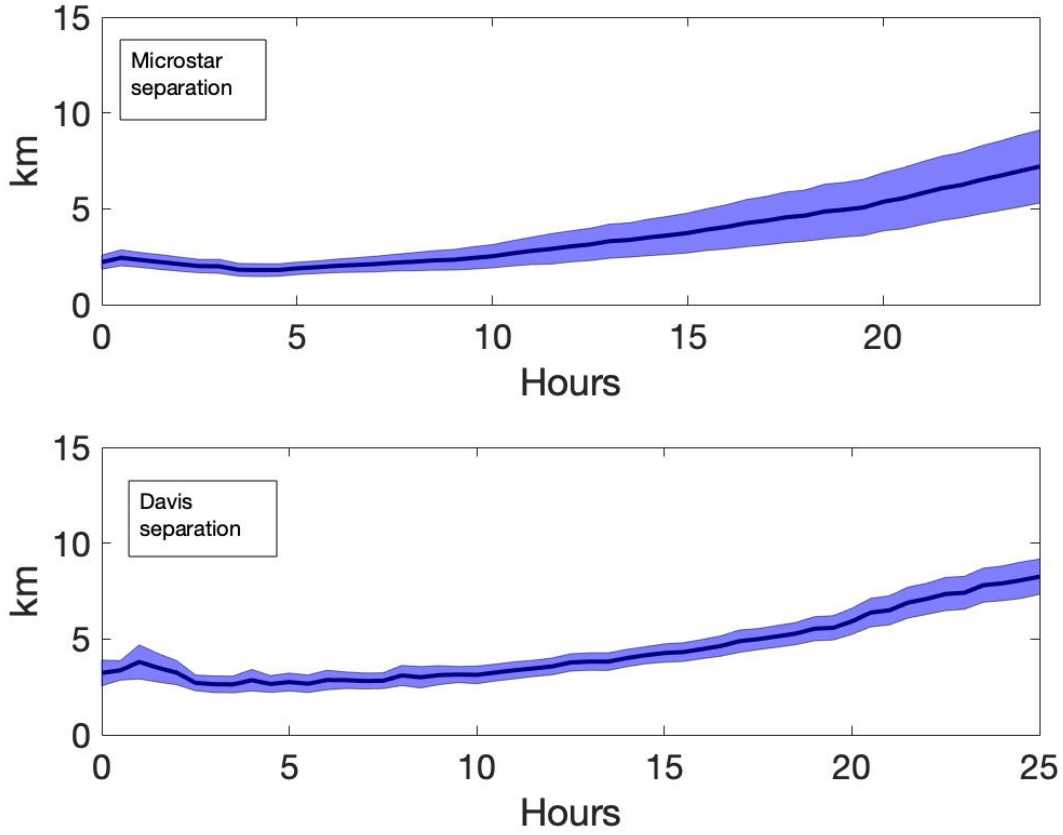

Figure 4.5: Average root mean square separation of of the cluster from the center position.

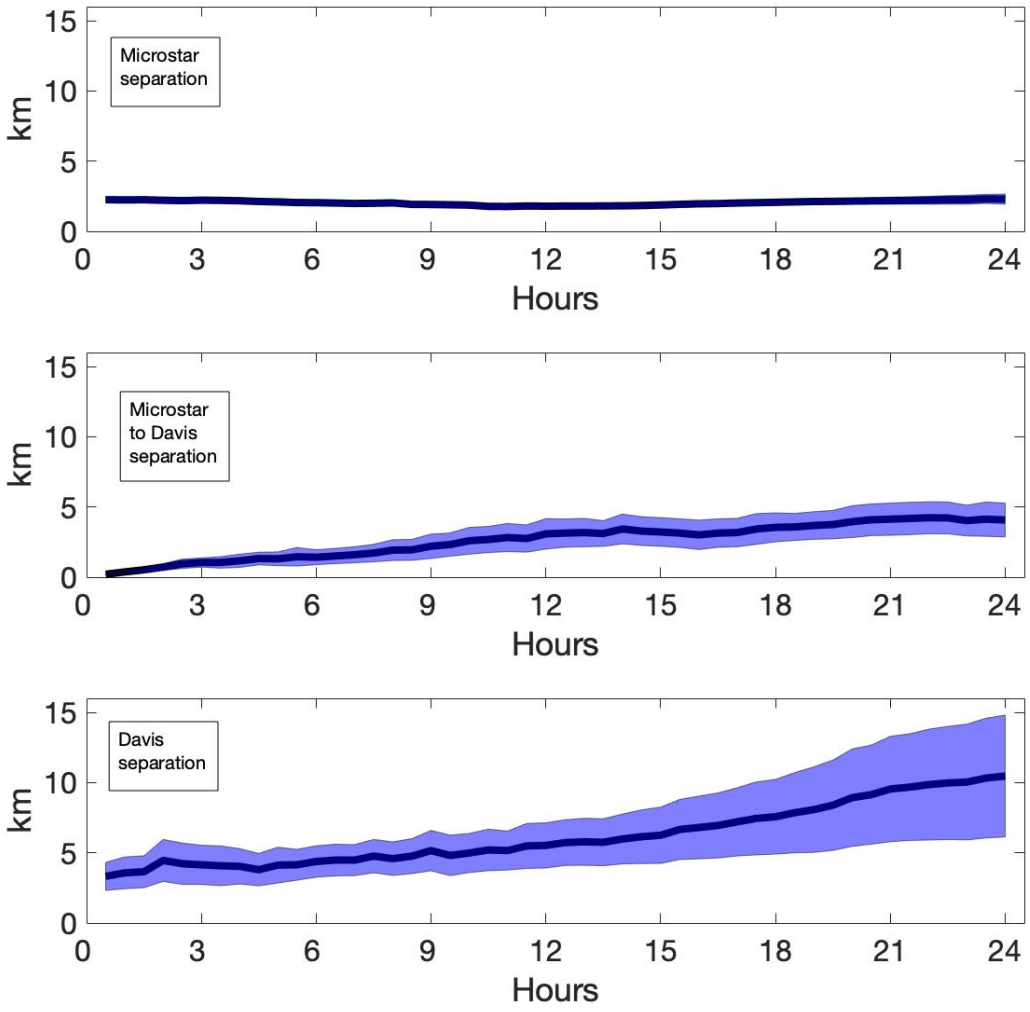

Figure 4.6: Average root mean square separation of drifter pairs in the cluster for each drifter type.

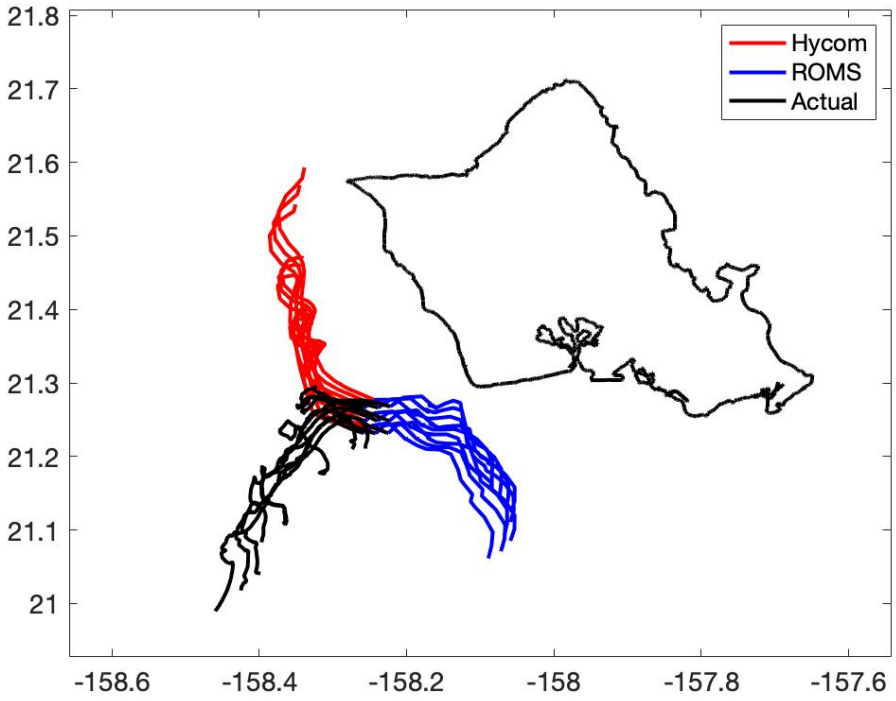

Figure 4.7: Predicted trajectories of the cluster for the first 48 hours using HYCOM (red) and Hawaii ROMS (blue) compared to the actual paths (black)

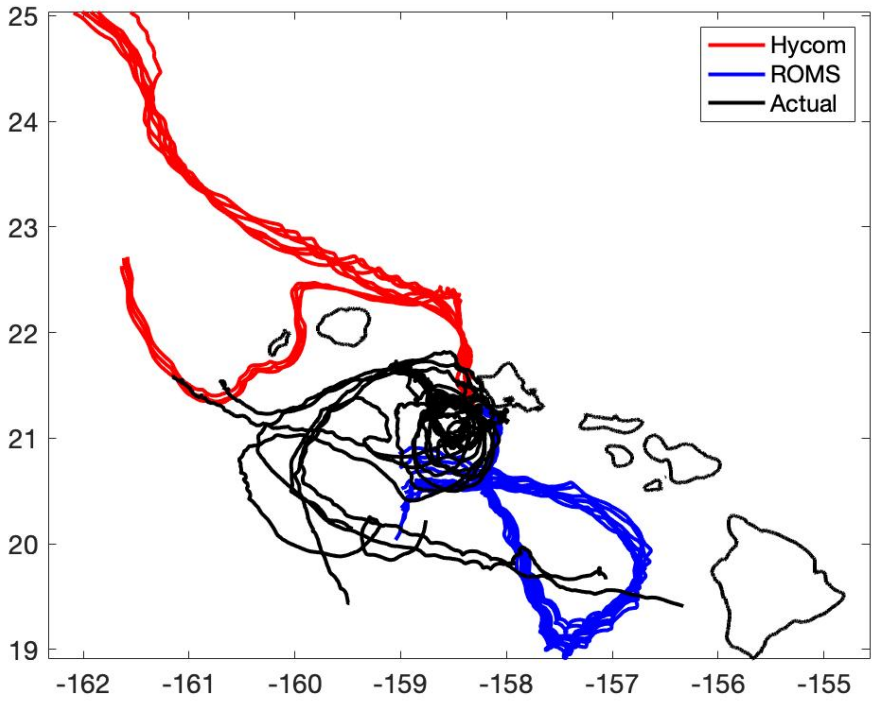

Figure 4.8: Predicted trajectories of the cluster for 30 days using HYCOM (red), Hawaii ROMS (blue) compared to the actual paths of the Microstar (black) drifters

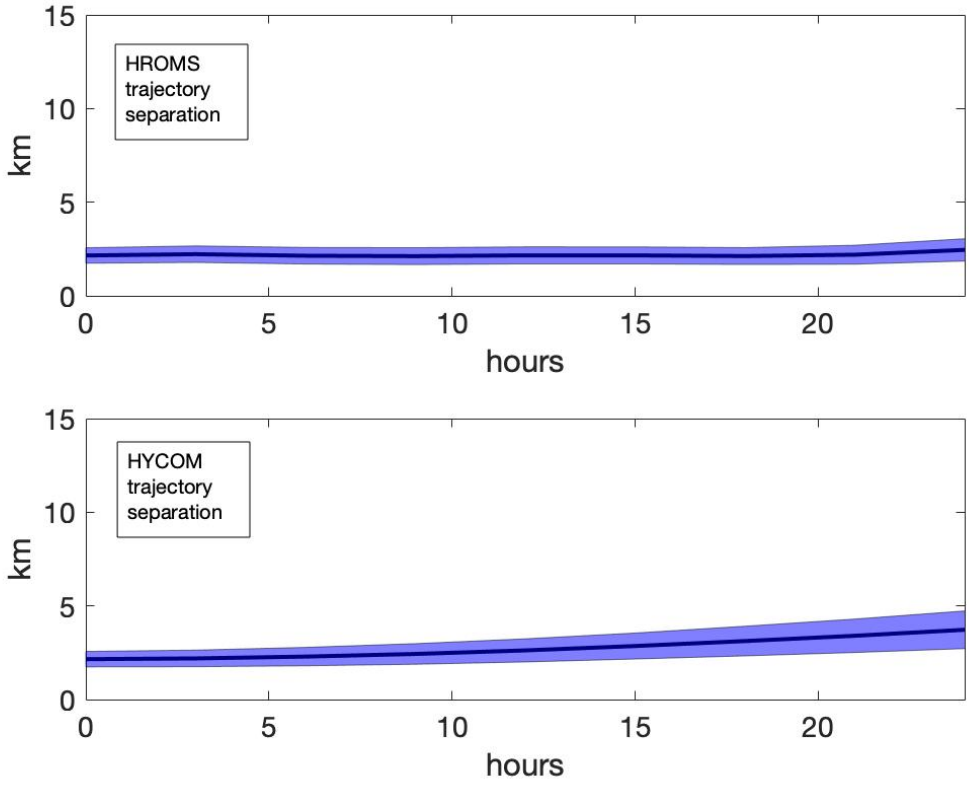

Figure 4.9: Separation of a predicted cluster using HROMS and HYCOM models

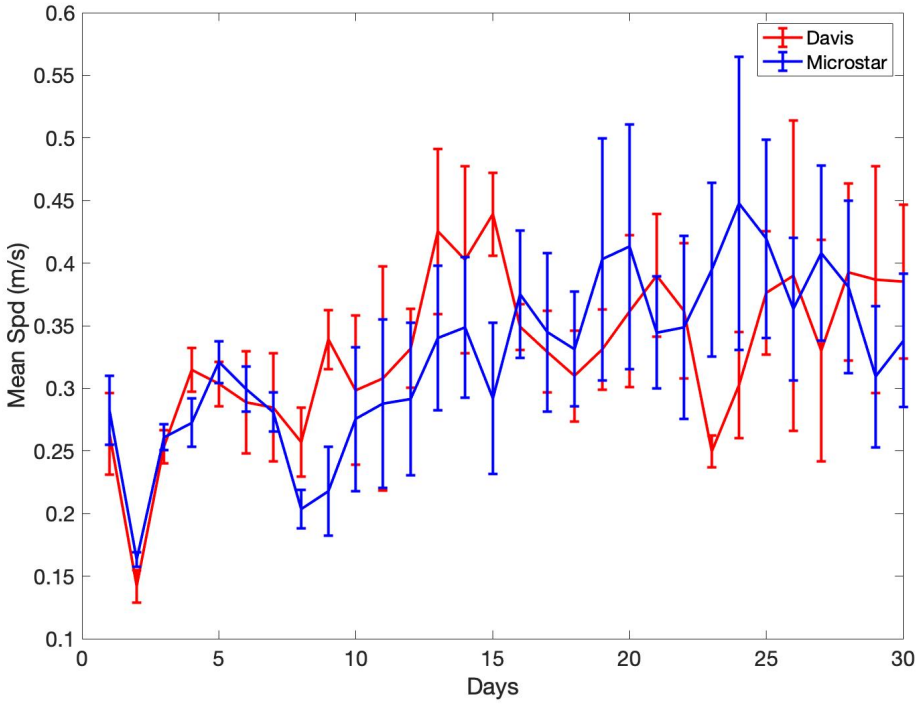

Figure 4.10: Mean daily speeds for each drifter over the first 30 days, Microstars (blue lines) and Davis (red lines) with standard errorbars.

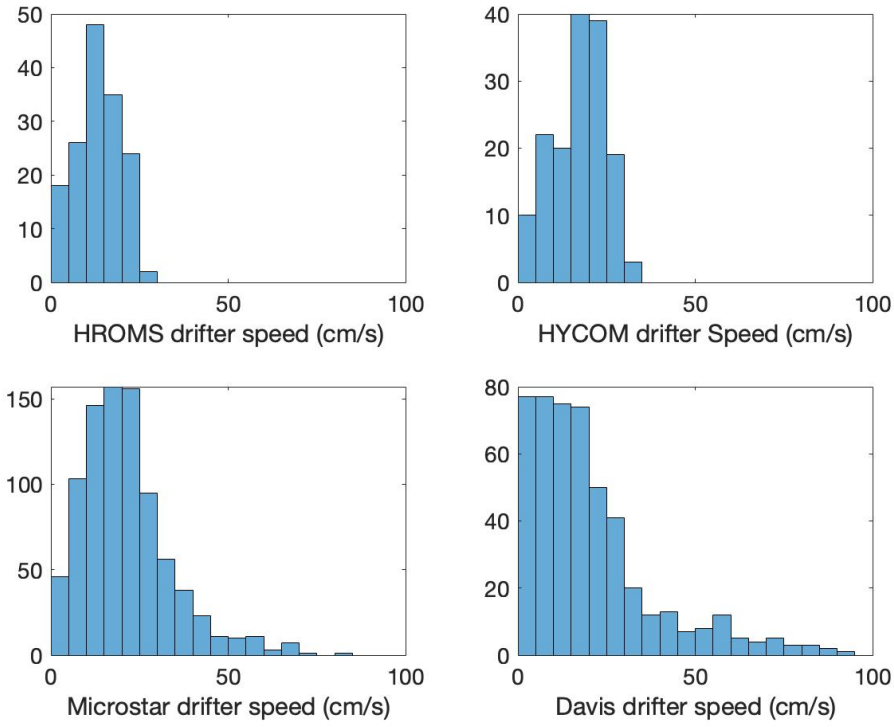

Figure 4.11: Histogram of drifter speeds over the first 48 hours

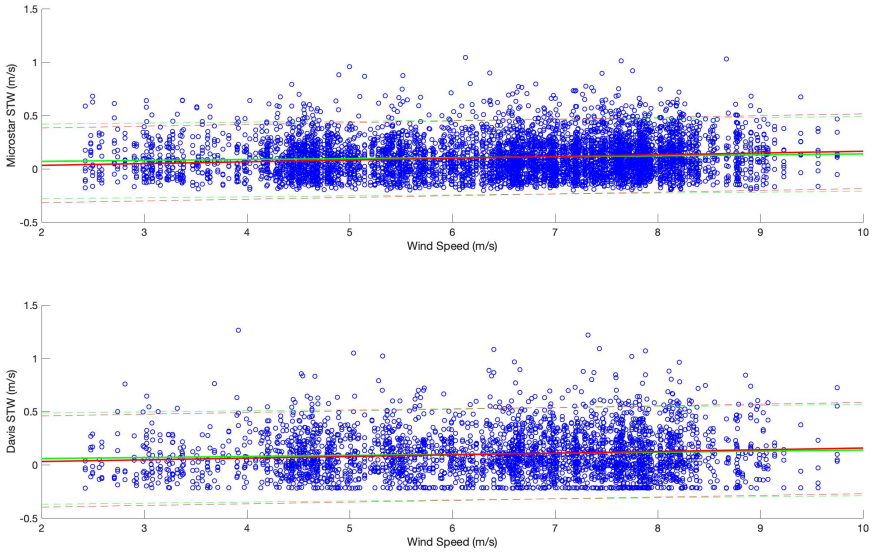

Figure 4.12: Leeway speed (m/s) compared with wind speeds at 10m (m/s) for both Microstars (top) and Davis (bottom) drifters. Green is the best fit linear regression, and red is the linear regression forced with a zero y-intercept. Dashed lines represent 95% confidence intervals

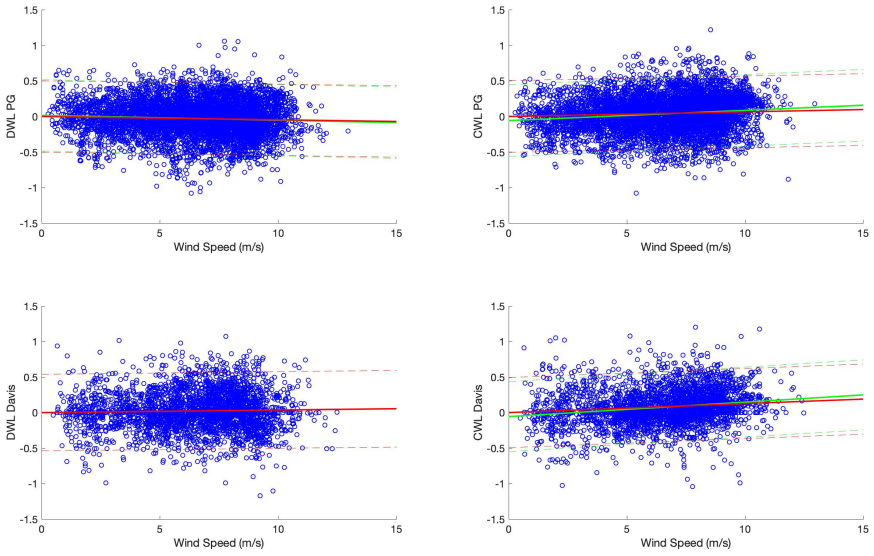

Figure 4.13: Downwind (left) and Crosswind (right) Leeway speed (m/s) compared with wind speeds at 10m (m/s) for both Microstars (top) and Davis (bottom) drifters. Green is the best fit linear regression, and red is the linear regression forced with a zero y-intercept. Dashed lines represent 95% confidence intervals

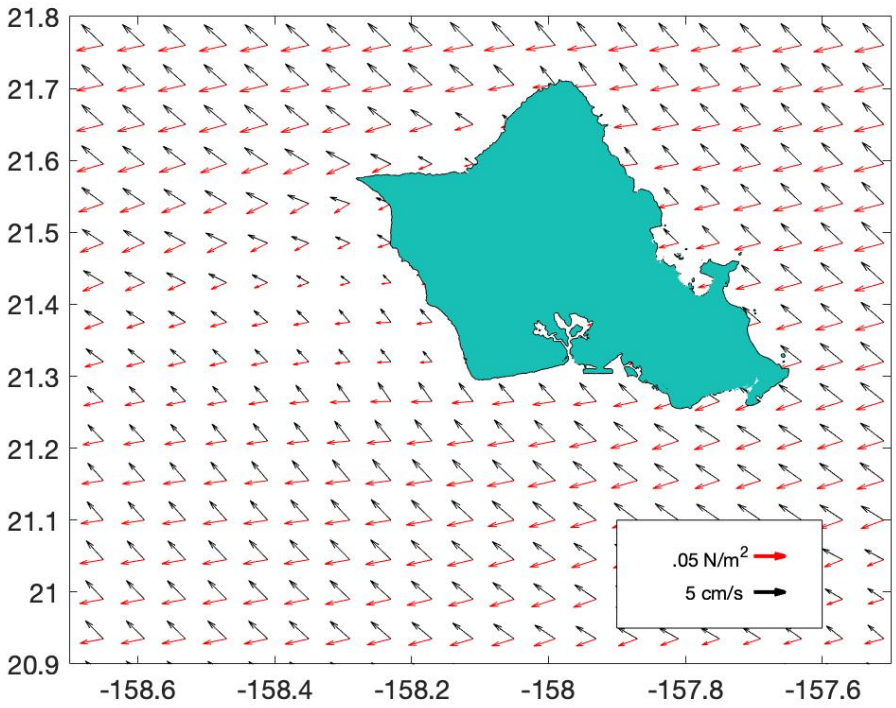

Figure 4.14: 48 hour Mean Ekman Surface currents (black vectors, in cm/s) calculated from WRF 10m surface wind stress (red vectors in N/m^2)

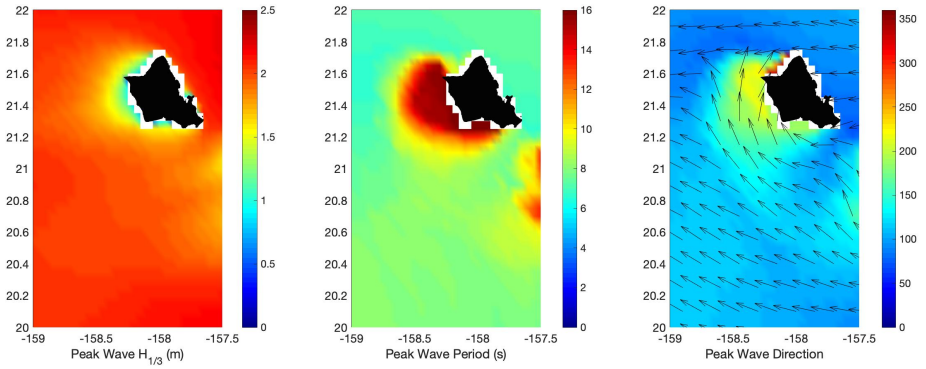

Figure 4.15: 48 hour mean wave height, period and direction for Peak waves

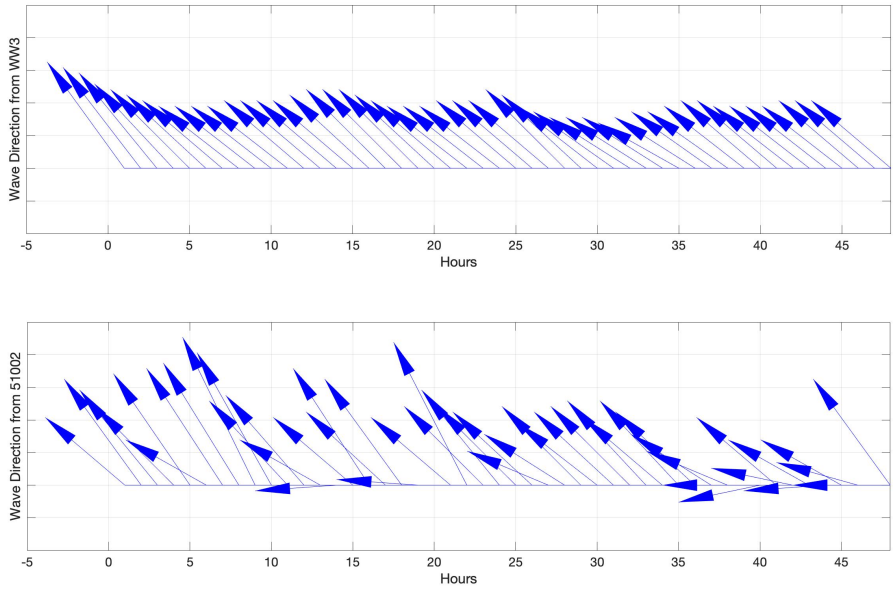

Figure 4.16: Top: Hourly wave direction taken from Wave Watch 3 in vicinity of buoy 51002. Bottom: Hourly wave direction from buoy 51002. Vectors are scaled by significant wave height.

Chapter 5

Discussion

The Hawaiian island chain is an ideal place to study lee eddies. Due to is unique position in the path of the North Equatorial Current and the Northeast trade winds, vortex formation downstream of the islands is common. So it is surprising that there are few, and no recent, comprehensive observational studies of these eddies. The last comprehensive study was in 1998, by Lumpkin. Since then, there has been a dramatic increase in available drifter data, now with $>$ 800 drifters having passed through the lee region of the islands. There are also long time records (20 years) of satellite data and the placement of high resolution High Frequency Radars on some of the islands.

There were 25 anticyclones found in the 27 years of drifter data, averaging out to just less than one anticyclone observed per year. The greatest number of anticyclones in one year was four, which happened in both 1994 and 1995. These years coincided with a large observational study, which could account for the increased numbers. Drifter coverage was not continuous in time and it is probable that many anticyclones passed quietly through without a drifter hitching a ride, meaning the anticyclones are most likely under sampled. The anticyclones observed with drifters were most likely to form in the summer months (July, August, September), and were least likely to form in the fall months (October, November, December). They had an average lifespan in the lee of the islands of 75 days, and the anticyclonic sector formed by the looping drifters extended past 170°W, a distance

of 1500 km downstream. The anticyclones followed a very narrow path centered to the south-southwest at 260°T. This lays out a clearly defined anticyclonic sector in the lee of the island of Hawai‘i. It is interesting to note that a similar cyclonic zone to the north of the islands was not visible in the drifter data, as was predicted by Lumpkin (1998). There were only three cyclones observed in the drifter data in the lee of the islands, and none of them travelled past 160°W. If this is truly representative of the dual vorticity zones created by the wake of Hawai‘i, then the anticyclonic zone is substantially stronger and dominates the lee dynamics.

One of the questions raised by Lumpkin (1998) after the last observational study was what the dominant forcing mechanism was for the anticyclones in the lee of Hawai‘i. An attempt was made to answer that question here by examining temporal and spatial patterns in the wind and sea level surrounding the island. Empirical Orthogonal Functions (EOFs) were used to pull out the dominant modes of variability in both the wind stress using QuikScat satellite data, and sea level anomalies, using AVISO satellite data. The dominant mode of variability in the wind stress was the annual fluctuations of the north east trade winds due to seasonal patterns. There was also a 50-day signal observable in the second wind stress EOF mode. The dominant mode of variability for the sea level anomaly was also a seasonal pattern with an annual signal. This signal was mostly confined to the lee of islands and had significant overlap with the observed anticyclonic sector from the drifters. With the annual peak in wind stress, this could indicate a potential for wind forcing of the anticyclones. The mean wind stress curl in the lee of Hawai‘i can spin up anticyclones and it has been shown by Yoshida et al. (2010) that anticyclones in the direct lee of Hawai‘i can be wind-induced at a 60-day frequency, but that it did not explain the anticyclones further to the west. In addition to the annual signal, there was also a 100-day signal observable in the sea level anomaly data. This signal was strongest downstream of the islands, and had two main sections. One area where the 100 day signal was strong was in a zonal path centered at 19.5°N, extending from 160° to 180°W. This area matches the

known location of the Hawaiian Lee Countercurrent (HLCC), that separates the cyclonic sector on the north, form the anticyclonic sector to the south. A second region where the signal was strong was a south-southwest region running from 160° to 175°W, angled at 260°T. This section of the 100 day signal matches the anticyclonic sector very well. The 100-day signal was found to be uncorrelated to the 50-day signal in the wind stress. With the anticyclonic signature in the both the annual and 100-day signals, there could be multiple forcing mechanisms at play. The wind stress would explain the annual signature, but it cannot explain the 100-day signal. Unfortunately, there is very little observational data for ocean current structure and variability off of the southern region of Hawai'i. In order to investigate the potential of shear instability from the NEC separation's off of the island as a potential forcing mechanism, better quality data is needed. The whole region surrounding the island of Hawai'i is observationally sparse. This is unfortunate because the island is subject to interesting dynamics. The current flow along the leeward coast often reverses direction (Chapter 2) and when speaking with local boaters and fisherman near South Point, Hawai'i, they describe the regional waters as difficult and unpredictable. One recommendation from this dissertation would be to complete an observational study along the southern and leeward coasts of the island of Hawai'i. This is an important region economically, for fishing and tourism, but our knowledge of the coastal dynamics is lacking. What is the current structure off of South Point? Is the current fast enough, and is the shear line strong enough to generate this anticyclonic eddies? And what happens to the Hawaii Lee Current along the western shores of Hawai'i? Mean currents from the drifters show that it disappears during anticyclones. This would mean it is most likely stronger during cyclones. And does it exist when there are no vortices?

Most of the research on lee eddies has been conducted on the vortices of the largest island. But we know that these eddies also form in the lee of the smaller islands. Due to the presence of high frequency radar (HFR) installed along the leeward coast of the island, Oahu presented an opportunity to study the lee wakes in more detail. A year long drifter and

HFR study was conducted in the western waters of Oahu. There were 75 drifters deployed off the western coast of Oahu and the HFR provided almost near-continuous high resolution spatial current vectors at hourly intervals. During the course of the year, there were eight cyclones and five anticyclones observed in Oahu's lee. Looking at the eddies formed only during the NE trade winds, the cyclones and anticyclones split into distinct sectors, with a cyclonic zone to the north, and an anticyclonic zone to the south, as observed in Chapter 2, for Hawai'i. Although previously modeled, this study is the first to map out these dual zones using observations for Oahu. By looking at the vorticity balance in the ocean during these events, these vortices are most likely wind-driven. However, not all of the vortices in the lee of Oahu were wind-induced. Three of the cyclones formed during Kona winds (trade wind reversals) when the wind forcing was removed. These cyclones must have been formed by another source of vorticity into the ocean, such from changes in topography (only for very coastal regions) or input of relative vorticity by shear or curvature. This breakdown of vorticity inputs using the HFR currents is what was lacking in the previous study on the island of Hawai'i.

There were three varieties of drifters used in this dissertation research. The first type, used to investigate the anticyclones in the lee of Hawai'i were from the Global Drifter Program-Surface Velocity Program (SVP) database. The errors in these buoys have been well studied and the data was validated in Lumpkin and Pazos (2007). However, the two drifters used to study the smaller vortices in the lee of Oahu were a Davis-style drifter by MetOcean, and a Microstar drifter by PacificGyre. Deployed together in a cluster, differences in their behavior were noted. A detailed comparison of their behavior was completed in Chapter 4. Over the course of the initial drift, both drifters moved with the mean flow. However, looking at the separation in the cluster revealed that the Davis drifters quickly separated from their Microstar pair were bumped to the northwest. A estimate of each drifter's leeway revealed differences in their response to wind and ocean forcing. While the Microstars behaved more closely to a non-slip drifter, the Davis drifters had downwind

leeway that was around 0.4% of the wind speed, and had a crosswind leeway that was 0.5% larger than the Microstars. The Microstar drifter's crosswind leeway could be explained by the local Ekman surface currents and Stokes drift from the dominant waves, both relics of the indirect leeway estimation method. However, the Davis drifters additional leeway meant a larger response to those forces, or additional input from wind or current shear. With recent updates to the Davis drifter used in search and rescue, this study should be repeated with the newer generation drifters. If possible, outfitting with an accelerometer or pitch/roll meter would allow wave impacts to be removed.

One of the difficulties in conducting operational studies in the Hawaiian region is the low density of oceanographic observations due to the small land to water ratio. This has implications outside of academic interests. In particular, search and rescue operations rely on accurate wind and ocean data/forecasts in order to plan search responses. After observing the lack of data available for parts of this study, I wanted to know what that data availability was for search and rescue and if it had an impact on search probability size. This lead to Appendix A, a look at the data available for search and rescue in Pacific waters. It turns out that most of the search and rescue cases in the last 16 years are not covered by anything more than the global scale wind and ocean models. Not only would increased observations improve our scientific understanding of Hawaiian waters, but strategically placed observations could improve search and rescue.

Appendix

EOF Analysis Review

A.1 Definition

The Empirical Orthogonal Function (EOF), also called Principal Component Analysis (PCA) is a statistical tool used to explain the variance in a data set. This method can be used to find both temporal and spatial patterns that represent variance in a field, such as sea surface height, winds, etc. EOF analysis can be used only to find standing wave patterns in spatially gridded data sets (Emery and Thomson 2004). In order to find propagating modes, a complex EOF should be used in the frequency domain (Emery and Thomson 2004).

A.2 Background

Although used earlier, Principle Component Analysis was brought into mainstream use by Hotelling (1933), however it wasn't until 1956 that the term EOF was coined by Lorenz (1956) and first used in geophysical sciences for statistical weather prediction (Emery and Thomson 2004). Since then, it has grown in use as a tool to analyze variation in spatially gridded data sets. Even though there is no direct relationship between the EOF modes and scientific processes, it can be a useful way analyze the variance in a data set. For this reason, EOF analysis is particularly useful with the recent addition of gridded satellite time series data sets.

A.3 Methodology

Here, two different EOF methodologies will be discussed. The first is the calculation of EOFs and principle components by calculation of the eigenvector and eigenvalues of the covariance matrix. The second method discussed is singular value decomposition (SVD) of the data matrix.

Since the EOF is used on spatially gridded time-series of a variable (such as temperature, sea surface height, etc.) it can be represented as a function:

$$A(\phi, \theta, t) \tag{A.1}$$

where A is the variable or data, ϕ is the longitude, θ is the latitude, and t is the time. The first step is to prepare the data for computation of the EOF. To reduce computational stress, it is efficient to combine the latitude and longitude dependence into one variable representing spatial coordinates, and transform from a three dimensional matrix to a two dimensional matrix. This creates a variable that is a function of space and time, $A(s,t)$. Next, the mean must be removed from the spatial data set. This can be done by removing the time average of the data at each spatial grid point, leaving the anomaly field:

$$A'(s,t) = A(s,t) - \overline{A}(s) \tag{A.2}$$

where $A'(s,t)$ is the anomaly field, $A(s,t)$ is the original 2D data set, and $\overline{A}(s)$ is the time averaged data at each grid point. If the data field is not a scalar, but a vector, such as wind speeds, or ocean currents, the same preparatory methods can be used:

$$U'(s,t) = U(s,t) - \overline{U}(s) \qquad and \qquad V'(s,t) = V(s,t) - \overline{V}(s) \tag{A.3}$$

where $U'(s,t)$ is the anomaly field of zonal wind, $U(s,t)$ is the original 2D zonal wind data set, and $\overline{U}(s)$ is the time averaged data at each grid point. The same is true for meridional wind, V. These can then be combined into a complex number $W = u' + iv'$.

A.3.1 Eigenspace Method

The computation of the EOF begins with the calculation of the covariance matrix of the data. Covariance represents how much two variables change together about a common mean (Emery and Thomson 2004). A positive covariance demonstrates that two variables increase or decrease together, where a negative covariance represents one variable increasing and the other decreasing.

$$C = \frac{1}{n-1} A'^T A' \qquad or \qquad C = \frac{1}{n-1} W'^T W' \tag{A.4}$$

For a square matrix, we can now solve the eigenvalue problem, $Ce = \lambda e$ where C is the covariance matrix, e is the eigenvectors and λ are the eigenvalues as follows:

$$Ce - \lambda e = 0 \tag{A.5}$$

$$CIe - \lambda Ie = 0 \tag{A.6}$$

$$(C - \lambda I)e = 0 \tag{A.7}$$

which is the characteristic equation and I is the unity matrix. A non-trivial solution requires that

$$det(C - \lambda I)e = 0 \tag{A.8}$$

We can then solve for e, the eigenvectors (the EOFs) and for λ, the eigenvalues (the principle components or time-series amplitudes of each EOF). The percentage variance represented by each mode is

$$V_i = \frac{\lambda_i}{\sum_{i=1}^{n} \lambda_i} * 100 \tag{A.9}$$

Note: If a complex dataset, W is used it will create a covariance matrix of dimension NxN that is Hermitian. A Hermitian matrix is defined as a matrix that is equal to its conjugate transpose. The eigenvalues of a Hermitian matrix are real and N orthogonal eigenvectors

exist (Hardy and Walton 1978). Solving the eigenvalue problem yields real eigenvalues and complex eigenvectors. The eigenvectors of each mode are of dimension N, complex, with the magnitude detailing speed (such as wind speed or current magnitude) and the argument detailing direction or phase, which create a set of vectors for each geographic position.

A.3.2 SVD Method

Singular Value Decomposition is a method of breaking down a matrix into the product of three matrices, and therefore picking a different coordinate system in terms of maximum variance. If we begin with a mxn matrix, A, where m is time and n is space, we can factor A using SVD into:

$$A = USV^T \tag{A.10}$$

Here, U is an orthogonal mxm matrix, V is an orthogonal nxn matrix, and S is an mxn diagonal matrix (Williams 2014). Matrix S is the weighting for each mode, from greatest to least, along the diagonal. This can also be thought of as the variance represented by each mode. For each mode S_i, the associated components of U and V are column i of U and row i of V^T or column i of V. U is m points in time, so column i of U is the amplitude of mode i and are the Principle Components (PCs) for that mode. V is n points in space for each column, and this is the EOF for that mode.

A.4 Complex EOF

EOF analysis can only detect standing waves or oscillations. Because of this, propagating features in a data set show up as two modes, with each mode representing a phase of the propagation. In order to represent propagating features in one mode, a complex EOF is used. A complex EOF uses a Hilbert transformation to represent the data in the frequency domain before computation of the covariance matrix and eigenvalues and eigenvectors.

Mathematically, a propagating feature can be represented as:

$$A_{x,t} = \sum_{\omega} [\underbrace{b_x(\omega)cos(\omega t) + c_x(\omega)sin(\omega t)}\, a_{x,k}] + i[\underbrace{c_x(\omega)cos(\omega t) - b_x(\omega)sin(\omega t)}\, \hat{a}_{x,k}] \quad \text{(A.11)}$$

where $A_{x,t} = a_{x,k} + i\hat{a}_{x,k}$ is the representation of the data using a Hilbert transformation. Here, $a_{x,k}$ is the original data and $\hat{a}_{x,k}$ is the Hilbert transform. The Hilbert transform does not filter the data, the amplitudes are the same, but it advances the phase by $\pi/2$. From here, the procedure is nearly identical to the normal EOF calculation. With the complex data $A_{x,t}$, find the covariance matrix, C, and then find the eigenvalues λ_i, and the complex eigenvectors, e. From these three variables, distinct modes can be defined as $B_i(x)$ with principle components $P_i(t)$, where i is the mode number.

A.5 Reconstruction of Data

One of the primary benefits of using EOF analysis is that can remove noise from a data set. After breaking down a data set into its EOF modes and Principle Components and identifying the dominant modes, the data can be "reconstructed" using only those modes. This eliminates noise in the data from higher order modes. The data can be reconstructed with:

$$Data = \sum_{i=1}^{n} PC_i * EOF_i \quad \text{(A.12)}$$

where there are n EOF modes and PC is the principle components for each mode. If after analysis of the EOF results, the main dynamics can be represented from the first three modes, the cleaned data can be represented by the sum of the first three modes:

$$NewData = PC_1 * EOF_1 + PC_2 * EOF_2 + PC_3 * EOF_3 \quad \text{(A.13)}$$

Appendix

Search and Rescue Applications: On the Need to Improve Ocean Observing Data Systems in Offshore or Remote Locations

Abstract

Search and rescue (SAR) in remote maritime locations is a difficult mission. One of the limitations in these isolated regions is the low density of available oceanographic data for model validation. In order to examine the state of remote search and rescue a review of maritime search theory and advances was conducted. This included basic drift theory, leeway, available environmental data, and the current methods used by the United States Coast Guard for SAR operations. In particular the U.S. Coast Guard's fourteenth district's SAR case history was examined and it was found that 60% *of SAR cases fall outside of areas that have high-resolution wind and current data, with only global scale model forecasts available. In addition,* 2% *of cases occurred in offshore waters (>* 12*nm from land) and exceeded* 36 *hours in asset response time. Three SAR simulations were run off the coast of Oahu, Hawaii using the same wind data, but different surface current models. These simulations had extremely large (up to 12,000 km*^{2}*) search areas, highlighting the need for solutions that narrow these expected areas.*

A.1 Introduction

The United States Coast Guard (USCG) is responsible for more than 21.3 million square nautical miles of ocean and oversees 11 mission areas including aids to navigation, living marine resources, law enforcement and search and rescue. In 2017, the USCG responded to 16,000 search and rescue (SAR) cases and saved over 4,000 lives. Although most SAR cases are short lived and do not require an extensive search, the cases that do extend over multiple days and necessitate extensive asset allocations are quite expensive. These cases generally have a low probability of successfully finding missing persons alive. During a typical SAR case, nowcast and forecasted oceanographic and meteorological data from numerical models are used to predict the drift pattern of the lost object or person using leeway calculations. In many areas there are limited observational oceanographic datasets available to verify drift prediction from the fields, which can reduce the probability of success. A prime example is the Coast Guard's fourteenth district, which is responsible for the Hawaiian Islands, America Samoa, Guam, the Northern Mariana Islands, and the Republic of the Marshall Islands as well as the high seas in between. Many of these regions are isolated and lack observational current data for model validation. In addition, the island regime creates unique issues that are not common in mainland region cases such as the large ocean distance between population centers, crossing between islands can cover deep, exposed waters and may be done in small craft (Brushett et al. 2014b). Here, we review the literature on SAR in maritime environments and examine SAR statistics in the USCG's fourteenth district to identify gaps in our current oceanographic data coverage. Then, using current methods and datasets available to USCG SAR, we run three example case studies in the Hawaiian Islands.

A.2 Search and Rescue Fundamentals

Objects lost at sea are subject to forcing from ocean currents, winds and waves. For SAR purposes, an object drifting in the ocean subject only to a current V_c is expected to drift

at the same speed as and in the direction of V_c. However, the addition of wind complicates the equations. Due to the complex nature of wind forcing on the ocean surface and that the area exposed to the wind is different for each search object, a drift prediction requires more than just knowledge of the surface current speed. Total drift is predicted from leeway, defined as *the motion of the object induced by the 10-m reference height wind and surface waves relative to the ocean current* in Breivik et al. (2013) as well as Allen and Plourde (1999). Using the definitions put forth in Allen (2005), wind forcing is treated as a vector with a direction and magnitude. Leeway speed is the velocity given to a drifting object from the wind, relative to the ambient currents. It is usually noted as a percentage of the wind speed. Leeway angle represents the angular offset from the downwind direction. This angle, when combined with the downwind component leeway, and the crosswind component, creates the full leeway vector. A thorough discussion of these principles is given in many previous key publications (Allen 2005; Hackett et al. 2006; Breivik et al. 2013; Breivik and Allen 2008).

The leeway of an object does not just represent wind forcing on a drifting object. As detailed in Brushett et al. (2014b); Hodgins and Hodgins (1998), the total drift of an object is the sum of the drift caused by the currents and the drift caused by leeway. However, inside both of these sources of drift are subcategories. The drift caused by currents can be thought of as the superposition of the drift caused by surface currents and the drift caused by Stokes drift. The drift caused by leeway can similarly be broken down into a component caused by wind upon the surface of the ocean and the impact of waves. Leeway estimates therefore include impacts from stokes drift, waves, and wind. It has been shown by Hodgins and Hodgins (1998); Breivik and Allen (2008) that leeway impacts caused by wave motion can be ignored for objects smaller than one half of the wavelength of the average wave. The leeway caused by the stokes drift from local wind driven sea waves will predominantly be in the downwind direction. Leeway caused by stokes drift from swell could occur in any direction and would therefore be wrapped into both the downwind and crosswind leeway estimates.

Leeway is normally calculated using either the direct method by measuring drift through water using attached current meters and anemometers or the indirect method of subtracting the estimate of current drift from the total drift (Allen and Plourde 1999). For different drift objects such as a person in the water, a liferaft, or a 36' sailboat, leeway parameters specific to each object need to be measured and recorded for use during SAR operations. As of this publication date there are 89 different leeway categories available with more being tested every year. New advancements in leeway calculation have shown that it is possible to create a model of leeway drift using the balance of hydrodynamic and aerodynamic forces. This was conducted by Di Maio et al. (2016) on a person in the water, with the modeled leeway performing better than the statistical approach described above. If this model proves accurate with other objects, it could reduce the need for direct measurement of leeway parameters.

A.3 Oceanographic Data

Observational data can be used during search and rescue operations in three main ways: a) validation of numerical model output, b) used directly or through a short term predictive model to predict drift, or c) through assimilation into ocean models that are then used to predict drift.

A.3.1 Surface drifting buoys

Surface drifting buoys are commonly used to validate ocean currents during SAR operations (Breivik et al. 2013). These units are deployed in the area of interest and their drift is compared to available numerical model outputs, which aide in the placement of search patterns used by response assets. A thorough discussion of the use of surface drifting buoys for SAR is provided in Berkson et al. (2019); Wilkin et al. (2017); Roarty et al. (2018) and Roarty et al. (2016).

A.3.2 High Frequency Radar

The availability of High Frequency (HF) Radar surface current data has expanded over the last twenty years. Integrated HF radar networks are available for operational oceanographic use in the United States (IOOS, discussed below), Austrailia (Austrailian Coastal Ocean Radar Network, ACORN), the Mediterranean Sea (Tracking Oil Spill and Coastal Awareness, TOSCA) and since 2017, as a global HF radar network (http://global-hfradar.org/). The U.S. Integrated Ocean Observing System (IOOS), through its academic and state partners, is one of the main providers of HF radar data for SAR operations (Harlan et al. 2011) in the United States. Work by Bellomo et al. (2015) showed that the use of HF radar data in SAR and oil tracking operations reduced position error and search range by up to a factor of 5. In addition to the real-time surface currents which can be used for model validation, in some regions the data is used to produce forecast fields from a program called the Short Term Predictive System (STPS) (Harlan et al. 2011). As discussed by Ullman et al. (2003), the STPS, developed and run by the University of Connecticut with support from US IOOS, predicts the surface currents up to 25 hours in advance by breaking them down into two components: a tidal-driven flow, and a non-tidal driven flow (2003). The tidal driven flow is predicted using harmonic analysis of one month of HF radar data, the non-tidal flow is predicted using Gauss-Markov estimation (Ullman et al. 2003). This STPS is presently available for SAR use for the entire West Coast where there is HF radar coverage and on East Coast in the Mid-Atlantic region. However, this is not the only STPS available. Two complementary studies used different modeling methods for STPS from HF radar data, one using a long historical record of HF radar currents to train the model and the second was developed as STPS for rapid deployment. Frolov et al. (2012) developed a predictive alogrithm for surface currents up to 48 hours in the future by using empirical orthogonal functions (EOFs). They used 1-2 years (minimum) of previous HF radar data and deconstructed it using EOFs to capture spatial variability which they then used to train their model. Their EOF-based STPS was more accurate for their area of interest than other existing operational model forecasts. In contrast, Barrick et al. (2012)

developed a STPS for rapid deployment of HF radars, in cases where radars are deployed for emergency operations, such as oil spill response. In this case, 1-2 years of HF radar data is not available to initiate a short-term predictive model. Instead, they created a STPS algorithm that could work with as little as 12 hours of previous data with predictions 24 hours into the future. They did experience poor performance during short-term local wind events, but the majority of the predictions agreed with with actual drift where mean winds were used. Where available, these STPS programs provide a spatially robust data set of predicted ocean currents for emergency responders.

A.3.3 Data Assimilating Ocean Current Models

The purpose of data assimilation into numerical models is to move beyond a purely mathematical solution to one that resembles reality as closely as possible. Le Traon (2013) outlines three major advancements in oceanography: satellite altimetry, Argo, and operational oceanography, but the three advancements are not independent, instead they work hand in hand to improve our knowledge of ocean science. Satellite altimetry provides global high resolution, near-real time sea surface heights. Oke and Schiller (2007) found that for the Ocean Forecasting Austrailia Model (OFAM) altimetry was critical in order to represent mesoscale variability, but without Argo measurments salinity variations were not well resolved. This was reinforced by Le Traon (2013), who showed that ocean models rely on altimetry and Argo data sets to constrain the models. Using data assimiliation, improvements were also noted in the Forecast Ocean Assimilation Model (FOAM) in the North Atlantic and Nucleus for European Modeling of Ocean VARiational (NEMOVAR) global output (Cummings et al. 2009). However, data assimilation into models can be a computationally intense processes that requires dedicated supercomputers. In addition, not all observations are available in real time and most observational data runs through at least a preliminary quality control process before assimilation into a model (Martin et al. 2015).

A.3.4 Search Models

To run drift simulations, the USCG uses the Search and Rescue Optimal Planning System (SAROPS) computer program. This program represents a large improvement in SAR technology and methods, from previous versions or hand calculations. For reference, Frost and Stone (2001) and Breivik et al. (2013) provides a robust overview of search methods prior to the implementation of SAROPS in the early 2000s. SAROPS is computationally similar to SAR models used in the East and South China Seas (Cho et al. 2014) and the Austrailian SARMAP program (http://asascience.com/software/sarmap/). SAROPS subjects drift objects to an ambient current with the specific leeway coefficients input for each search object given the observed or modeled wind speed and direction. It then uses a Monte Carlo approach to forecast drift position from a variety of initial condition scenarios that reflect the information from the reporting sources. The initial conditions include one to four search objects, uncertainty in time and spatial distributions. The spatial distributions include: (1) bi-variate normal distribution about point from a Last-Known-Position, (2) uniform distribution over a regular polygon for simulating fishing grounds, 3) distributions from lines of position(s) from radio transmissions or flare sightings, and (4) simulated voyages of the originating craft. Each object's position is subject to random walks to account for noise in the wind and current fields at the location of the particles, where each subsequent application of the random walk is correlated to the one before. One simulation can be run with up to 10,000 particles (representing 10,000 different drift runs for each object) per initial scenario. The output is then a probability map showing where the object is most likely to be found at each time-step, based on location of the highest particle density at that point in the simulation and accounting for all previous search efforts and the subjective weighting of the scenarios and 1 to 4 search objects likelihood. In order to complete these calculations, SAROPS requires access to oceanographic and meteorological data. This data is pulled from the Environmental Data Server (EDS) that aggregates and stores observational and forecasted wind and currents. This data includes global and regional numerical model forecasts of ocean currents and winds. It also includes

inputs of observational data from High Frequency (HF) Radars and Self-Locating Datum Marker Buoys (SLMDBs), a code-style drifter deployed during a SAR case to validate model currents. Both West and East Coast STPS current fields are provided to the EDS for use by SAROPS.

A.4 Searches in Offshore and Remote Locations

What makes remote search and rescue different from mainland scenarios is the low density of oceanographic data and the distance from response assets. Outside of the near-shore waters, many valuable resources are unavailable and due to the travel distance for response assets, time available to search on scene is reduced. In addition responders have to take into account fuel costs and crew fatigue constraints. The Central Pacific SAR area of responsibility, and the Hawaiian Islands in particular, make a good case study for remote SAR. The Hawaiian Islands are isolated, and have a low ratio of land to water (the islands only make up around 28,000 km^2). Here we investigate the location and density of SAR cases relative to available oceanographic datasets in the Central Pacific, and run three drift simulations using SAROPS. These case studies allow us to look at SAR statistics relative to available oceanographic resources and identify areas for improvement.

A.4.1 Remote SAR Case Study: The Hawaiian Islands

There are very few observational data sets available in the Central Pacific that can be pulled into the EDS for use in SAROPS. One observational data set that has recently been tested for use, is the surface portion of the 10-day ARGOS float cycle. While there are close to 4000 ARGO floats globally in the deep waters, only a few of the open ocean SAR cases can directly benefit from this data set. Most of the observations in the region are located near the main Hawaiian Islands due to the large population center located there. The only HF radar surface current data in the entire Central Pacific is found on the Hawaiian Islands (Fig. A.1). However, coverage is small. Only the southern and western shores of

Oahu, and Hilo Bay on the island of Hawaii are covered by real-time surface current data (red stars shown in figure A.1). By comparison, near continuous HF radar surface currents are available from Portland, Oregon to the California-Mexico border. Also, in contrast from the continental United States, is the lack of a STPS for surface currents based on the HF Radar data. The Hawaiian Islands do have a local ROMS model available. The Hawaii Regional Ocean Modeling System (HROMS) is a 4-km resolution ocean model that covers the main Hawaiian Islands. Nested inside are localized, higher resolution models in frequently trafficked areas such as the south shore of Oahu. Further information on HROMS is provided on the Pacific IOOS (PacIOOS) website. Available from PacIOOS is a regional Guam ROMS model with 2km resolution, as well as a Western North Pacific ROMS model with 4km resolution (Fig. A.2). Outside of those resources, the rest of the Central Pacific is left with only global scale ocean circulation models to conduct drift predictions.

SAR case data in the Pacific was examined using geographical position and case length, in hours (Fig. A.1). Most (66%) of search and rescue cases in the Central and Western Pacific occur within 12 nautical miles of land and were excluded from this analysis in order to focus on offshore search and rescue. For these offshore cases only a small percentage fall within the range of the HF radar real-time surface currents (4.5%) while one fifth fall within the Hawaii ROMS model currents (20%). If the Western Pacific and Guam ROMS model currents are added, the total number of offshore cases that are covered by ROMS increases to 40%. A detailed breakdown of SAR cases covered by each data source is provided in Table A.1. The highest case density occurs near the two main population centers, the Hawaiian Islands (Fig. A.1) and Guam (Fig. A.2) . However, once the cases are weighted by the time response assets spend on scene, other areas grow in importance. Since 2002, there have been 146 cases in offshore waters ($> 12nm$ from land) that exceeded 36 hours with response assets on scene. The majority of these cases occured in the Western Pacific near Guam, Palau, and the Federated States of Micronesia. Although this represents only 2% of SAR cases, due to the high hourly cost of response assets, these represent long search time, high cost cases with a low probability of success. In these locations, direct observations of

ocean currents are sparse, STPS from HF radars is unavailable, and coverage of the data assimilating regional ocean models is unavailable for the Federated States of Micronesia.

In order to investigate the impact of various observational data on SAR predictions, a drift simulation was conducted near the island of Oahu. The goal of the SAR simulation was to compare drift results from three different surface current data sources: direct observations via HF radar with 2-km horizontal resolution, modeled surface currents from HROMS with 4-km horizontal resolution, and modeled surface currents from Global HYCOM at 1/12° horizontal resolution. Two SAR cases were run simultaneously: a person in the water (PIW) without a lifejacket and a 14' sit-on-top kayak, both using the most current leeway coefficients available in SAROPS. The case was initiated with a last known position (LKP) for both objects of $21°10.302'N, 158°02.948'W$. The objects were drifted for 48 hours. This time frame was chosen because it kept the objects within the coverage of all three respective surface current sources during the whole drift. Additional time allowed both the objects to drift outside the coverage of the HF radar, invalidating the comparison. For all three simulations, the same wind source was used, the Hawaii based Weather Research and Forecasting (WRF) model at 3-km resolution. Particles were allowed to both run ashore (sticky shoreline) or "bounce" off the shoreline (slippery shoreline). The results of the three drift scenarios are shown in Figure A.3. Pink particles represent the PIW and brown particles represent the kayak. The drift run using the HF radar (Fig. A.3,top) resulted in the smallest area, with the particles (both PIW and kayak) covering a 2879km^2 area, compared to the HROMS run (Fig. A.3,middle) coming in at 7863km^2 and HYCOM (Fig. A.3,bottom) with the largest area of 12,196km^2. These results match previous studies that found the use of observational data including HF radar reduces search areas by up to a factor of 3 (Kohut et al. 2012; O'Donnell et al. 2005; Roarty et al. 2010).

A.5 Recommendations

One region in the Central Pacific that is not covered by ROMS is the area to the south of Guam, extending from Palau to the Federated States of Micronesia. This area contains 14.8% of offshore SAR cases, including the majority of the cases lasting longer than 36 hours. Increasing available observations in this region could benefit a large percentage of SAR cases. On a smaller scale, near the population hubs of Guam and Hawaii, case dense regions are the southern coast of Guam and the western shores of Hawaii and Maui. Additional coverage here could increase offshore SAR case coverage from 4.5% to 10%.

Another, more cost effective alternative to installing additional equipment is to maximize the use of what is already available. Brushett et al. (2017) used consensus modeling to evaluate search prediction effectiveness in the tropical Pacific. Using four different global ocean models, they found that a three or four model consensus search area was greatly reduced from a single model search area with a four model consensus being approximately one third the size of a search area produced by a single model. In addition to the large reduction in search area, they found that for their experiements, the consensus search area always contained the actual found position of the drift object. This is a promising result that suggests in areas with few options, consensus forecasts for SAR objects could reduce search area and decrease individual model error.

A.6 Conclusions

Even as sensors and search platforms continue to improve, mariners lost at sea aboard small craft which are difficult to detect, remain a problem for the world's coast guards. Narrowing search areas by accessing accurate, verified surface current fields will go a long way to successfully locating survivors and survivor craft, both saving lives and saving limited and expensive resource hours. Accessing and fully using all the available oceanographic data sets and numerical models is key to providing accurate predictions for the SAR trajectory models.

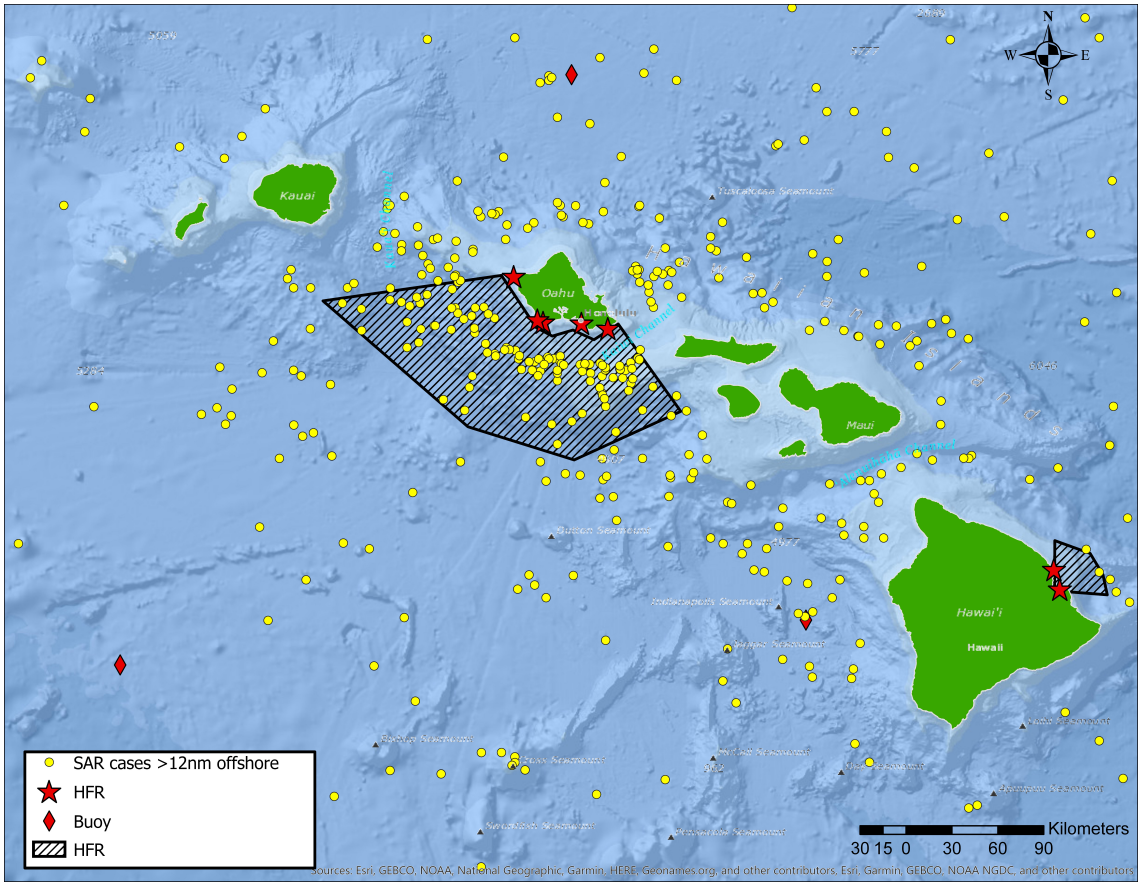

Figure A.1: Search and Rescue cases (yellow dots) in the Hawaiian Island region from 2002 through 2018. Only offshore cases (>12nm from land) are shown. Red stars indicate the locations of High Frequency Radars, red diamonds are the locations of moored surface buoys. The black hatched boxes represents the spatial coverage of the HF Radars.

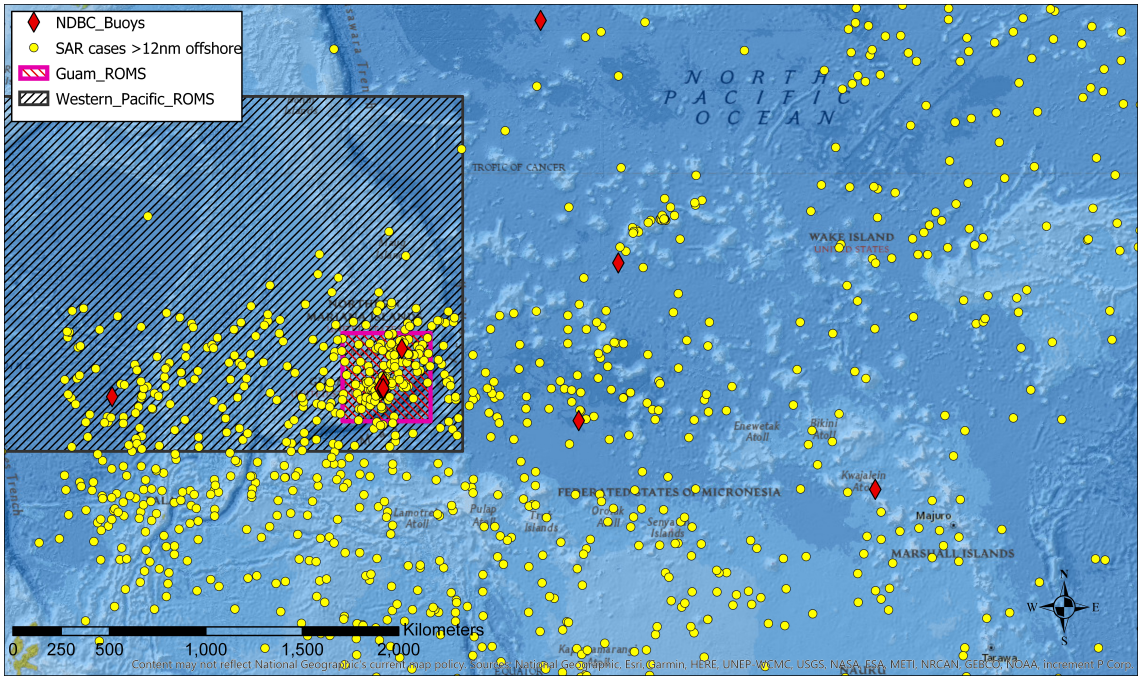

Figure A.2: Search and Rescue cases (yellow dots) in the Western Pacific region from 2002 through 2018. Only offshore cases (>12nm from land) are shown. Red diamonds are the locations of moored surface buoys. The hatched areas represent coverage of ROMS models.

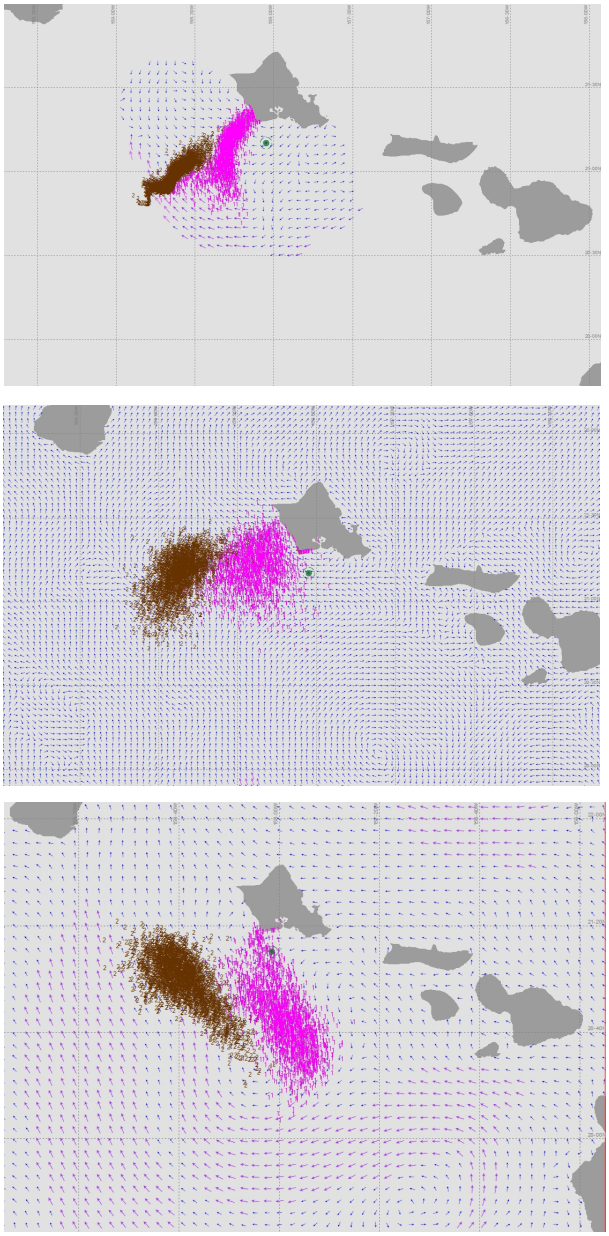

Figure A.3: SAROPS output from a simulated SAR case off Oahu. top: Particle density map for a 14 foot sit on top kayak (brown) and person in the water (pink) using ocean current data from available HF Radars. middle: Particle density map for a 14 foot sit on top kayak (brown) and person in the water (pink) using ocean current data from available HROM. bottom: Particle density map for a 14 foot sit on top kayak (brown) and person in the water (pink) using ocean current data from available global HYCOM.

Ocean Current Source	**% of cases covered**
HF Radar	4.5%
HI ROMS	20%
Guam ROMS	6%
Western Pacific ROMS	14%
Combined ROMS total	40%

Table A.1: Percentage of SAR cases covered by available ocean current data sources

References

Allen, A. and Plourde, J. Review of leeway: Field experiments and implementation. 1999. Report No. CG-D-08-99.

Allen, A.; Roth, J.C.; Maisondieu, C.; Breivik, Ø., and Forest, B. Field determination of the leeway of drifting objects. Technical Report 17, Norwegian Meteorological Institute, P.O. Box 43, Blindern NO-0313 OSLO, Norway, 8 2010.

Allen, Arthur. Leeway divergence. Technical report, U.S. Coast Guard Research and Development Center, 1082 Shenecossett Rd, Groton, CT, 1 2005.

Arbic, B.K.; Scott, R.B.; Chelton, D.B., and Richman, J.G. Effects of stencil width on surface ocean geostrophic velocity and vorticity estimation from gridded satellite altimeter data. *J. Geophys. Res.*, 117(C03029):1–18, 2012. doi: 10.1029/2011JC007367.

Aristegui, J.; Tett, P.; Hernandez-Guerra, A.; Basterretxea, G.; Montero, M.F.; Wild, K.; Sangra, P.; Hernandez-Leon, S.; Canton, M.; Garcia-Braun, J.A.; Pacheco, M., and Barton, E.D. The influence of island generated eddies on chlorophyll distribution: a study of mesoscale variation around gran canaria. *Deep Sea Res. Pt I*, 44:71–96, 1997.

Barrick, D.; Fernandez, V., and Ferrer, M.I. A short-term predictive system for surface currents from a rapidly deployed coastal hf radar network. *Ocean Dynam.*, 62:725–740, 2012.

Barton, E. Island wakes. In J.H., Steele; S.A., Thorpe, and K.K., Turekian, editors, *Encyclopedia of Ocean Sciences*, volume 5, pages 1397–1402. Academic Press, 2001.

Bellomo, L.; Griffa, A.; Cosoli, S.; Falco, P.; Gerin, R.; Iermano, I.; Kalampokis, A.; Kokkini, Z.; Lana, A.; Magaldi, M.G.; Mamoutos, I.; Mantovani, C.; Marmain, J.; Potiris, E.; Sayol, J.M.; Barbin, Y.; Berta, M.; Borghini, M.; Bussani, A.; Corgnati, L.; Orfila, A.; Poulain, P.-M.; Quentin, C.; Tintore, J.; Uttieri, M.; Vetrano, A.; Zambianchi, E., and Zervakis, V. Toward an integrated hf radar network in the mediterranean sea to improve search and rescue and oil spill response: the tosca project experience. *J. Oper. Oceanogr.*, 8(2):95–107, 2015.

Berkson, J.; Woityra, W.; Boda, K.; Allen, A.; Hicks, M., and Futch, V. The role of marine science and oceanography in the united states coast guard. *Proceedings, The Coast Guard Journal of Safety & Security at Sea*, 76(1):21–29, 2019.

Bidokhti, A.A. and Tritton, D.J. The structure of a turbulent free shear layer in a rotating fluid. *J. Fluid Mech.*, 241:469–502, 1992.

Bonjean, F. and Lagerloef, G.S.E. Diagnostic model and analysis of the surface currents in the tropical pacific ocean. *J. Phys. Oceanog.*, 32:2938–2954, 2002.

Breivik, O. and Allen, A. An operational search and rescue model for the norwegian sea and north sea. *J. Marine Syst.*, 69:99–113, 2008.

Breivik, O.; Allen, A.; Maisondieu, C., and Olagnon, M. Advances in search and rescue at sea. *Ocean Dynamics*, 63(1):83–88, 2013. doi: 10.1007/s10236-012-0581-1.

Brushett, B.; Allen, A.; Futch, V.; B., King, and C., Lemckert. Determining the leeway drift characteristics of tropical pacific island craft. *Applied Ocean Res.*, 44:92–101, 2014a.

Brushett, B.; Allen, A.; Futch, V.; King, B., and Lemckert, C. Determining the leeway drift characteristics of tropical pacific island craft. *Applied Ocean Research*, 44:92–101, 2014b. doi: 10.1016/j.apor.2013.11.004.

Brushett, B.A.; Allen, A.A.; King, B.A., and Lemckert, C.J. Application of leeway drift data to predict the drift of panga skiffs: Case study of martime search and rescue in the tropical pacific. *Applied Ocean Res.*, 67:109–124, 2017.

Burks, J.B. The flow of water through the molokai channel. Master's thesis, School of Ocean and Earth Sciences and Technology, University of Hawaii at Manoa, 1967.

Calil, P.; Richards, K.J.; Jia, Y., and Bidigare, R.R. Eddy activity in the lee of the hawaiian islands. *Deep Sea Res. Pt II*, 55(10):1179–1194, 2008.

Carnevale, G.F.; Briscolini, M.; Kloosterziel, R.C., and Vallis, G.K. Three-dimensionally perturbed vortex tubes in a rotating flow. *J. Fluid Mech.*, 341:127–163, 1997.

Castillo-Trujillo, A.C.; Partridge, D.; Powell, B., and Flament, P. Vorticity balance off the south shore of oahu, hawaii, derived by high-frequency radio doppler current observations. *J. Phys. Oceanog.*, 49:211–225, 2019.

Chavanne, C.; Flament, P.; Lumpkin, R.; Dousset, B., and Bentamy, A. Scatterometer observations of wind variations induced by oceanic islands: Implications for wind-driven ocean circulation. *Can. J. Remote Sens.*, 28(3):466–474, 2002.

Chavanne, C; Flament, P; Carter, G; Merrifield, M; Luther, D; Zaron, E, and Gurgel, KW. The surface expression of semidiurnal internal tides near a strong source at hawaii. part i: Observations and numerical predictions*. *J. Phys. Oceanog.*, 40(6):1155–1179, 2010a.

Chavanne, C.; Flament, P., and Gurgel, K-W. Interactions between a submesoscale anticyclonic vortex and a front*. *J. Phys. Oceanog.*, 40(8):1802–1818, 2010b.

Chawla, Arun; Tolman, Hendrik L.; Gerald, Vera; Spindler, Deanna; Spindler, Todd; Alves, Jose-Henrique G. M.; Cao, Degui; Hanson, Jeffrey L., and Devaliere, Eve-Marie. A multigrid wave forecasting model: A new paradigm in operational wave forecasting. *Weather and Forecasting*, 28(4):1057–1078, 2013. doi: 10.1175/WAF-D-12-00007.1. URL `https://doi.org/10.1175/WAF-D-12-00007.1`.

Chereskin, T. K. Direct evidence for an ekman balance in the california current. *Journal of Geophysical Research: Oceans*, 100(C9):18261–18269, 1995. doi: 10.1029/95JC02182. URL https://agupubs.onlinelibrary.wiley.com/doi/abs/10.1029/95JC02182.

Chew, F.M. and Busnell, M.H. The half-inertial flow in the eastern equatorial pacific: A case study. *J. Phys. Oceanog.*, 20:1124–1133, 1990.

Cho, K.-H.; Li, Y; Wang, H.; Park, K.-S.; Choi, J.-Y.; Shin, K.-I., and Kwon, J.-I. Development and validation of an operational search and rescue modeling system for the yellow sea and the east and south china seas. *J. Atmom. Ocean. Tech.*, 31:197–215, 2014.

Costa, B.M.; Poti, M.; Winship, A.; Miller, P., and Gove, J. Chapter 2: Environmental setting. In Costa, B.M. and Kendall, M.S., editors, *Marine Biogeographic Assessment of the Maine Hawaiian Islands*, page 359. Bureau of Ocean Energy Management and National Oceanic and Atmospheric Administration, 2016. OCS Study BOEM 2016-035 and NOAA Technical Memorandum NOS NCCOS 214.

Cummings, J.; Bertino, L.; Brasseur, P.; Fukumori, I.; Kamachi, M.; Martin, M.J.; Mogensen, K.; Oke, P.; Testut, C.E.; Verron, J., and Weaver, A. Ocean data assimilation systems for godae. *Oceanography.*, 22:96–109, 2009. doi: 10.5670/oceanog.2009.69.

Daingerfield, L. H. Kona storms. *Monthly Weather Review*, 49(6):327–329, 1921. doi: 10.1175/1520-0493(1921)49¡327:KS¿2.0.CO;2. URL http://dx.doi.org/10.1175/1520-0493(1921)49<327:KS>2.0.CO;2.

D'asaro, E.A. Generation of submesoscale vortices: A new mechanism. *J. Geophys. Res.*, 93:6685–6693, 1988.

Davis, R.E. Drifter observations of coastal surface currents during code: the method and descriptive view. *J. Geophys. Res.*, 90:4741–4755, 1985.

Davis, R.E.; Dufour, J.E.; Parks, G.J., and Perkins, M.R. Two inexpensive current-following drifters. *Ref*, 82-28:54 pp., 1982.

Di Maio, A.; Martin, M.V., and Sorgente, R. Evaluation of the search and rescue leeway model in the tyrrhenian sea: a new point of view. *Nat. Hazards Earth Syst. Sci.*, 16: 1979–1997, 2016. doi: 10.5194/nhess-16-1979-2016.

Ducet, N.; Le Traon, P.-Y., and Reverdin, G. Global high-resolution mapping of ocean circulation from TOPEX/Poseidon and ERS-1 and -2. *Journal of Geophysical Research*, 105:19477–19498, August 2000. doi: 10.1029/2000JC900063. URL `https://hal.archives-ouvertes.fr/hal-00772161`.

Ekman, V.W. On the influence of the earth's rotation on ocean currents. *Arkiv for Matematik, Astronomi och Fysik*, 2(11):1–52, 1905.

Emery, W.J. and Thomson, R.E. *Data Analysis Methods in Physical Oceanography*. Elsevier, 2 edition, 2004.

ESR, . *OSCAR third degree resolution ocean surface currents*. PO.DAAC, CA, USA, 1 edition, 2009. Dataset accessed 2016-03-01.

Flament, P.; Kennan, R.A.; Niiler, P., and Bernstein, L. The three-dimensional structure of an upper ocean vortex in the tropical pacific ocean. *Nature*, 383:610–613, 1996.

Flament, P; Kennan, S; Lumpkin, R; Sawyer, M, and Stroup, E. The ocean. *Atlas of Hawaii*, 3:82–86, 1998.

Flament, P.; Lumpkin, C.; Tournadre, J., and Armi, L. Vortex pairing in an anticylonic shear flow: discrete subharmonics of one pendulum day. *J. Fluid Mech.*, 440:401–409, 2001.

Fong, A.A.; Karl, D.M.; Lukas, R.; Letelier, R.M.; Zehr, J., and Church, M.J. Nitrogen fixation in an anticyclonic eddy in the oligotrophic north pacific ocean. *The ISME Journal*, 2:663–676, 2008. doi: 10.1038/ismej.2008.22.

Frolov, S.; Paduan, J., and Cook, M. Improved statistical prediction of surface currents based on historic hf-radar observations. *Ocean Dynam.*, 62:1111–1122, 2012.

Frost, J. and Stone, L. *Review of Search Theory: Advances and Applications to Search and Rescue Decision Support*. USCG Research and Development Center, 2001. Report No. CG-D-15-01.

Futch, V. The lagrangian properties of the flow west of oahu. Master's thesis, University of Hawaii at Manoa, 2009.

Garza, Jessica A.; Chu, Pao-Shin; Norton, Chase W., and Schroeder, Thomas A. Changes of the prevailing trade winds over the islands of hawaii and the north pacific. *Journal of Geophysical Research: Atmospheres*, 117(D11):n/a–n/a, 2012. ISSN 2156-2202. doi: 10.1029/2011JD016888. URL `http://dx.doi.org/10.1029/2011JD016888`. D11109.

Hackett, B.; Breivik, O., and Wettre, C. Forecasting the drift of objects and substances in the oceans. In E.P. Chassignet, J. Vernon, editor, *Oceans Weather Forecasting: An Integrated View of Oceanography*, pages 507–524. Springer, 2006.

Hardy, D.M. and Walton, J.J. Principle components analysis of vector wind measurements. *J. Applied Met.*, 17:1156–1162, 1978.

Harlan, J.; Allen, A; Howlett, E.; Terrill, E.; Kim, S.Y.; Otero, M.; Glen, S.; Roarty, H.; Kohut, J.; O'Donnell, J., and Fake, T. National ioos high frequency radar search and rescue project. In *OCEANS'11 MTS/IEEE KONA*, 2011. doi: 10.23919/OCEANS.2011.6107090.

Hodgins, D.O. and Hodgins, S.L.M. Phase ii leeway dynamics study program development and verification of a mathematical drift model for liferafts and small boats. Prepared for Canadian Coast Guard College, Dept. Fisheries and Oceans, 1998.

Hotelling, H. "analysis of a complex of statistical variables into principle components". *"J. Edu. Psych."*, 24:417–441,498–520, 1933.

Huang, Guoxing; Law, Adrian Wing-Keung, and Huang, Zhenhua. Wave-induced drift of small floating objects in regular waves. *Ocean Engineering*, 38(4):712 – 718, 2011. ISSN 0029-8018. doi: https://doi.org/10.1016/j.oceaneng.2010.12.015. URL `http://www.sciencedirect.com/science/article/pii/S0029801810002854`.

Jia, Y; Calil, P.HR; Chassignet, E.P.; Metzger, E.J.; Potemra, J.T.; Richards, K.J., and Wallcraft, A.J. Generation of mesoscale eddies in the lee of the hawaiian islands. *J. Geophys. Res.*, 116(C11), 2011.

Kennan, S. and Flament, P. Observations of a tropical instability vortex. *J. Phys. Oceanog.*, 30:2277–2301, 2000.

Jr.Kirwan, A.D.; McNally, G.; Chang, M.S., and Molinari, R. The effect of wind and surface currents on drifters. *J. Phys. Oceanog.*, 5:361–368, 1975.

Kloosterziel, R.C. and van Heijst, G.F. An experimental study of unstable barotropic vortices in a rotating fluid. *J. Fluid Mech.*, 223:1–24, 1991.

Kohut, J.; Roarty, H., and Randall-Goodwin, E. Evaluation of two algorithms for a network of coastal hf radars in the mid-atlantic bight. *Ocean Dynam.*, 62:953–968, 2012.

Large, W.G. and Pond, S. Open ocean momentum flux measurements in moderate to strong winds. *J. Phys. Oceanog.*, 11(3):324–336, 1981.

Le Traon, P.Y. Efrom satellite altimetry to argo and operational oceanography: three revolutions in oceanography. *Ocean Sci.*, 9:901–915, 2013. doi: 10.5194/os-9-901-2013.

Lilly, J.M. and Olhede, S.C. Generalized morse wavelets as a superfamily of analytic wavelets. *IEEE*, 60:6036–6041, 2012.

Lorenz, E. Empirical orthogonal functions and statistical weather prediction. Technical report, Air Force Cambridge Research Center, Air Research and Development Command, Cambridge, Mass., 1956.

Lumpkin, CF. Eddies an currents of the hawaiian islands. *Ph.D. thesis. Sch. of Ocean and Earth Sci. and Technol. Univ. of Hawaii at Manoa*, page 282, 1998.

Lumpkin, R. Global characteristics of coherent vortices from surface drifter trajectories. *J. Geophys. Res.*, 121(2):1306–1321, 2016. ISSN 2169-9291. doi: 10.1002/2015JC011435. URL `http://dx.doi.org/10.1002/2015JC011435`.

Lumpkin, R. and Flament, P. Extent and energetics of the hawaiian lee countercurrent. *Oceanography*, 26(1):58–65, 2013.

Lumpkin, R. and Pazos, M. Measuring surface currents with surface velocity program drifters: the instrument, its data, and some recent results. In Griffa, A.; Kinwan, A.D.; Mariano, A.; Ozgokmen, T., and Rossby, T., editors, *Lagrangian Analysis and Prediction of Coastal and Ocean Dynamics*, chapter 2, pages 39–67. Cambridge Univ. Press, Cambridge, U.K., 2007.

Lumpkin, R.; Flament, P.; Kloosterziel, R., and Armi, L. Vortex merging in a 1 1/2 layer fluid on an f-plane. *J. Phys. Oceanog.*, 30:233–242, 2000.

Martin, M.J.; Balmaseda, M.; Bertino, L.; Brasseur, P.; Brassington, G.; Cummings, J.; Fujii, Y.; Lea, D.J.; Lellouche, J.-M.; Mogensen, K.; Oke, P.R.; Smith, G.C.; Testut, C.-E.; Waagb/o, G.A.; Waters, J., and Weaver, A.T. Status and future of data assimilation in operational oceanography. *J. of Operational Oceanogr.*, 8(S1):s28–s48, 2015. doi: 10.1080/1755876X.2015.1022055.

Menkes, C.E.; Kennan, S.C.; Flament, P.; Dandonneau, Y.; Masson, S.; Biessy, B.; Marchal, E.; Eldin, G.; Grelet, J.; Montel, Y.; Morliere, A.; Lebourges-Dhaussy, A.; Moulin, C.; Champalbert, G., and Herbland, A. A whirling ecosystem in the equatorial pacific. *Geophys. Res. Lett.*, 29, 2012.

Meyers, G. Seasonal variation in transport of the pacific north equatorial current relative to the wind field. *J. Phys. Oceanog.*, 5:442–449, 1975.

Mitchum, G.T. The source of 90-day oscillations at wake island. *J. Geophys. Res.*, 100: 2459–2475, 1995.

Morel, A.; Claustre, H., and Gentili, B. The most oligotrophic subtropical zones of the global ocean: similarities and differences in terms of chlorophyll and yellow substance. *Biogeosciences*, 7:3139–3151, 2010.

Morris, J.T.; Osychny, V.I., and Turner, A.C. Analytical techniques for the calculation of leeway as a basis for search and rescue planning. page 10. OCEANS 2008, IEEE, 9 2008.

Morrison, I. and Businger, S. Synoptic structure and evolution of a kona low. *Weather and Forecasting*, 16(1):81–98, 2001.

Niiler, P.P.; Sybrandy, A.S.; B., Kenong; Poulain, P.M., and Bitterman, D. Measurements of the water-following capability of holey-sock and tristar drifters. *Deep-Sea Res. I*, 42 (11):1951–1964, 1995.

O'Donnell, J.; Ullman, D.; Spaulding, M.; Howlett, E.; Fake, T.; Hall, P.; Isaji, T.; Edwards, C.; Anderson, E.; McClay, T.; Kohut, J.; Allen, A.; Lester, S.; Turner, C., and Lewandowski, M. Integration of coastal ocean dynamics application radar (codar) and short-term predictive system (stps) surface current estimates into the search and rescue optimal planning system (sarops). 2005. Report No. CG-D-01-2006.

Oke, P.R. and Schiller, A. Impact of argo, sst, and altimeter data on eddy-resolving ocean reanalysis. *Geophys. Res. Lett.*, 34:L19601, 2007. doi: 10.1029/2007GL031549.

Olhede, S.C. and Walden, A.T. Generalized morse wavelets. *IEEE*, 50:2661–2671, 2002.

Patzert, W.C. Eddies in hawaiian waters. *HIG*, 69(8):55, 1969.

Pazan, S.E. and Niiler, P.P. Recovery of near-surface velocity from undrogued drifters. *J. Atmos. Ocean Tech.*, 18:476–489, 2001.

Pond, S. and Pickard, G.L. *Introductory Dynamical Oceanography*. Elsevier, The Boulevard, Kidlington, Oxford, OX5 1GB, 2 edition, 1983. ISBN 978-0-750624961.

Poulain, P.M. and Warn-Varnas, A. Near-surface circulation of the nordic seas as measured by lagrangian drifters. *J. Geophys. Res.*, 101(C8):18237–18258, 1996.

Poulain, P.M.; Ursella, L., and Brunetti, F. Direct measurements of water-following characteristics of code surface drifters. Ist. Naz. di Oceanografia e di Geofisica Sperimentale (OGS), Trieste Italy, 12 2000.

Poulain, P.M.; Gerin, R., and Mauri, E. Wind effects on drogued and undrogued drifters in the eastern mediterranean. *J. Atmos. Ocean Tech.*, 26(7):1144–1156, 2009. doi: 10.1175/2008/JTECHO618.1.

Qiu, B.; Koh, D.A.; Lumpkin, C., and Flament, P. Existence and formation mechanism of the north hawaiian ridge current. *J. Phys. Oceanog.*, 27(3):431–444, 1997.

Rayleigh, Lord. On the dynamics of revolving fluids. *Proc. R. Soc. Lond.*, 93(A):148–154, 1916.

Rio, M.-H.; Mulet, S.; Greiner, E.; Picot, N., and Pascual, A. New global mean dynamic topography from a goce geoid model, altimeter measurements and oceanographic in-situ data. OSTST2013, 2013. URL http://www.aviso.altimetry.fr/fileadmin/documents/OSTST/2013/oral/mulet$_M DT_C NES_C LS1$3

Roarty, H.; Glenn, S., and Allen, A. Evaluation of environmental data for search and rescue. pages 1–3. OCEANS 2016, Shanghai, 2016.

Roarty, H.; Allen, A.; Glenn, S.; Kohut, J.; Nazzaro, L., and Fredj, E. Evaluation of environmental data for search and rescue ii. pages 1–3. OCEANS 2018, Kobe, 2018.

Roarty, H.J.; Glenn, S.M.; Kohut, J.T.; Gong, D.; Handel, E.; Rivera Lemus, E.; Garner, T.; Atkinson, L.; Jakubiak, C.; W., Brown; Muglia, M.; Haines, S., and Siem, H. Operation and application of a regional high frequency radar network in the mid atlantic bight. *Mar. Technol. Soc. J.*, 44(6):133–145, 2010.

Rockewell Geyer, W. Field calibration of mixed-layer drifters. *J. Atmos. Ocean Tech.*, 6: 333–342, 1989.

Sanderson, M. Introduction. In Sanderson, M., editor, *Prevailing Trade Winds: Weather and Climate in Hawaii*, pages 1–11. 1993.

Sasaki, H.; Xie, S-P; Taguchi, B.; Nonaka, M., and Masumoto, Y.". Seasonal variations of the hawaiian lee countercurrent induced by the meridional migration of the trade winds. *Ocean Dynamics*, 60(3):705–715, 2010. doi: 10.1007/s10236-009-0258-6. URL `http://dx.doi.org/10.1007/s10236-009-0258-6`.

Service, National Ocean. Tidal currents average speed and direction. https://tidesandcurrents.noaa.gov/currents13/tab2pc4.html, 8 2018. Site run by Center for Operational Oceanographic Products and Services.

Smith, Jerome A. Observed variability of ocean wave stokes drift, and the eulerian response to passing groups. *Journal of Physical Oceanography*, 36(7):1381–1402, 2006. doi: 10.1175/JPO2910.1. URL `https://doi.org/10.1175/JPO2910.1`.

Souza, J.; Powell, B.S.; Castillo-Trujillo, A., and P., Flament. The vorticity balance of the ocean surface in hawaii from a regional reanalysis. *submitted to Journal of Physical Oceanography*, 2014. Submitted to Journal of Physical Oceanography.

Stokes, G.G. On the theory of oscillatory waves. *Trans. Camb. Philos. Soc.*, 8:441–455, 1847.

Talley, L.D.; Pickard, G.L.; Emery, W.J., and Swift, J.H. *Descriptive Physical Oceanography, an Introduction*. Elsevier, 6th edition, 2011. ISBN 978-0-7506-4552-2.

Ullman, D.; O'Donnell, J.; Edwards, C.; Fake, T.; Morschauser, D.; Sprague, M.; Allen, A., and Krenzien, B. Use of coastal ocean dynamics application radar (codar) technology in u.s. coast guard search and rescue planning. 2003. Report No. CG-D-09-03.

Vaillancourt, R.D.; Marra, J.; Seki, M.P.; Parsons, M.L., and Bidigare, R.R. Impact of a cyclonic eddy on phytoplankton community structure and photosynthetic competency in the subtropical north pacific ocean. *Deep Sea Res. Pt I*, 50:829–847, 2003. doi: doi:10.1016/S0967-0637(03)00059-1.

van den Bremer, T.S. and Breivik, O. Stokes drift. *Philos Trans A Math Phys Eng Sci.*, 376(2111), 2018. doi: 10.1098/rsta.2017.0104.

Villas Bôas, A. B.; Sato, O. T.; Chaigneau, A., and Castelão, G. P. The signature of mesoscale eddies on the air-sea turbulent heat fluxes in the south atlantic ocean. *Geophysical Research Letters*, 42(6):1856–1862, 2015. doi: 10.1002/2015GL063105. URL `https://agupubs.onlinelibrary.wiley.com/doi/abs/10.1002/2015GL063105`.

Wilkin, J.; Rosenfeld, L.; Allen, A.; Baltes, R.; Baptista, A.; He, R.; Hogan, P.; Kurapov, A.; Mehra, A.; Quintrell, J.; Schwab, D.; Signell, R., and Smith, J. Advancing coastal ocean modelling, analysis, and prediction for the u.s. integrated ocean observing system. *J. Operational Oceanogr.*, 2017. doi: 10.1080/1755876X.2017.1322026.

Williams, G. *Linear Algebra with Applications*. Jones and Bartlett Learning, 8 edition, 2014. ISBN 978-1-4496-7954-5.

Wyrtki, K. Fluctuations of the dynamic topography in the pacific ocean. *J. Phys. Oceanog.*, 5:450–459, 1975.

Wyrtki, K. Eddies in the pacific north equatorial current. *J. Phys. Oceanog.*, 12:746–749, 1982.

Wyrtki, K. and Kilonsky, B. Mean water and current structure during the hawaii-to-tahiti shuttle experiment. *J. Phys. Oceanog.*, 14:242–254, 1984.

Xian, Peng and Miller, Ron L. Abrupt seasonal migration of the itcz into the summer hemisphere. *Journal of the Atmospheric Sciences*, 65(6):1878–1895, 2008. doi: 10.1175/2007JAS2367.1. URL `https://doi.org/10.1175/2007JAS2367.1`.

Xie, S-P; Liu, W.T.; Liu, Q., and Nonaka, M. Far-reaching effects of the hawaiian islands on the pacific ocean-atmosphere system. *Science*, 292(5524):2057–2060, 2001.

Y.Yang, J. Ma S-P Xie. Observations of the trade wind wakes of kauai and oahu. *Geophys. Res. Lett.*, 35(4):L04807, 2008. doi: 10.1029/2007GL031742.

Yoshida, S.; Qiu, B., and Hacker, P. Wind-generated eddy characteristics in the lee of the island of hawaii. *J. Geophys. Res.*, 115(C3), 2010.